Johannes Kofler, BSc

Fabrication and investigation of micro – and nano – fluidic devices: Fundamental aspects and sensor applications

MASTER THESIS

For obtaining the academic degree
Diplom-Ingenieur

Master Programme of
Technical Physics

Graz University of Technology

Supervisor:

Ao. Univ.-Prof. Dipl.-Ing. Dr.techn. Emil J. W. List

Institute of Solid State Physics

Graz, February 2011

Deutsche Fassung:
Beschluss der Curricula-Kommission für Bachelor-, Master- und Diplomstudien vom 10.11.2008
Genehmigung des Senates am 1.12.2008

EIDESSTATTLICHE ERKLÄRUNG

Ich erkläre an Eides statt, dass ich die vorliegende Arbeit selbstständig verfasst, andere als die angegebenen Quellen/Hilfsmittel nicht benutzt, und die den benutzten Quellen wörtlich und inhaltlich entnommene Stellen als solche kenntlich gemacht habe.

Graz, am ....
(Unterschrift)

Englische Fassung:

STATUTORY DECLARATION

I declare that I have authored this thesis independently, that I have not used other than the declared sources / resources, and that I have explicitly marked all material which has been quoted either literally or by content from the used sources.

....
date (signature)

Acknowledgement

To begin with, I would like to thank my supervisor Prof. Emil J. W. List for giving me the opportunity to work in his team at the NTC Weiz and his support throughout the work. For financial support, the research project cluster ISOTEC (RP DEVFAB) is acknowledged.

I would also like to thank Stefan Sax for his co-supervision, guidance, patience and his trust. I also greatly acknowledge the interesting discussions and his reviewing which has improved this work.

I especially thank Alexander Blümel for his support, his test structures and his magnificent AFM images. Further, I would like to thank Alexander Blümel and Stefan Sax for introducing me into electron beam lithography.

Furthermore I would like to thank Dr. Karl Popovic for the inkjet printed masters and Sonja Larissegger for inputs concerning all chemical stuff.

I also have to thank my co-students Sebastian Nau and Kerstin Schmoltner for their interest in my work and for creating a frolicsome working atmosphere.

I would also like to thank Peter Krapp for all the stuff concerning the E-Line and for coating my samples with metal.

Moreover, I would like to thank the whole team of the NanoTecCenter Weiz Forschungsgesellschaft mbH for the great collaboration and their assistance. Hereby I would like to thank Hannes Holl for his persistent efforts to keep the time records up to date.

Finally yet importantly, I would like to thank my parents for financial support throughout my studies and Martina Brunnhofer for her support and love.

Abstract

Microfluidic systems gained tremendous importance over the last few years. Recent advances in this emerging technology lead to a revolution of molecular biology, DNA analysis and proteomics. Other key applications are clinical pathology, testing of air / water for biochemical toxins and other dangerous pathogens. The goal is to integrate and automate whole laboratory processes onto a single chip not requiring any qualified personal to operate.

This master thesis focuses on the fabrication of such microfluidic systems via replica molding using polydimethylsiloxane (PDMS). Liquid PDMS pre-polymer is casted onto a structured master yielding a negative polymeric PDMS replica / mold which is subsequently bonded onto a flat substrate. The advantage of this technique is that it is cheap and furthermore that it allows rapid prototyping.

The masters to be replicated are structured by electron beam lithography, inkjet printing or a combination of these two. The benefit of combining these two techniques is that the functional part of the microfluidic chip can be structured by slow electron beam lithography with a high resolution, whereas the access channels are printed by the fast inkjet printer with a low resolution. Thus, required resources and fabrication times are minimized. Electron beam lithography requires a profound understanding of the electron – resist and electron – substrate interactions leading to the so called proximity effect. In order to create typical microfluidic structures it is necessary to characterize these interactions and to compensate them by a proximity correction. Using this proximity correction, it is possible to create well defined structures with lateral dimensions ranging from 500 nm up to 10 µm while keeping the designed integrity. Furthermore, it is possible to tune the final resist height after development continuously and in a controlled manner through resist profile simulations.

After replicating the master, the mold is bonded onto another substrate. The relevant bonding techniques are stamp and stick bonding, oxygen plasma activated bonding and reversible pressure assisted bonding. The bonding quality of these techniques is investigated by pressure tests. The stamp and stick bonding technique can be used to bond microfluidic chips in a non-invasive manner onto sensible organic field effect based sensing systems and to seal ink jet printed electrodes with a thickness of 10 µm. Whereas plasma activated bonding is used to bond microfluidic systems requiring high external pressures (> 6 bar) onto smooth and clean SiO_2 / glass substrates.

The function of the fabricated microfluidic devices, a T-junction, a mixer and a reservoir are validated. In order to inject fluids into the microfluidic devices, a reversible pressure assisted interconnect is designed to safely seal pressures up to 1 bar.

Kurzfassung

In den letzten Jahren erlangten Mikrofluidik Systeme enorme Wichtigkeit. Die aktuellen Fortschritte dieser aufkommenden Technik haben die Molekularbiologie, die DNA-Analyse und die Proteomik revolutioniert. Andere aufkeimende Anwendungsgebiete sind zum Beispiel Laboratoriumsmedizin und das Testen von Wasser auf biochemische Toxine. Das Ziel ist es, ganze Laborprozesse/- analysen zu automatisieren und auf einen einzelnen Chip, dessen Bedienung kein Fachpersonal mehr benötigt, zu integrieren.

Diese Arbeit fokussiert auf die Fabrikation genannter Mikrofluidik-Systeme mittels der „replica molding“ Technik mit polydimethylsiloxane (PDMS). Die Struktur eines „Masters“ wird repliziert indem PDMS Pre-Polymer auf diesen abgegossen, gehärtet und anschließend abgezogen wird. Der so erhaltene Abdruck, wird anschließend auf ein flaches Substrat gebondet. Diese Technik hat den Vorteil, dass sie billig ist, da sie das mehrmalige Verwenden der „Master“ Strukturen ermöglicht und dass Prototypen schnell erstellt und auf ihre Funktion getestet werden können.

Die Strukturierung der „Master“ wird mittels Elektronenstrahl-Lithographie, Inkjet-Drucken oder einer Kombination beider durchgeführt. Die Kombination der Techniken zeichnet sich dadurch aus, dass der funktionale Bereich des Chips mittels der hoch-auflösenden aber langsameren Elektronenstrahl-lithographie strukturiert wird, wohingegen die Peripherie mit niedriger Auflösung, dafür schneller, mit dem Inkjet Drucker gedruckt wird. Somit werden Zeit und Ressourcen gespart. Die Elektronenstrahl-lithographie setzt unter anderem ein Verständnis der Interaktion der Elektronen mit dem Elektronenstrahllack und dem Substrats voraus. Diese Interaktion, der sogenannte „Proximity Effect“, muss charakterisiert und mittels einer „Proximity“ Korrektur berücksichtigt werden, um komplexe Microfluidik Systeme strukturieren zu können. Die „Proximity“ Korrektur ermöglicht es, definierte Strukturbreiten zwischen 500 nm und 10 µm mit gleichbleibenden Lackhöhe zu erstellen. Des Weiteren kann die Kanalhöhe kontinuierlich und kontrolliert durch Lackprofil-Simulationen eingestellt werden.

Nach dem Replizieren des „Masters“ wird das Replikat (der „Mold“) auf ein Substrat gebondet. Die relevanten Bond Techniken wie zum Beispiel die „Stamp and Stick Bonding“ Technik und das Sauerstoffplasma aktivierte Bonden, wurden mittels Drucktests untersucht. Die „Stamp and Stick Bonding“ Technik ermöglichte es, Microfluidik Systeme nicht invasiv auf sensible organische Feldeffekt basiernende Sensorensysteme zu bonden. Diese Technik kann auch verwendet werden um Inkjet geprintete Elektroden mit Dicken bis zu 10 µm verlässlich abzudichten.

Die Funktionsweise der erstellten Mikrofluidik Systeme („T-junction“, Mixer, Reservoir) wird validiert. Dazu werden die Flüßigkeiten mittels eigens designter reversibler „Interconnects“, die Druck bis zu 1 bar verlässlich abdichten, injeziert.

Content

1. Introduction

Microfluidics covers a huge area of research topics documented by an extensive number of reviews and books. The goal of this master thesis is neither to give an introduction into microfluidics, nor to create complex microfluidic systems but rather to focus on the fabrication of microfluidic systems via the replica molding technique using PDMS as done for example by D. C. Duffy [**1**]. A positive side effect of this work is that not only know-how in the fabrication of microfluidic systems is gained. Furthermore replica molding can also be used as a base for micro structuring. Keywords in this area are for instance micro contact printing and metal transfer printing. [**2**]

The introduction starts by defining the term microfluidics and by discussing the major advantages as well as disadvantages of this technique. Subsequently, the fabrication of microfluidic chips via replica molding is explained.

1.1. Why microfluidics?

First of all it is important to define the term microfluidics: “Microfluidics is the science and engineering of systems in which fluid behavior differs from conventional flow theory primarily due to the small length scale of the system”. [**3**] Thus, fluidic systems are not characterized by their actual metric size but rather by their characteristic length scales. The latter determine the fluid behavior. Typical microfluidic systems deal with length scales between 1 µm and a few 100 µm.

Microfluidic systems gained a tremendous importance over the last few years. The applications range from DNA analyses systems and protein folding devices used in biology to the integration of whole laboratory processes onto a single chip. [**4**] The advantages of these systems is that the required samples volumes for fluid analysis or manipulation range from mL to pL which is especially important when dealing with expensive samples as well as in the case of medical investigations. Another benefit is that they are fast, tiny and that parallel automatic processing is possible. It is believed that microfluidic systems will revolutionize life sciences and biology. [**4**] [**3**], [**5**] “The question is if microfluidic systems revolutionize large-scale automation of chemistry and biology as micro fabricated integrated circuits revolutionized computation by vastly reducing the space, labor and time required for calculations.” [**4**] Microfluidic systems fabricated by replica molding are interesting because their fabrication is cheap and rapid prototyping is possible. [**1**]

One really important aspect in microfluidic systems to consider is that, one must question whether working at these small length scales is really beneficial. The maximum sensitivity a sensor can have is limited by the analyte concentration in the sensed volume. The relation between the sensed volume V and the minimal analyte concentration A_i is given by [**3**]:

Equation 1-1)
$$V = \frac{1}{\eta_S N_A A_i}$$

V … sample volume; η_S… sensor efficiency; N_A … Avogadro number; A_i … concentration of the analyte

If the sample volume is too small it may not contain any target molecules rendering any detection useless: Typical immunoassays have a concentration of 10^8 to 10^{18} copies per milliliter requiring sample volumes of the order of nL, whereas DNA analyses of human blood with a concentration of 10^2 to 10^7 copies per mL require sample volumes of the order of mL. [**3**] Therefore, the concentration of analytes in the sample and the sensitivity of the sensor determines the dimensions of the microfluidic system.

Another disadvantage of microfluidic systems is that the ratio between the surface of the channel and the volume of the liquid is very small. Therefore, the material of the channel walls and impurities on it influence significantly the fluid behavior. [**3**]

1.2. Principles of fabrication

The principle fabrication process of microfluidic systems in the case of replica molding is shown in figure 1. The first step is to structure the master (figure 1 step 1). This can be done by different techniques, e.g. inkjet printing and electron beam lithography (EBL). Then an initially liquid PDMS pre-polymer is poured onto the master and cured (figure 1 step 2a-2b) yielding a solid PDMS polymer which is subsequently peeled off the master (figure 1 step 2c). The resulting structured polymer slice is a negative replication of the master (mold). The mold is then bonded onto another substrate (figure 1 step 3). Finally, the microfluidic chip is connected to the macroscopic world, e.g. to syringe pumps (figure 1 step 4).

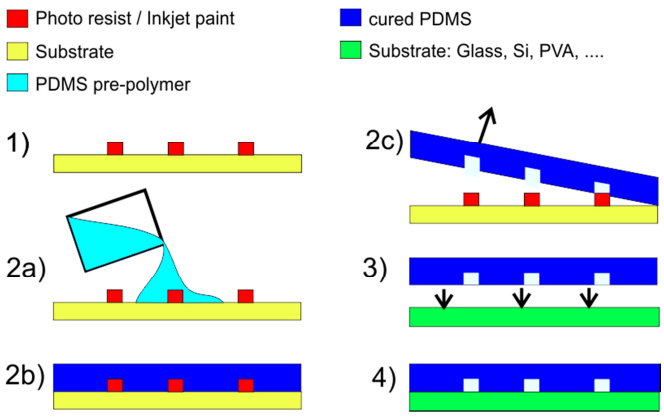

Figure 1: Fabrication process of a microfluidic chip created by replica molding. 1) The master is structured by inkjet printing or EBL. 2) Mold fabrication: a) Pouring a liquid PDMS pre-polymer onto the master. b) Cure the PDMS pre-polymer. c) Lift off of the PDMS mold. 3) Bonding of the mold onto another substrate. 4) Connecting the microfluidic chip to the macroscopic world.

2. Theory and applications of micro- and nano- fluidics

In order to introduce the reader to the microfluidic theory, this chapter starts by explaining the fundamental Navier stokes equations and the properties of laminar flow. Secondly, the relevant subjects' laminar flow and capillary pressure in a rectangular channel and bubble formations mechanisms at a T-junction are discussed.

These chapters only give a very rough overview of the fundamentals relevant to this work. An overall summary of microfluidic related theories and its different aspects would exceed the scope of this work and is given in reference [**3**], for example.

2.1. Principles of laminar flow

The velocity field of an incompressible, Newtonian fluid can be described by equation 2-1:

Equation 2-1)
$$\rho\left(\frac{\partial\vec{u}}{\partial t}+\vec{u}\cdot\nabla\vec{u}\right)=\Delta p+\eta\nabla^2\vec{u}+\vec{f}$$
$$\nabla\cdot\vec{u}=0$$

$\vec{u}$…velocity field; $\vec{f}$… body force; ρ… density; η… viscosity

The terms on the left side in equation 2-1 correspond to the inertial force densities. The inertial force densities consist of an unsteady acceleration ($\frac{\partial\vec{u}}{\partial t}$) and a convective acceleration ($\vec{u}\cdot\nabla\vec{u}$) term. The latter is the time independent acceleration of a fluid with respect to space. It is nonlinear and responsible for the chaotic behavior, irreversibility and turbulences. The terms on the right side correspond to the pressure difference induced force density (Δp), the viscous force density ($\eta\nabla^2\vec{u}$) and a body force density ($\vec{f}$).

The ratio between the inertial force densities and the viscous force densities is described by the Reynolds number (Re). The viscous force density scales as $\frac{\eta u}{L^2}$ and the inertial force density scales as $\frac{\rho u^2}{L}$. [**4**] Thus, the Re number is defined as:

Equation 2-2)
$$Re=\frac{Inertial\ force}{Viscous\ force}=\frac{\rho uL}{\eta}$$

ρ ... characteristic density; u ... characteristic velocity; L ... characteristic length scale. This length scale can be defined by convention. In this master thesis the length scale is defined as the hydraulic-radius; η ... characteristic viscosity

In the case of microfluidic systems, the volume to surface ratio is very small. The surface force densities such as the viscous force are therefore dominant compared to inertial force densities

leading to small Re numbers. If the Re is below a critical value ($Re_{critical}$), the inertial force densities can be neglected. This leads to the laminar Stokes flows:

Equation 2-3) $$\Delta p + \eta \nabla^2 \vec{u} + \vec{f} = 0 \;\; and \; \nabla \cdot \vec{u} = 0$$

$\vec{u}$…velocity field; $\vec{f}$… body force; ρ … density; η… viscosity

Equation 2-3 is linear, deterministic and time reversible. Time reversibility is of course only true if one does not consider irreversible molecular diffusion. Since the non-linear convective acceleration is neglected, there is no time independent acceleration of a fluid with respect to space any more, i.e. there are no turbulences or eddies due to the geometry of the channel. The behavior of laminar flow is sometimes counter-intuitive and is explained with the help of two examples.

The first example is illustrated in figure 2. A microfluidic channel is filled with two liquids, one blue, the other one red; the liquids flow from the bottom to the top. In the case of low Re, there are no non-linearities due to geometry and the liquid passes the obstacles (stars) completely ignoring them (figure 2 on the left). Increasing the flow velocity increases the Re number. If the Re number is large enough, vortexes and turbulences start to occur, leading to a mixture of the fluids (figure 2 on the right).

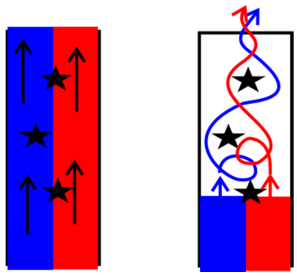

Figure 2: Two liquids which are marked red and blue flow in microfluidic channel. Left; laminar flow; there are no turbulences induced by the obstacles (black stars). Right; turbulent flow; the obstacles induce vortexes which lead to a fast mixing.

“All mixing - whether in turbulent or laminar flows - occurs due to molecular diffusion. Fluid stirring can be used to stretch and fold inhomogeneous fluids blobs until mixing (diffusive migration across streamlines occurs). The basic idea behind mixers is to use stirring motions to reduce the distance over which mixing must occur.” [**4**] As a consequence at low Re numbers, the fluids flow parallel in a channel without folding into each other, leading to an inefficient mixing. Consider the left channel of figure 2 and suppose width of d = 100 µm. The blue fluid contains solvated ions with a size of ~0.1 nm and small proteins with a size ~5 nm. In the case of laminar flow, the time to obtain complete mixing corresponds to the time the ions / proteins require to diffuse a distance d onto the other side of the channel which is approximately $\tau \sim d^2/D$ (D … diffusion constant). Thus, the ions would reach the other side in about 5 s (D = 2*10³ µm²/s [**4**]) and the proteins would reach the other side in about 250 s (D = 40 µm²/s [**4**]). In the turbulent regime the fluids would be folded into each other due to turbulences reducing the required diffusion length for complete mixing and thus also the mixing time.

Hence, mixing in a laminar flow regime is not efficient. As a consequence especially designed mixers have to be used. Probably the most popular one used for low Re numbers (Re ~ 1) is the staggered herringbone mixer shown in figure 3. The fluid flows from the left to the right. The grooves on the bottom deflect the fluid flowing over them onto the side walls (see figure 3). Consequently, a vortex is created. The herringbone structure creates a small and a big vortex. Anyhow, this alone would not lead to efficient mixing; the large vortex has to be folded into the smaller one by mirroring the herringbone structure. These vortexes are deterministic and reversible but the mixing still scales chaotic [**4**]: If the fluid flow would be reversed, the fluid would end up being completely separated as it was before entering the mixer. This is of course only true if molecular diffusion is neglected.

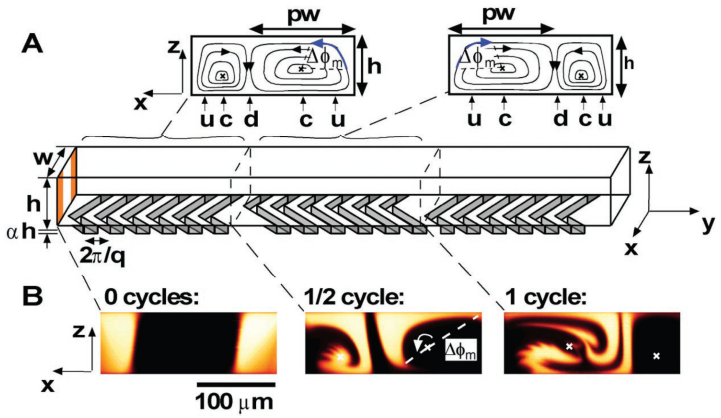

Figure 3: Staggered herringbone mixer (picture taken from reference [6]). The flows from the left to the right. The grooves on the bottom create vortexes which fold the fluids into each other.

There are many other aspects and applications of laminar flow which are not going to be discussed here. A comprehensive summary is given by T. M. Squires [**4**], by S. Colin [**3**] and by N.T. Nguyen [**5**].

2.2. Flow in a rectangular channel

Suppose a laminar flow in a rectangular channel and further suppose that there is no-slip between the channel walls and the fluid, i.e. the velocity of the fluid at the interface is zero (no-slip boundary condition). Then the volumetric flow rate in the channel is approximately: [**7**]

Equation 2-4)

$$\dot{Q} = \frac{ba^3}{12\,\eta}\left(\frac{\Delta p}{\Delta L}\right)$$

$$u(y,z) = \frac{16a^2}{\pi^3\eta}\left(\frac{\Delta p}{\Delta L}\right)$$

$\dot{Q}$ … volumetric flow rate; b … longer edge of the rectangular channel; a … shorter edge of the rectangular channel; η… viscosity; Δp … pressure difference between the beginning and the end of the channel; ΔL … length of the channel.

Equation 2-5 already implies a no-slip boundary condition. This does not pose any problems as long as the channels are macroscopic, but the smaller they get the higher is the influence of the walls and thus also the influence of the boundary conditions. There are strong indications that there is a slip flow in micro- and nano- scale channels which can be quantified by the slip length. [**8**] The slip length

depends on interactional parameters between the solid and the fluid like shear stress, wetting properties, fluid properties and interfacial roughness. [**8**], [**9**] Another effect not considered in equation 2-4 is that there are temperature gradients of a few degrees K in micro channels with characteristic length scales below 100 µm. These temperature gradients lead to viscosity gradients within the fluid and consequently also to a deviation from equation 2-5. [**9**], [**5**] Furthermore, equation 2-4 is based on a continuum model which does not have to be valid in sub µm channel. To what extent the continuum model is still valid is described by Knudsen number (Kn) which is defined in equation 2-5. [**9**]

Equation 2-5) $$Kn = \lambda/L$$

λ … mean free path of the molecules (for gases) and intermolecular length for liquids, L… characteristic length scale.

If the characteristic length scale L approaches λ, the continuum model can't be used any more. For water, the characteristic length should be around 100 nm whereas for gases such as N_2 it would be around 1 µm. [**9**] Water can therefore be treated with the continuum equations as long as the channel dimensions are larger than 100 nm. [**9**]

2.3. Capillary pressure in a channel

The capillary pressure, the filling time and the volumetric flow rate in a rectangular channel imposing a no-slip boundary condition can be approximated by equation 2-6. [**10**]

Equation 2-6) $$\Delta P = 2\sigma\cos(\theta)\left(\frac{1}{a}+\frac{1}{b}\right)$$

$$\dot{Q} = \frac{ba^3}{12\eta}\left(\frac{\Delta \mathrm{p}}{\Delta L}\right)$$

$$\Delta L = \sqrt{\frac{2\,\Delta \mathrm{p}\,a^2}{12\,\eta}t}$$

$\dot{Q}$ … volumetric flow rate; b … longer edge of the rectangular channel; a … shorter edge of the rectangular channel; η … viscosity; Δp … capillary pressure; ΔL ... length of the channel filled with liquid; t ... time; $\cos(\theta)$ … advancing contact angle of the liquid; σ … surface tension of the liquid.

Again the no-slip boundary condition does not have to be valid for tiny channels and also the roughness of the channel walls is not considered.

2.4. Droplet / plug formation at a T-junction

The droplets / plugs are generated by mixing two immiscible fluids (see figure 4). There are a few droplet / plug generation systems but this work will only focus on the so called T-junction. The actual mechanisms of droplet / plug formation depend very much on the geometry and are still under investigation.

The droplets / plugs at a T-junction are created by injecting the dispersed phase perpendicular into a continuous phase as shown in figure 4. The dispersed and the continuous phase are both immiscible and both flow at constant flow rate through the channels, i.e. the droplet formation is not due to oscillating flows.

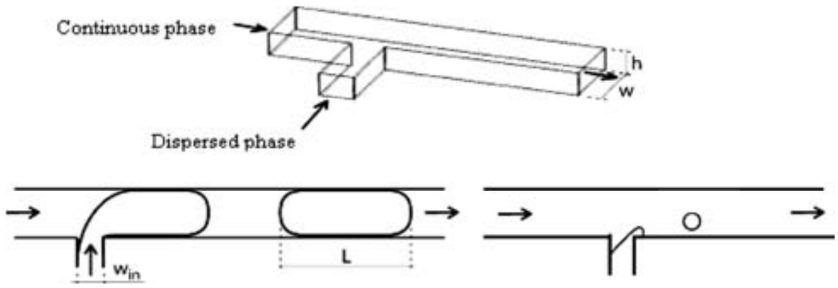

Figure 4: Droplet / plug formation in a T-junction (Picture from reference [11]). The dispersed phase gets injected into the immiscible continuous phase creating plugs (left) or droplets (right). Plugs / Droplets are defined as plugs if their length is two times the channels' width (L> 2w) whereas they are called droplets if their length is smaller than the channels' width (L< w). [11]

The droplet / plug formation is governed by two competing stresses: On one hand, there is the shear force / viscous force between the continuous phase and the dispersed phase which drags the interface downstream (scales like $\mu_c u_c$). On the other hand there is the surface tension (scales like γ) between the phases trying to reduce the interfacial area. [**4**]. The formation mechanisms are characterized by the capillary number Ca which is defined as the ratio between these two forces: [**11**], [**12**], [**13**]

Equation 2-7) $$\mathrm{Ca_c} = \frac{\mu_c u_c}{\gamma}$$

μ_c… viscosity of the continuous phase; u_c… average velocity of the continuous phase; γ… interfacial tension.

It is assumed that there are three different droplet formation regimes which can be distinguished by the Ca number of the continuous phase [**11**], [**12**], [**13**]:

- $Ca_c < 0.002$ (see figure 5 (a) and figure 6): The squeezing regime / plug formation; the shear force is not strong enough to drag the dispersed phase along. Thus, the dispersed phase expands into the channel blocking the continuous phase. For that reason, pressure is accumulated upstream by the continuous phase. This pressure drop across the plug (squeezing pressure) dominates the break up, i.e. ruptures the dispersed phase into plugs.

- $0.01 < Ca_c < 0.3$ (see figure 5 (c) and figure 6): The dripping regime / droplet formation; the shear force is high enough to drag the dispersed phase along downstream where the dispersed phase is ruptured into drops by the interfacial tension. Thus, the formation process is governed by both the shear force and the surface tension. If the Ca number is too high (Ca > 0.3) the dispersed fluid gets dragged along without a rupture and one obtains parallel laminar flow (see reference [**14**] for details).
- $0.002 < Ca_c < 0.01$ (see figure 5 (b)): The transient regime; in this regime the droplet formation is due to a combination of the two mechanisms mentioned above.

An illustration of the different droplet formation regimes is shown in figure 5. Please note that the plug / droplet size of each of these regimes scales differently and that this scaling is not intuitive. Details can be found in reference [**11**], [**12**] and [**13**].

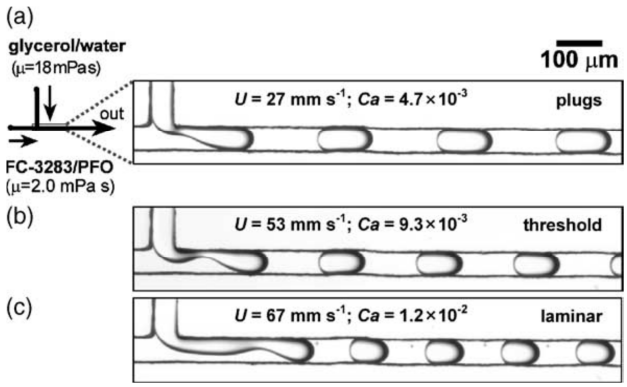

Figure 5: Picture from [14]: Visualization of the three regimes: Water gets injected from the top. The carrier fluid flows from the left to the right. a) Low values of Ca, plug flow regime. The plugs are formed right at the channel. The viscous force is too weak to drag the dispersed fluid along. b) Transition between plug and droplet flow regime. c) Droplet flow regime: The dispersed phase gets dragged along and is ruptured into drops downstream.

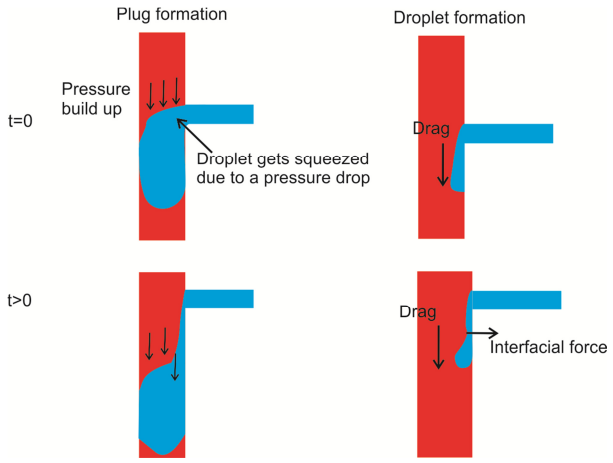

Figure 6: Droplet / plug formation mechanisms. Plug formation; the dispersed phase (blue) is not dragged along by the continuous phase (red). The formation is dominated by the pressure which is build up upstream (squeezing pressure). Droplet formation; The viscous force is strong enough to drag the dispersed phase downstream where the dispersed phase will eventually get ruptured into drops by the interfacial force. Thus, the formation mechanism is determined by the viscous force and the interfacial force.

3. Experimental methodology - Electron beam lithography

The main advantage of electron beam lithography over conventional photo lithography is that it allows writing structures in the sub 100 nm range due to the shorter wavelength of the electron beam. Besides that, this type of lithography is very flexible since no photo masks are required. Thus, it is possible to structure complex microfluidic systems with a high resolution and flexibility. The disadvantage of this technique is that it is a sequential raster technique. It is therefore slow (> 24 h) at writing large area-wide structures (> 1 mm²).

The principles of electron beam lithography and the system used (Raith E-Line), are presented first. Once these principles are explained, the proximity effect which is a consequence of the interaction volume of the electrons with the resist and the substrate is elucidated. The electrons get scattered in the resist and in the substrate exposing regions which were originally not addressed by the electron beam. This interaction volume can reach as far as 2 µm from the incident beam into the resist influencing the geometry of the exposed structures. It is therefore essential to take into account the proximity effect via a proximity correction in order to obtain a conformal map of the designed structures. The final paragraph deals with the optimization of the resist, e.g. the determination of the proximity effect parameters, the contrast curve and the limits of the system.

3.1. Electron beam lithography principles

First of all, the electron beam lithography system, Raith E-Line, used in this work is presented. Then the relevant parameters of the exposure are discussed. The concept of write fields, which is used to write structures extending over the maximal scan field size (1mm²) is introduced subsequently. Then the alignment of the beam, relative to the sample is discussed. The influence and the compensation of temperature drifts is explained in the end.

Figure 7: Electron beam lithography system E-Line from Raith.

3.1.1. Raith E-Line

The electron beam lithography system discussed and used in this work is the Raith E-Line. The system is shown in figure 7. This system is controlled by two computers and basically consists of the following subsystems (see figure 8) [**15**]:

- Electron optical column (Zeiss Gemini) with a Schottky thermionic field emission emitter (brightness 10^7 A/cm².sr.kV) and electromagnetic lenses; the parameters to be adjusted are the acceleration voltage and the aperture. The electron beam generated by the column has to be further optimized by aperture- and stigmation- alignment.
- Deflection system with two scan generators:
    - The raster scan generator which is primarily used for SEM imaging.
    - The digital pattern generator which is primarily used for lithography; It rasterizes the structures to be exposed in a vector mode. The resolution and the scan speed are higher than that of the raster scan generator. The digital pattern generator can also be used to record images or line scans.
- High precision X-Y-Z stage with laser interferometer for X-Y positioning with a resolution of 2 nm.
- Secondary electron detectors:
    - The Inlens detector provides shadow and distortion free images for voltages below 20 kV. This detector provides a slight material contrast, e.g. it's possible to distinguish between SiO_2 and organic contaminations.
    - The off-axis Everhardt-Thornley secondary electron detector provides topographic information of the surface.

These subsystems are controlled by two interacting computers systems. The first one controls all the tasks for an exposure, e.g. layout editing, lithography job setup and starting exposures (see figure 7 left screen). The second computer is responsible for the column settings and for SEM imaging. It provides all functions for recording, modifying and saving SEM images (see figure 7 right screen). [**15**] The interactions of the computers and their tasks are shown in figure 8.

It is important to mention that the resolution of the pattern generator is higher than that of the raster scan generator used for SEM imaging. The resolution of the raster scan generator is equal to the resolution of the screen used. The digital pattern generator allows scanning with a higher resolution at the same magnification, i.e. one can look, with the same magnification, at a cut out of the scanned area increasing the resolution of the screen. This is the major difference between computer 1 and computer 2 (left and right screen shown in figure 7). At the right side, zooming can only be done by increasing the magnification. On the left side zooming can also be done by increasing the resolution.

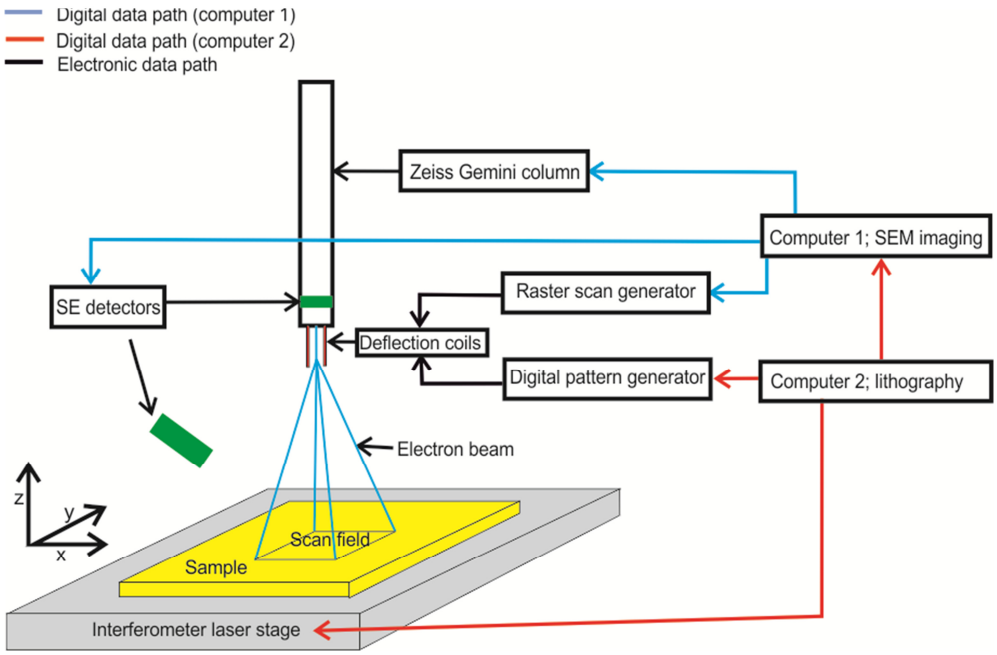

Figure 8: The E-Line electron beam lithography system; the system is controlled by two computers. Computer 1 handles the tasks necessary for SEM imaging, e.g. it controls the Zeiss Gemini column, the SE detectors and the raster scan generator which in turn drives the deflection coils. Computer 2 manages the lithographic processes. It directly controls the precision interferometer laser stage and the digital pattern generator which drives the deflection coils. The Zeiss Gemini column and the SE detectors are accessed by communicating with computer 1.

3.1.2. Principles of exposure

The principle process of structuring a substrate by electron beam lithography is shown in figure 9. First, the resist is spin coated onto a substrate (figure 9 step 1). Then the electron beam rasterizes the designed structures exposing each raster point through the deposited energy in its interaction volume (figure 9 step 2). In the case of a negative resist, the deposited energy renders the resist insolvable, whereas in the case of a positive resist, the deposited energy increases the solubility in the developer. [**16**] The next step after the exposure is to place the sample into the developer which dissolves the unexposed / exposed negative / positive resist regions (figure 9 step 3).

The local solubility of the resist is determined by the amount of deposited / dissipated energy per volume. Thus, the final resist profile and also the final resist height after development is related to the deposited energy in the resist. [**16**] The deposited energy in a volume depends on the dose and on the acceleration voltage. The acceleration voltage, a global parameter, has to be chosen prior to exposure and is equal for all designed structures of an exposure, whereas the dose can be different for each designed structure. The height and the profile of the structures can be tuned by the dose. The dose is defined as:

Equation 3-1) $$D = \frac{I}{\Delta x \Delta y} t$$

D ... dose $[C/m^2]$; $\Delta x/\Delta y$ ... step size of the electron beam; t ... point exposure time; I ... the beam current.

The dose which describes how much charge a certain area receives can roughly be tuned prior to exposure by the beam current and by the step size. The beam current depends on the acceleration voltage and on the aperture. The step size determines the resolution, i.e. the size of the designed structures is rounded to a multiple of the step size. The fine tuning of the dose during the exposure is done via the dwell time. Two problems to consider are that there is a minimum dwell time leading to a minimum dose value and further that the dwell time can't be tuned continuously leading to discrete dose values. For that reason it is important to roughly tune the dose by the acceleration voltage and the aperture in a way that a fine tuning around the value which is necessary to develop the resist is possible. Furthermore, it is important to mark that the structures are all designed using normalized doses. The actual applied absolute dose is then set prior to exposure by multiplying it with the selected base dose. Hence, the same design can be exposed at different absolute doses if the base dose is changed.

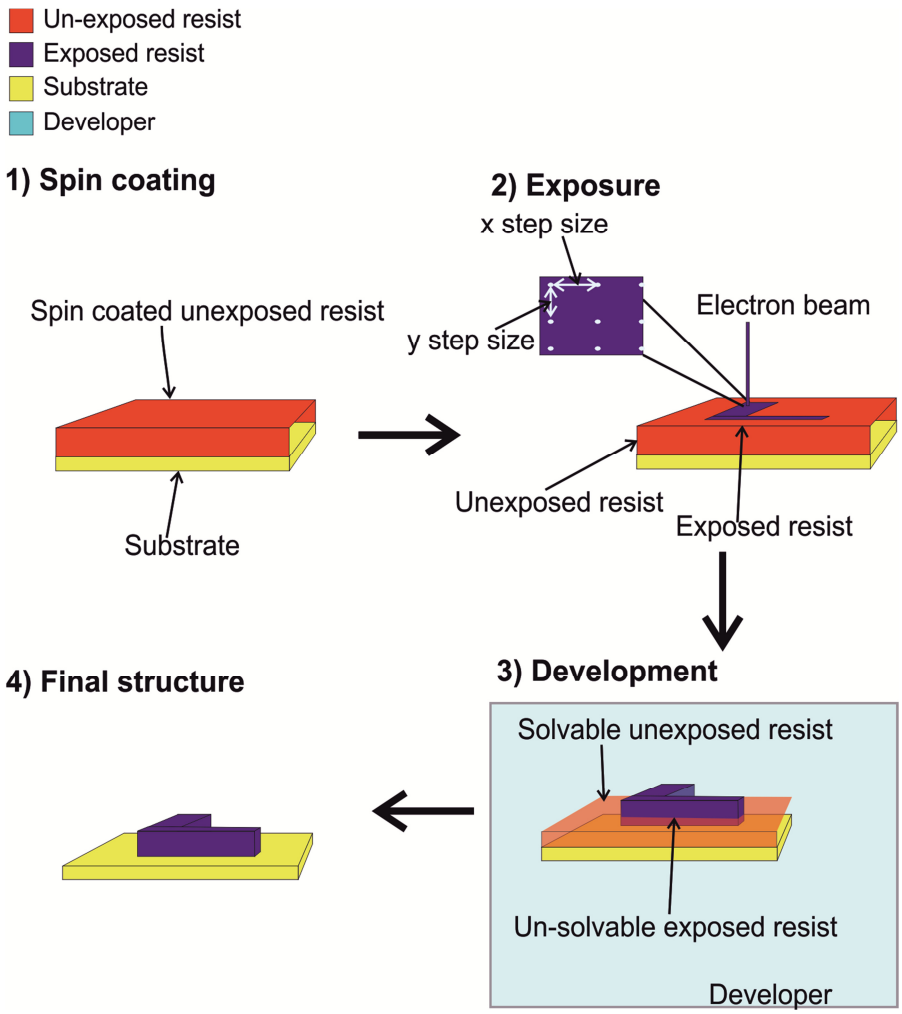

Figure 9: Structuring of a master and a negative resist with electron beam lithography: 1) The resist is spin coated on a substrate; 2) The designed structures are rasterized by the beam and the resist is exposed by the deposited energy of the incident electron beam in a raster point. 3) The exposed resist is developed; the developer dissolves the unexposed resist; 4) The final structure made by electron beam lithography.

3.1.3. Write field

The maximal size of the field which can be scanned (scan field) by the electron beam is determined by the magnification set prior to the exposure (maximum 1 mm²). Structures which have dimensions larger than this scan field, have to be separated into different write fields. First all the elements within one write field are exposed. Then the stage moves to the center of the next write field and the elements in this new write field are exposed (see figure 10).

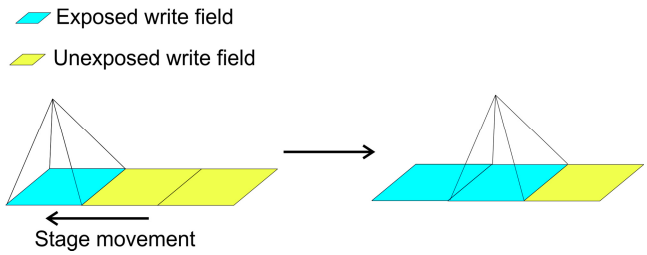

Figure 10: Writing multiple write fields; first, the elements within one write field are exposed. Subsequently the stage moves and afterwards all elements within the next write field is exposed and so forth.

However, it's not only the maximal size of the scan field which limits the maximal write field size but also the required resolution. The digital pattern generator which scans the structure and deflects the beam can process a limited amount of pixels (2^{16}). Thus, the minimal step size and therefore the resolution are limited by the write field size:

Equation 3-2) $$\Delta x = \frac{Write\ field\ size}{2^{16}}$$

Δx … minimal step size

A write field of 100 µm x 100 µm for example has a minimal step size of 1.5 nm, whereas a write field of 1 mm x 1 mm has a minimal step size of 15 nm.

3.1.4. Alignment of the beam

There is the coordinate system of the beam (U', V') and the coordinate system of the sample / stage (U, V). The coordinate system of the sample / stage is considered to be exact since the stage has a resolution of 2 nm and an accuracy of 1.6 nm which is higher than the resolution and accuracy of the beam. Furthermore, the current coordinates of the sample / stage are considered to be in the center of the write field.

The point is that the coordinate system of the beam (U', V') is not identical to the coordinate system of the sample / stage. The coordinate system of the beam is rotated, compressed and twisted compared to the coordinate system of the stage. Thus, writing structures, extending over multiple write fields is not possible. Consider an exposure of a rectangle with a length of 300 µm using a 100 µm write field (see figure 11). Once the first write field has been exposed, the stage moves 100 µm into the center of the next write field. Then the beam should be deflected exactly 50 µm to continue the exposure of the rectangle at the border between the write fields. The point is that the beam is not deflected 50 µm, it's deflected with another magnitude in another direction creating gaps in the rectangle between the write fields.

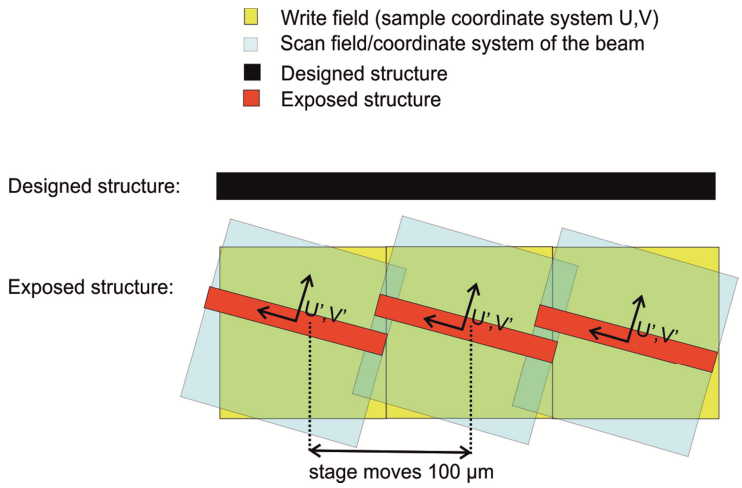

Figure 11: Exposing a structure extending over multiple write fields. The coordinate system of the beam U', V' is rotated, twisted and compressed compared to the coordinate system of the stage U,V. Thus, the actual exposed structure does not correspond to the designed structure.

Therefore, the coordinate system of the beam has to be determined by a write field alignment which measures the following parameters:

- The zoom factor which scales the U', V' coordinates of the beam to the U, V coordinates of the sample.
- The rotation between the coordinate system of the beam and the U,V coordinate system of the sample.
- The shift between the center of the scan and center of the write field.

The write field alignment is executed as follows (see figure 12): A point P with known coordinates is chosen and placed into the center of the write field / thought center of the scan field. Thus, the current position of the stage corresponds to the coordinates of this point (U, V). Subsequently, the digital pattern generator scans a small area / image whose center is believed to lie exactly on this point. The difference / offset between the thought and the real center is determined manually or automatically by recognizing this point (step 1). Then the stage is displaced (step 2). The digital pattern generator scans another field which is believed to be situated around the point P. The center of the scanned image should again lie on top of the point P. The offset is then determined by re-recognizing the point P. This process is repeated at least twice but the accuracy is increased with multiple displacements. Furthermore, the smaller the scanned area around the point P, the higher the resolution and the more accurate is the alignment.

Once the coordinate system of the beam is known, it is transformed electronically by the digital pattern generator in a way that it corresponds to the coordinate system of the sample. The coordinates of the new transformed scan field corresponds therefore to the coordinates of the write field defined by the stage (see figure 13).

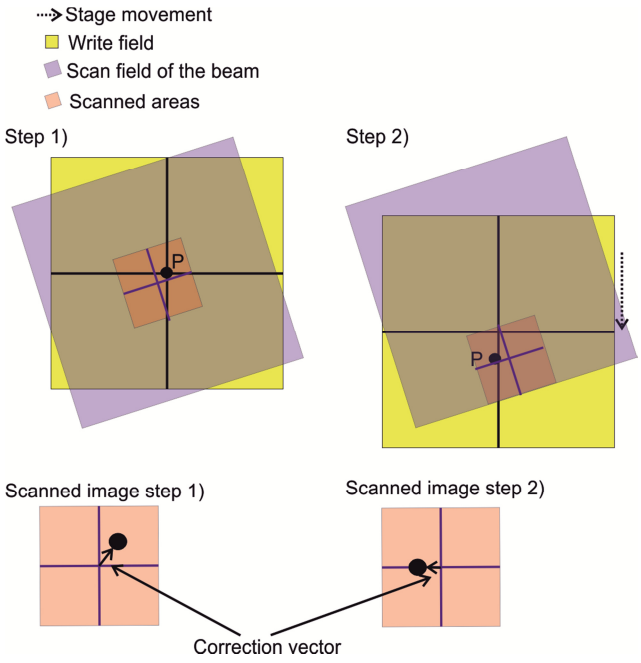

Figure 12: Determination of the coordinate system of the beam by a write field alignment.

The magnification has to be adjusted in a way that the transformed scan field is larger than the write field. This way the scan fields overlap, allowing writing structures extending over multiple write fields. There are following additional details which have to be considered:

- Recording an image using the digital pattern generator is in fact the same as an exposure of this image. Consequently, the image is actually recorded in U, V coordinates.
- One of the major problems is that the scan field is strongly influenced by temperature drifts. This poses especially a problem writing large and time consuming structures. Therefore, there are automatic write field alignments adjusting the drifted coordinate system of the beam to that on the sample. These automatic write field alignments can be executed after each exposure of one write field.

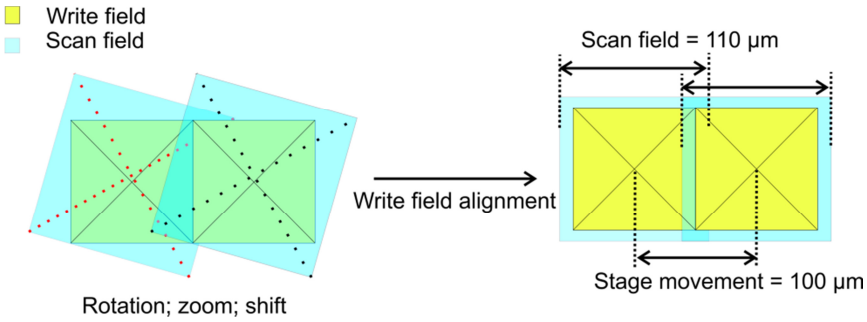

Figure 13: Left; there is a difference between the coordinate system of the scan field/beam and the coordinate system of the write field / stage. Right; the transformed scan field whose coordinate system is identical to that of the stage/write field. The transformed scan field must be larger than the write field in order to write structures extending over multiple write fields.

3.1.5. Drift compensation

As already discussed in the sub chapter above, the scan field of the beam drifts. The minimal beam drift is 2 nm/s at temperature variations of ±0.5 °C. [**15**] This is especially a problem if large structures which require long writing times are exposed or if two consecutive, aligned exposures are conducted. In the first case beam drifts would lead to overlaps / gaps in structures ranging from one write field to another. In the second case the consecutive exposures would not be aligned correctly to each other. It is therefore important to re-align the beam automatically during the exposure via an automatic write field alignment.

Alignments always require well defined alignment marks. These marks should ideally have a high contrast and they should be well defined even below 100 nm. Contamination spots fulfill these conditions. As a consequence, alignment marks composed of contamination spots were written onto a SiO_2 surface. An exemplary mark is shown in figure 14. Writing such marks already requires a good write field alignment and also a good stigmation, aperture and focus adjustment; if the write field alignment is done poorly, it is almost impossible to find the mark after writing it whereas a good stigmation, aperture and focus adjustment is necessary in order to burn the contamination spots. The problem with these alignment marks is that they eventually get destroyed if they are scanned multiple times with a very high resolution and integration time which is necessary to look at structures smaller than 100 nm because the scanning itself also contaminates the surface leading to a decreasing contrast between alignment mark and its surroundings. Therefore, it is practical to create an array of alignment marks. This way, if an alignment mark is destroyed one can move on to the next one.

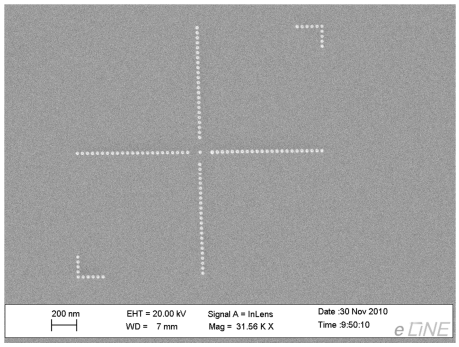

Figure 14: Alignment mark written by a line exposure with a spot dwell time of 500 ms and line step size of 30 nm. The contamination spot in the middle has a diameter of about 20 nm.

The alignment / drift compensation itself is not done by re-adjusting the coordinate system of the sample. The alignments / drift compensations are always done by a simple write field alignment using the central point as a reference. The coordinates of this central point have to be defined once and are never changed thereafter.

Figure 15 on the left shows a structure exposed without automatic write field alignment. The write field size was 100 µm requiring an exposure time of 1 ½ h. One can see that the scan field was deformed during the exposure leading to defects. Thus, automatic write field alignments have to be carried out in between exposing write fields. The drift after 1 ½ h is usually too large and consequently the alignment mark is usually not found any more. Hence, it is necessary to use smaller write fields with shorter exposure times. The structure shown in figure 15 on the right was exposed

using write fields with a size of 50 µm requiring about 25 min writing time. After the exposure of each write field, an automatic write field alignment was carried out. One can see the structure has less defects due to beam drift than the previous one.

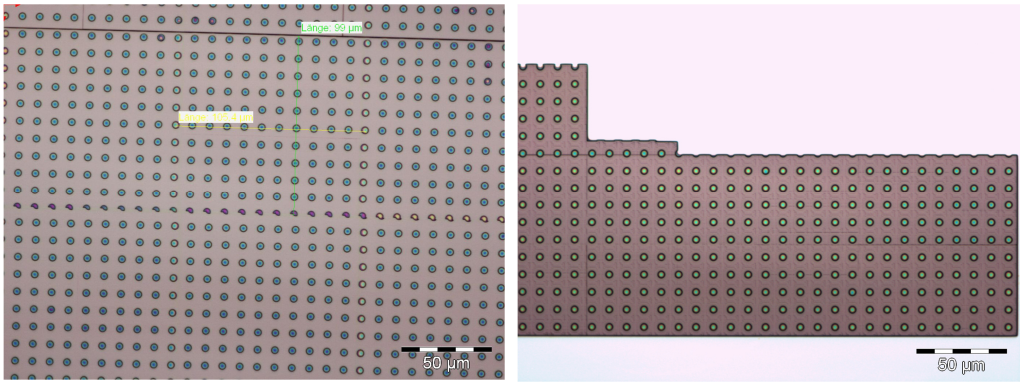

Figure 15: Left; structure exposed with a write field of 100 µm without automatic write field alignment. Right: Structure exposed with write fields of 50 µm and automatic write field alignment. The write fields are marked with black transparent rectangles. No failures occurred in this structure.

Two aligned consecutive exposures require exactly the same procedure. An example of such two consecutive exposures is shown in figure 16. The first exposure was carried out at 20 kV and the subsequent second exposure at 5 kV. At 5 kV, the electrons get stuck in the resist. Thus, the resist is not developed all the way down to the substrate like at 20 kV. Hence, one can write pending bridges at 5 kV whose posts are exposed at 20 kV. The alignment of these consecutive exposures is then done by a write field alignment using alignment marks and a reference point with known coordinates. First the alignment mark is written and the coordinates of the reference point are defined. Then, before exposing a layer, a write field alignment is carried out in order to align the beam as exactly as possible to the alignment marks and to the reference point. The offset between the exposures, i.e. the alignment error, was around 100 nm. This offset can further be reduced if one waits till the beam is stabilized which takes about 4 h after changing the acceleration voltage. However, it is believed that the alignment can be done with accuracy smaller than 50 nm.

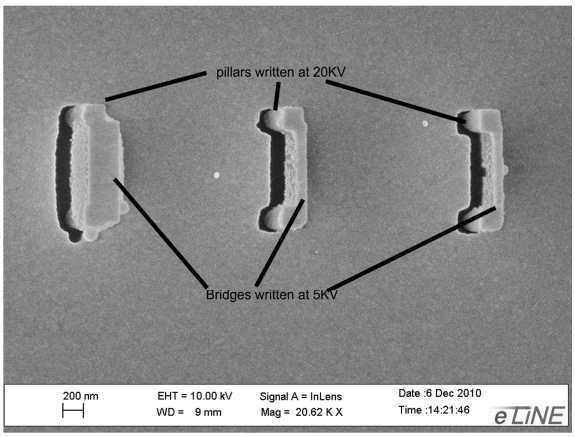

Figure 16: Two layer exposure. The exposure written at 20 kV penetrates the whole resist and was used to create the pillars. Subsequently, the pending bridges in between the pillars were exposed at 5 kV. The sample was coated with Ag and tilted in order to record this image. The black areas are metal free whereas the light areas are covered by Ag.

3.2. Proximity effect

The designed structures are rasterized by the electron beam which exposes the resist through the dissipated / deposited energy in its interaction volume which extends over a few µm leading to the so called proximity effect. It's the deposited energy which determines the solubility of the resist in the developer and therefore also the final shape / profile of the structures. [**16**] Hence, the final structure obtained after development is not a conformal map of the designed applied dose distribution but of the deposited energy distribution. It is therefore essential to characterize and compensate this proximity effect by proximity correction in order to actually replicate the design with the required resolution. The consequences of the proximity effect are illustrated in figure 17.

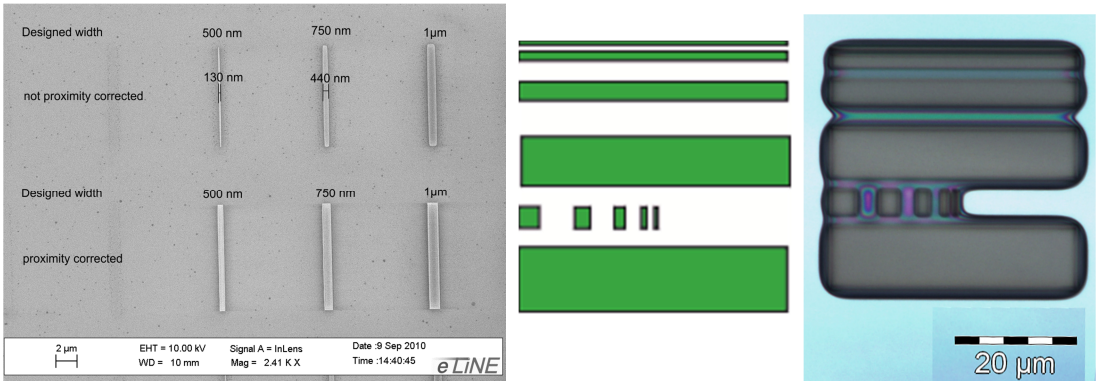

Figure 17: Left; Developed rectangles examined with the SEM. If the proximity effect is not taken into account (upper rectangles), then the resulting structures do not agree with the designed structures. Whereas, if the structures are proximity corrected the designed integrity is kept. Center; design of the test structure Right; image made by an optical microscope of the exposed and developed test structure shown in the center. The rectangles are rounded and the gaps between them have been exposed by the proximity effect.

The principles and consequences of the proximity effect are introduced first. The deposited energy distribution in the resist of an incident electron beam is described mathematically by the proximity function. The parameters of this function have to be determined experimentally by a doughnut test. Once the proximity function is known, one can compensate the proximity effect by a proximity correction and additionally one can also simulate the resist profile for an applied dose distribution.

3.2.1. Principles and consequences of the proximity effect

The electron beam rasterizes the designed structures and exposes the resist at each raster point through the deposited energy in its interaction volume. The energy is deposited in this interaction volume according to a deposited energy distribution which can be ascribed to two processes; inelastic forwardscattering and elastic backscattering. [**17**] The incident electrons experience small-angle forwardscattering which broadens the primary beam size (~100 nm). As the electrons penetrate the resist and enter the substrate some of them undergo large-angle scattering events. These electrons can return back to the resist exposing it in places far from the incident spot where the primary beam has entered (~3 µm). [**18**] In order to get an overview, electron-resist and electron -substrate interactions were simulated by Monte Carlo simulations. The results are presented in the appendix in chapter I), on page 104. A typical interaction volume of an incident beam can be seen in figure 18.

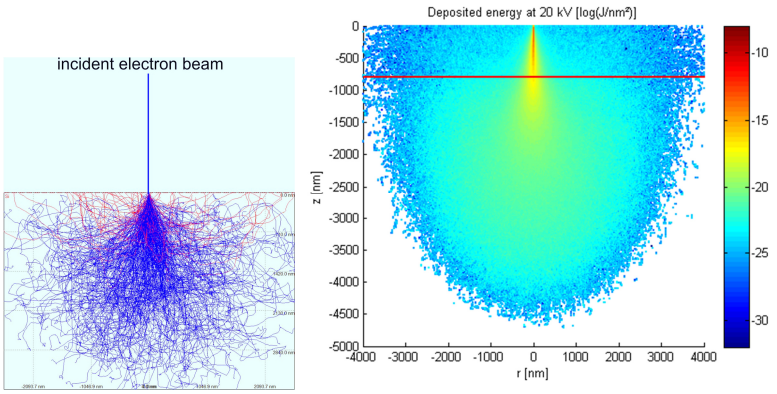

Figure 18: Illustration of the interaction of the electrons of the incident beam with 800 nm thick PMMA resist on a SiO_2 substrate (simulated with Casino). Left; the trajectories of the electrons are marked blue. Right; the deposited energy plotted as a function of radial distance of the incident electron beam and depth in the resist. The substrate-resist interface is marked with a red line.

In order to illustrate the proximity effect, consider a simplified, normalized deposited energy distribution of an incident electron beam as shown in figure 19 on the left and further suppose that the deposited energy is independent of the depth in the resist and radially symmetric. In figure 19, 50 % of the incident energy is deposited by the forwardscattered electrons within a radial distance of 5 nm around the incident spot and the other 50 % are deposited by the backscattered electrons within a radial distance of 2.5 µm. Hence, the deposited energy distribution of an incident electron beam due to the contribution forward scattered electrons has a magnitude of 6000 and the contribution of the backscattered electrons one of 0.05.

The total deposited energy distribution at a point P is obtained by summing up the deposited energy contributions at this point P of all exposed raster points around it. Consider an exposure with a step size of 10 nm (see figure 19). The forwardscattering contributions of the exposed raster points do not overlap and consequently, the forwardscattering contribution of the total deposited energy is equal to the forwardscattering contribution of an exposed raster point within a structure and zero elsewhere. Whereas the backscattering contributions of the exposed raster points overlap and the backscattering contribution of the total deposited energy in a point P is therefore the sum over all the backscattering contributions of the exposed raster points within its backscattering interaction radius. In other words, the backscattering contribution of the total deposited energy in a point P is the backscattered contribution of a single exposed raster point multiplied by the number of raster points within its backscattering interaction radius (2.5 µm). For example, a point P in the center of a square with a side length of 1 µm is exposed by 10^4 raster points and the backscattered contribution of the total deposited energy would be 0.05 (backscattering contribution of a single exposed raster point) times 10^4 (the number of point within its interaction radius, see figure 20). Hence, even if the backscattering contribution to the deposited energy of an exposed raster point is magnitudes lower (10^{-5}) compared to the contribution of the forwarscattered electrons around the incident beam, their contribution to the total deposited sums up over large distances eventually getting important.

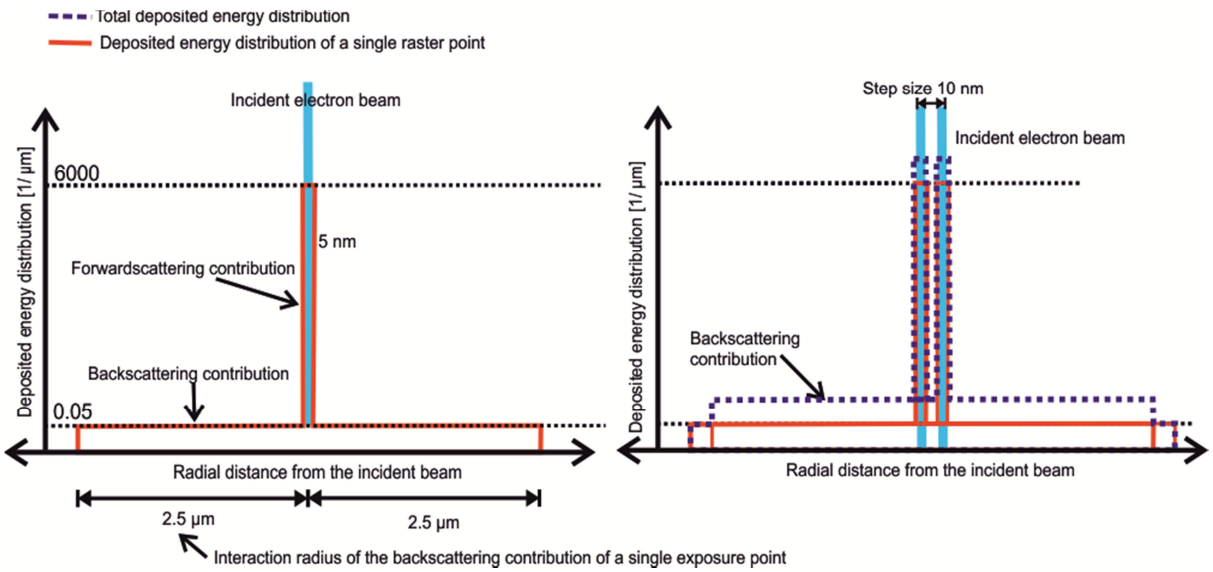

Figure 19: Right; simplified deposited energy distribution of an incident electron beam (not to scale). Left; exposure of two raster points with a step size of 10 nm. The total deposited energy is obtained by summing up the energy distributions of the single raster points. Thus, the backscattering contribution of the total deposited energy is increased.

The simplified model above considered the deposited energy to be independent of depth in the resist. In fact, in this case the deposited energy is directly related to the resist height (see chapter 3.2.3). The proximity effect has the following consequences:

- Size dependence: The deposited energy in large structures (figure 20 structure R1) is overall higher than in smaller ones (figure 20 structure R2), even if they have the same homogenous designed dose distribution. For that reason, smaller structures require a higher dose than larger ones to achieve the same resist height and width. A square with a length of 1 µm / 100 nm is exposed by 10^4 / 10^2 single exposed raster points (step size 10 nm). The backscattered contributions of all single exposed raster points overlap in the whole structure and thus can be added up. Therefore, the backscattering contribution of the total deposited energy in a square with a size of 100 nm is 100 times smaller than in a square with a size of 1 µm.
- Cross talk: Exposed structures influence each other. Consider two rectangles as shown in figure 20 (structure R3 and R4). Rectangle R3 is exposed by 10^4 single exposure points which all expose rectangle R4 through their backscattered electrons. Thus, rectangle R4 receives approximately 10 % more total deposited energy than the free standing rectangle R2.
- Proximity tails: Regions which in principle were not addressed by the electron beam are exposed through the backscattered electrons. This exposure is more pronounced around large structures since their total long ranging backscattered contribution is higher (see figure 20 structure R1 and R2).
- Edge effect: A point being at the center of these rectangles (> 2.5 µm) is exposed by all other single exposure points around it through their backscattering contributions, whereas a point at the edge misses its neighboring single exposed raster points. For that reason, the actual total deposited energy distribution at the edges is always lower than at the center (see figure 20 R5).

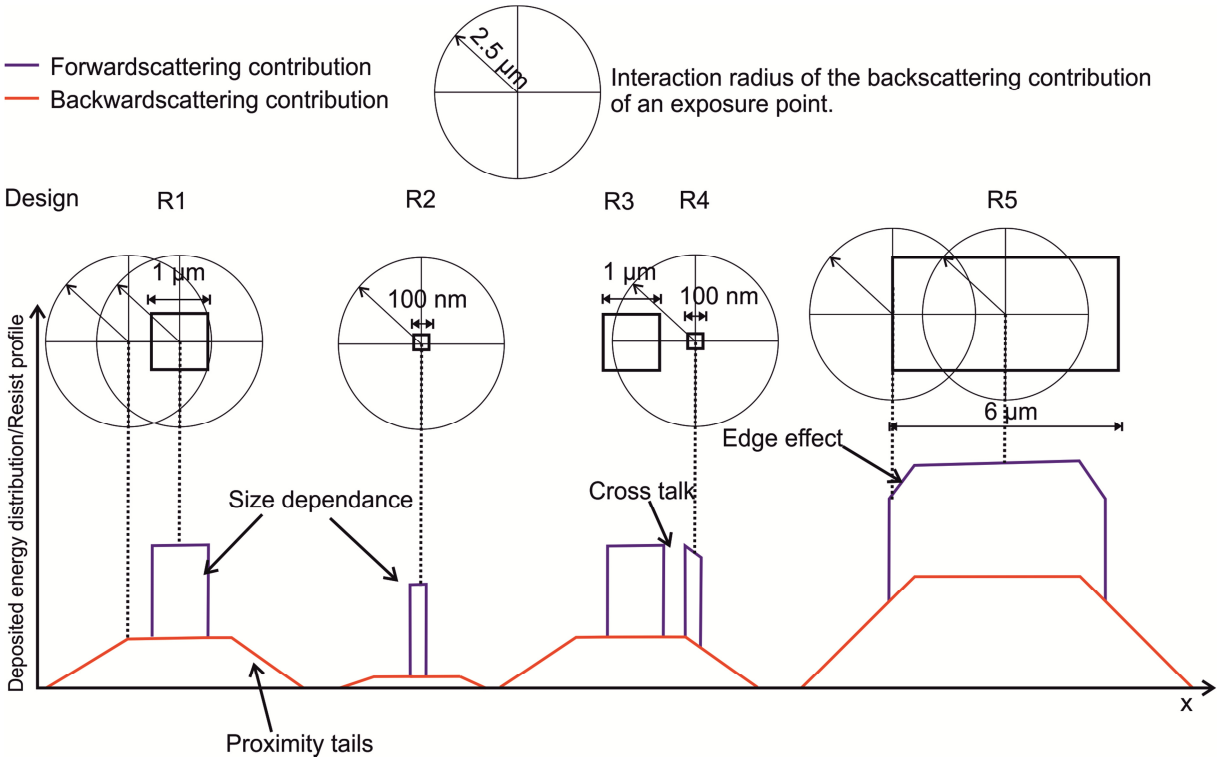

Figure 20: Illustration of the proximity effect (not to scale). The cross section of the deposited energy distribution of the designed rectangles supposing simplified interaction volume as shown in figure 19 and a linear dependence between the resist height / profile and the deposited energy.

Microfluidic devices typically consist of channels with varying lateral dimensions between 500 nm and 10 µm. Hence, it is inevitable to take into account the proximity effect which is done by a proximity correction. The proximity correction requires an accurate knowledge of the deposited energy distribution profile of an incident beam. This profile is described mathematically by the proximity function. The parameters of this function have to be measured experimentally by a doughnut test. Once the proximity function is determined one can calculate the deposited energy distribution via a so called energy density simulation and further one can compensate the proximity effect by fine tuning the dose of the structure in a way that the designed pattern is revealed after development. Additionally, if the contrast curve, which describes the relation between the resist height and the deposited energy, is known one can deduce the resist profile of an exposed structure after development. The whole process is shown in figure 21. The same approach is also described by R. J. Hawryluk [**16**] and by K. Vutova [**19**].

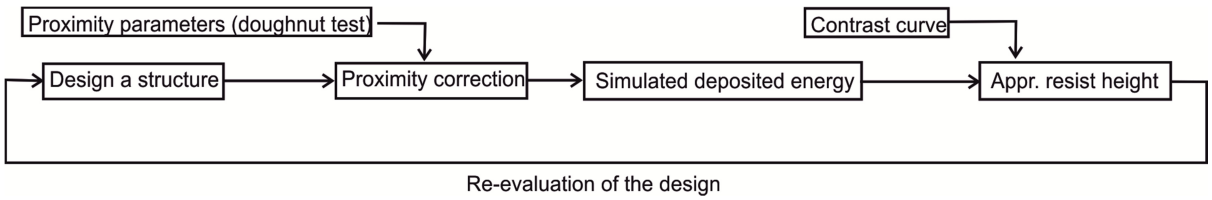

Figure 21: Proximity correction procedure.

3.2.2. Proximity function

The proximity function describes the profile of the deposited energy distribution of an incident electron beam at a certain depth in the resist. It is assumed that the deposited energy is symmetric and solely a function of the radial distance r from the incident beam. This function is approximated by two Gaussian terms and sometimes additionally by a third Gaussian or an exponential term [**16**], [**20**], [**21**], [**22**]:

Equation 3-3) $$f(r,z) = \frac{1}{\pi(1+\eta+\nu_1+\nu_2)}\left(\frac{1}{\alpha^2}e^{-\left(\frac{r}{\alpha}\right)^2} + \frac{\eta}{\beta^2}e^{-\left(\frac{r}{\beta}\right)^2} + \frac{\nu_1}{\gamma_1^2}e^{-\left(\frac{r}{\gamma_1}\right)^2} + \frac{\nu_2}{2\gamma_2}e^{-\left(\frac{r}{\gamma_2}\right)}\right)$$

z… depth in the resist. r … radial distance from the incident beam; η… ratio between deposited energy forwardscattered electrons and backward scattered electrons; β… standard deviation of backscattered electrons distribution; α … standard deviation of forwardscattered electrons distribution; γ_1… standard deviation third Gaussian term; ν_1… weight of the third Gaussian term; γ_2… standard deviation of the exponential term; ν_2… weight of the exponential term; All parameters depend on the depth z in the resist.

The first term of equation 3-3 can be assigned to forwardscattered electrons and the second one to backwardscattered electrons. The behavior of the proximity function has been simulated in the appendix chapter I), on page 104. It turns out that η is decreased slightly with increasing acceleration voltage and it increases slightly with the depth in the resist. The backscattering parameter β is increases with increasing acceleration voltage and decreases with increasing depth in the resist. The forwardscattering parameter α decreases with increasing acceleration voltage and increases with depth z in the resist. As a consequence backscattered electrons have a larger interaction volume at high acceleration voltages but the energy deposited in a volume within a distance β (see figure 22 on the right) from the incident electron beam is lower compared to low acceleration voltages. Additionally, the forwardscattering around the incident beam is reduced using high acceleration voltages. For that reason high acceleration voltages should be preferred. The simulation results have been confirmed by the group of K. Vutova [**17**], by the group of M. Parikh [**22**] and by R. J. Hawryluk [**16**] and agree with experimentally obtained data.

Figure 22 shows a typical proximity function at a certain depth in the resist.

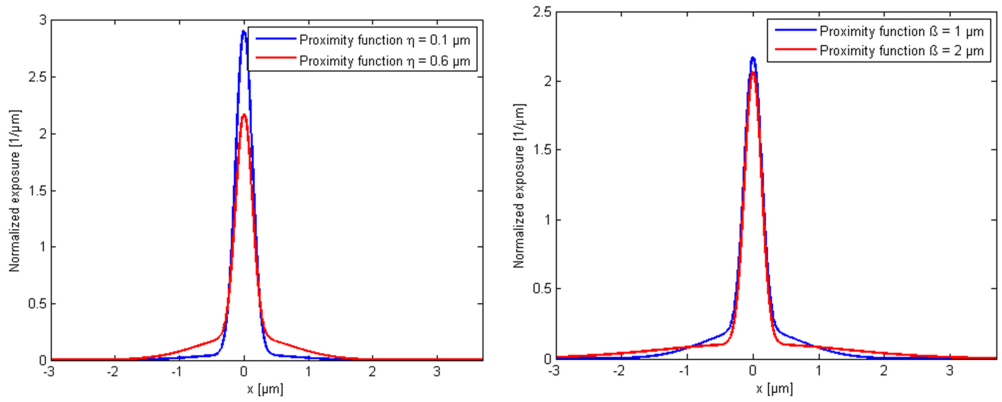

Figure 22: Typical proximity function described by two Gaussians. Left; the η parameter has been varied (α = 180 nm β= 1 µm). Right; the β parameter has been varied (α = 180 nm β= 1 µm).

Some important details concerning the proximity function:

- The Gaussian distributions are a consequence of random scattering processes whereas exponential distributions are more likely due to absorption processes. An exponential distribution is therefore encountered for backscattering electrons of substrates with heavy atoms like GaAs. [**20**], [**22**]
- The electron beam distribution is supposed to be Gaussian. The forwardscattering parameter is actually a convolution between the actual forwardscattering and the beam intensity distribution. [**22**]

  Equation 3-4) $$\alpha = \sqrt{{\alpha_{f.scatter}}^2 + {\alpha_{Beam}}^2}$$

  Where $\alpha_{f.scatter}$ represents the forwardscattering and α_{Beam} is due to the Gaussian beam distribution. Hence, the forwardscattering parameter is strongly influenced by the beam shape and by the beam size. [**22**]

The total deposited energy distribution at a point r is assumed to be calculated through equation 3-5 [**20**].

Equation 3-5) $$E(r,z) = k \int D(r',z) f(r-r',z) dr'^2$$

k … represents the charge to energy conversion factor; $f(r-r',z)$ … proximity function at a certain depth in the resist z; $D(r',z)$ … dose applied at the point r' in a certain depth in the resist; z … depth in the resist.

Equation 3-5 already implies that the deposited energy of all exposure points can be summed up and that the energy is linear with the electron flux. [**16**] Thus k is a scaling factor converting the dose which is measured in units of [As] to deposited energy [J]. [**20**] The scaling factor k and therefore also the actual deposited energy cannot be measured. It is therefore practical to use the deposited dose instead of deposited energy:

Equation 3-6) $$D_{deposited}(r,z) = \frac{E(r,z)}{k}$$

The deposited energy distribution (it is also called deposited dose distribution) can be simulated automatically by the Raith Nanopecs software package upon injecting the proximity function. It is important to mention that if the designed dose distribution is changed by a scaling factor, the simulated energy distribution is simply re-scaled by the same factor due to the linear relationship between the deposited energy E(r) and the applied dose D(r).

Please note: The proximity function is also called point exposure distribution [**20**], energy intensity distribution [**23**] or energy deposition function [**24**].

3.2.3. Contrast curve

The contrast curve is either defined as the relation between the resist height and the deposited dose or as the dependence between the deposited dose and the solubility rate of the resist. In fact, both definitions are similar. An increasing solubility rate also leads to a decreasing resist height and vice versa. [**19**] The method to measure these contrast curves is elucidated in this chapter.

The solubility of the resist is a function of the deposited dose. The deposited dose is connected to the applied dose via the proximity function. However, the proximity parameters are not known at this point and as a consequence it is not possible to calculate the actual deposited dose in the resist. One can get around this problem by using a large area exposure. The latter is done by exposing a large structure with a homogenous dose (e.g. a 10 µm x 10 µm rectangle):

Equation 3-7) $\mathrm{D_{applied}(r,z)} = D_0(z) \quad r \in Structure$ and $\mathrm{D_{applied}(r,z)} = 0 \quad r \notin Structure$

D_0(z) … homogenous dose applied in a depth z of the resist; z … depth in the resist. $\mathrm{D_{applied}(r,z)}$ … dose applied at a point r in the resist depth z.

The deposited dose at a certain resist depth in the center of the structure can then be calculated through: [**17**]

Equation 3-8)
$$D_{deposited}(r',z) = \int \mathrm{D_{applied}(r,z)}\, f(r-r')dr^2$$
$$D_{deposited}(r',z) = D_0(z) \int f(r-r')dr^2 = D_0(z) \quad r' \epsilon\, center$$
$$\rightarrow D_{deposited}(r',\mathrm{z}) = D_{applied}(r',\mathrm{z}) = D_0(z) \quad r' \epsilon\, center$$

$D_{deposited}$… deposited dose at a point r'; $D_{applied}$ … applied dose; z … depth in the resist; D_0 … homogenous dose applied in the whole structure

Equation 3-8 uses the fact that the proximity function is normalized. It further assumes that the structure is large enough (> 4 ß [**21**]) for the integral to be equal to 1, i.e. an exposed point in the center re-receives its lost energy by the exposed points around him and thus, the deposited dose is equal to the applied dose D_0(z) at a point in the center of the structure.

The solubility rate is defined as the rate the resist dissolves in the developer in [m/s]. The dependence of the solubility rate on the deposited dose is given by the solubility contrast curve. The solubility in a depth z of the resist is then given by:

Equation 3-9) $S(z) = C_{solubility}\left(D_{deposited}(z,r')\right) = C_{solubility}\left(D_0(z)\right) \quad r' \epsilon\, center$

S(z)… solubility rate at a depth z in the resist; $C_{solubility}$ … solubility contrast curve; $D_0(z)$ … deposited dose in a resist depth z in the structure (equal to the applied dose in the center)

Measuring the contrast curve using equation 3-10 is difficult since the deposited dose changes with depth in the resist. Each resist layer would have to be evaluated on its own for every applied dose. [**16**] For that reason it is assumed that the deposited energy is uniform in the resist with respect to z. Simulations carried out in the appendix chapter I), on page 104, showed that this approximation is reasonable. If the applied / deposited dose is assumed to be uniform in the resist, the solubility rate is independent of the depth in the resist. Hence, the solubility contrast curve can be measured by

comparing the resist height prior and after development at a certain deposited dose D_0 (in the case of a negative resist):

Equation 3-10) $$S = \frac{h_{pre} - h_{post}}{t_{dev}} = C_{solubility}(D_0)$$
$$\rightarrow D_0(z) = D_0 = D_{applied} = D_{deposited}$$

h_{pre} … height of the resist prior to development; h_{post} … height of the resist after development; S … solubility rate; $C_{solubility}$ … solubility contrast curve; D_0 … uniformly deposited dose in the resist; t_{dev} … development time (time the resist is dissolved by the developer).

In the case of a negative resist, the resist height contrast curve is measured by measuring the final resist height after development as a function of the deposited dose:

Equation 3-11) $$h_{post} = C_{height}(D_0)$$

h_{post}… height of the resist after development; C_{height} … resist height contrast curve; D_0… deposited dose.

Thus, using the resist height contrast curve and assuming that the deposited dose is uniformly distributed in the resist with respect to z, one can approximate the resist height for a certain deposited dose. The deposited dose can be calculated by the Nanopecs software using the proximity function. The value of the contrast itself is defined as the slope of the resist height-logarithmic applied dose graph (see figure 23) (as defined in reference [**25**]):

Equation 3-12) $$\gamma = \frac{1}{log10\left(\frac{D_i}{D_c}\right)}$$

γ… contrast; D_i… incipient dose: Dose where the resist is completely developed / saturated; D_c… dose where the resist just starts to stick (clearing dose).

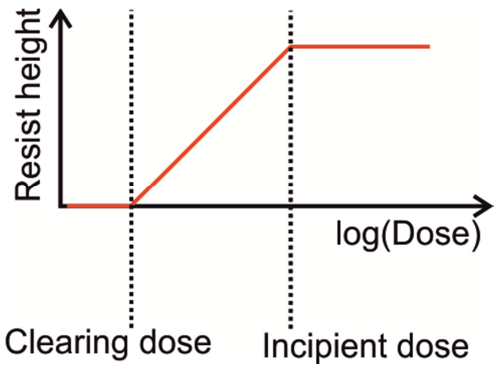

Figure 23: Definition of the contrast for a negative resist.

3.2.4. Doughnut test

The proximity parameters necessary to calculate the deposited energy and further approximate the resist height can be simulated by Monte Carlo simulations [**17**], [**22**] [**21**] or determined experimentally. Simulations require an exact knowledge of the density and the composition of the resist as well as the substrate. This data is not available for the resist and neither for the substrate used in this master thesis. For that reason, the parameters have to be measured.

There are different methods to determine the proximity parameters $(\beta, \alpha, \gamma, \eta, \dots)$ which are summarized in the following list:

- The doughnut test uses a doughnut structure. The inner radius and the dose are varied.
- Using rectangles or lines with different distances and doses. Data points are obtained similar to the doughnut test but the fitting formula is very complicated [**26**].
- Using a large rectangle or lines and measuring the corresponding width at different doses. This method requires SEM metrology techniques [**26**], [**27**].
- PROX-In method which is basically done automatically by a commercial software called PROX-IN. Details are discussed in reference [**28**].
- Point exposure [**20**]: An array of points is exposed for a large range of doses. The radius of the points after development is measured as a function of the dose. This procedure seems simple but it is believed to be very sensitive to exposure variations.

The most adequate method in our case is the doughnut test since it doesn't require line or point exposures which can be washed off during development especially in the case of thick resists. The doughnut test consist of a doughnut where the inner circle is unexposed and the outer circle exposed. The center of the doughnut is therefore only exposed through the proximity effect by the outer circle (see figure 24).

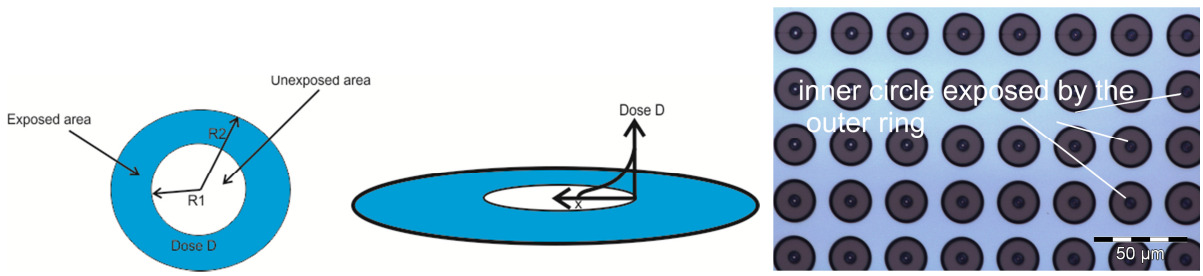

Figure 24: Left; Principle structure of a doughnut test. The outer ring is exposed whereas the inner ring is unexposed. The inner ring is exposed through the proximity effect. Right; image of a doughnut test made with an optical microscope. The inner circle is exposed by the proximity effect through the outer circle.

In order to calculate the deposited energy in the center of the inner ring, it is assumed that the dose is deposited uniformly with respect to depth in the resist. However, the deposited dose is still different in each resist layer since the proximity parameters continue to depend on the depth in the resist. Hence, it is further supposed that the proximity function can be described by an average proximity function independent of the depth in the resist. [**26**], [**16**] The three dimensional problem is therefore reduced to a two dimensional problem. Using these assumptions, the dose received at the center can be calculated through equation 3-13. [**26**], [**29**]

Equation 3-13) $$D_{center} = \int D_{app}(r) f(r - r') dx dy$$

D_{center} ... deposited dose at the center of the inner circle; D_{app} ... homogenous applied dose at the outer ring; $f(r)$ ... normalized average proximity function.

If the radial symmetry is taken into account, one obtains (R1 is the inner radius and R2 is the outer radius): [**29**]

Equation 3-14) $$D_{center} = 2\pi \int_{R1}^{R2} D_{app}(r)\, f(r) r dr$$

Provided that R2 is large enough (>4 β), the second boundary R2 can be ignored and one obtains equation 3-15 which can be used to determine the proximity parameters. [**29**], [**26**]

Equation 3-15) $$D_{center} = D_{app}\left[\frac{1}{1+\eta+\cdots}\left(e^{-\left(\frac{R1}{\alpha}\right)^2} + \eta e^{-\left(\frac{R1}{\beta}\right)^2} + \cdots\right)\right]$$

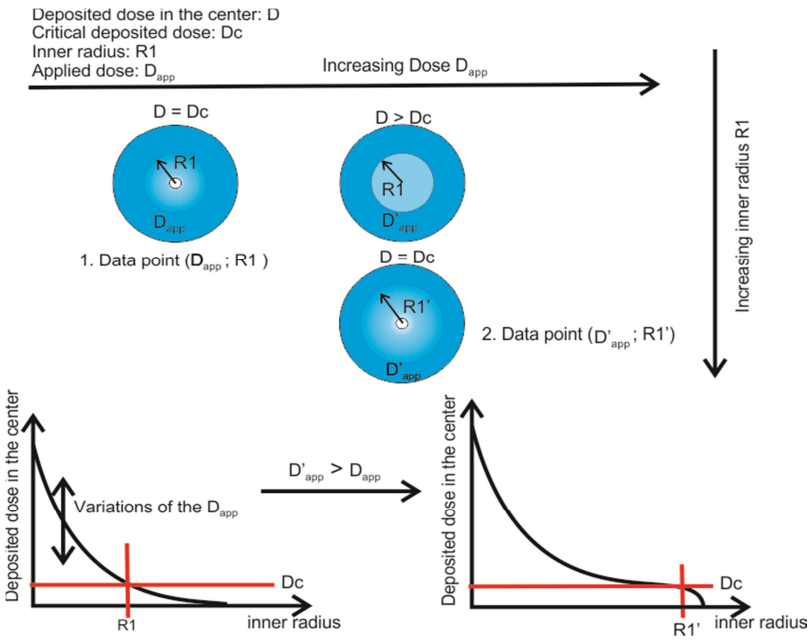

Figure 25: Doughnut test; the data points are found by searching the doughnuts whose deposited dose in the center D corresponds to a pre-defined value D_c. In other words the function of equation 3-15 is scanned.

Intuitively one would think that with these equations one can determine the proximity parameters by fitting the deposited dose in the center (D_{center}) as a function of R1 for a constant D_{app}. But this is not the case since the deposited dose at the center cannot be determined. One could argue that measuring the height with AFM and knowing the contrast curve would be a possibility to determine the deposited energy in the center of the doughnut, but the hole is too small and the slope too steep to get reliable results. For that reason a certain deposited energy D_c has to be defined. It's not the point to know the value of D_c at the moment, but only to define D_c in a way that it can be re-identified if the inner radius or the outer dose D_{app} is changed. Usually D_c is set to be the energy where the center of the ring just starts to get free of resist i.e. the clearing energy. Once this energy D_c is defined one can set $D_{center} = D_c$. Subsequently, the proximity function can be scanned by

changing the inner radius and the outer dose D_{app} (figure 25): If the outer exposure dose D_{app} is increased, the function equation 3-15 is "shifted down". A data point of equation 3-15 can be found by re-identifying D_c and the corresponding radius R1. The data pairs D_{app}, R1 can then be used to fit the proximity parameters. In order to do so it is useful to rearrange the terms above into a form like in equation 3-16.

Equation 3-16)
$$D_{app} = D_c \left[\frac{1}{1+\eta+\cdots} \left(e^{-\left(\frac{R1}{\alpha}\right)^2} + \eta e^{-\left(\frac{R1}{\beta}\right)^2} + \cdots \right) \right]^{-1}$$

It turned out that it is actually important to know the value of D_c in order to get stable fit results. This is actually not a problem if D_c was chosen to be the critical energy which can be determined by a contrast curve which has to be measured anyway. This contrast curve should be exposed together with the doughnut test minimizing the uncertainty of contrast / sensitivity variations between the exposures.

There is another issue which is very important to mention; the doughnut test has to be carried out for each acceleration voltage, aperture, working distance and step size. The working distance and the aperture influence the beam intensity distribution and thus the α parameter. The influence of the step size is not that obvious. Consider, for the sake of simplicity, a line structure with a step size of 20 nm and another one with a step size of 2 nm. Each exposure point of the 20 nm line further receives 10 times more dose than the points of the 2 nm line. This ensures an overall equal applied dose. A line is a 1D problem leading also to a different normalization of the proximity function ($\sqrt{\pi}$ instead of π). The proximity functions overlap differently at a step size of 20 nm than at a step size of 2 nm. This leads to different deposited energy / dose at the end of the lines (figure 26). Thus, the proximity function determined by the doughnut test is not really the distribution function of a point dose it's rather the effective distribution function of an ideally infinitesimal small area. The actual size of this area is believed to be related to the step size. This is actually no limitation as long as the structures simulated are larger than this area.

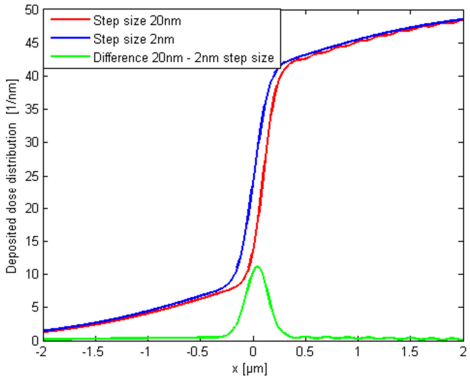

Figure 26: Exposure distribution of a line with a step size of 2 nm and 20 nm.The exposures differ remarkable at the end of the line in a range of 400 nm. The line starts at x = 0 µm and ends at x = 5 µm.

As a conclusion one can state that the proximity function determined by the doughnut test is not an actual three dimensional dose distribution function of an incident electron beam. It is the average deposited dose distribution function of a small area whose size is determined by the step size the doughnut test has been exposed with.

3.2.5. Proximity correction

There are basically two possibilities of proximity corrections. On the one hand one can use the proximity correction software available in the Nanopecs software and on the other hand one can adjust the dose for each structure depending on its size and on its surroundings. The principle of the proximity corrections is shown in figure 27.

The proximity corrections discussed here use the average two dimensional proximity function. Advanced proximity corrections require a three dimensional proximity function as well as development models. Such complex approaches have been described by the group of K. Vutova [**17**], R. J. Hawryluk [**16**] and I. Raptis [**24**]. S. Babin and coworkers [**30**] also incorporated beam induced temperature effects.

The solubility of the resist depends on the deposited energy. A uniform deposited energy in the resist, thus a two dimensional model implies that the resist height / profile is directly related to the deposited energy via the contrast curve. Hence, it is possible to approximate the final resist profile after development by linear interpolation of the contrast curve. This approximated resist height is used to verify the proximity corrected structures and to tune the absolute applied dose.

The calculation of the approximate resist height is discussed first. Then the proximity correction via the Nanopecs software is explained. In the end the proximity correction via dose adjustment is presented.

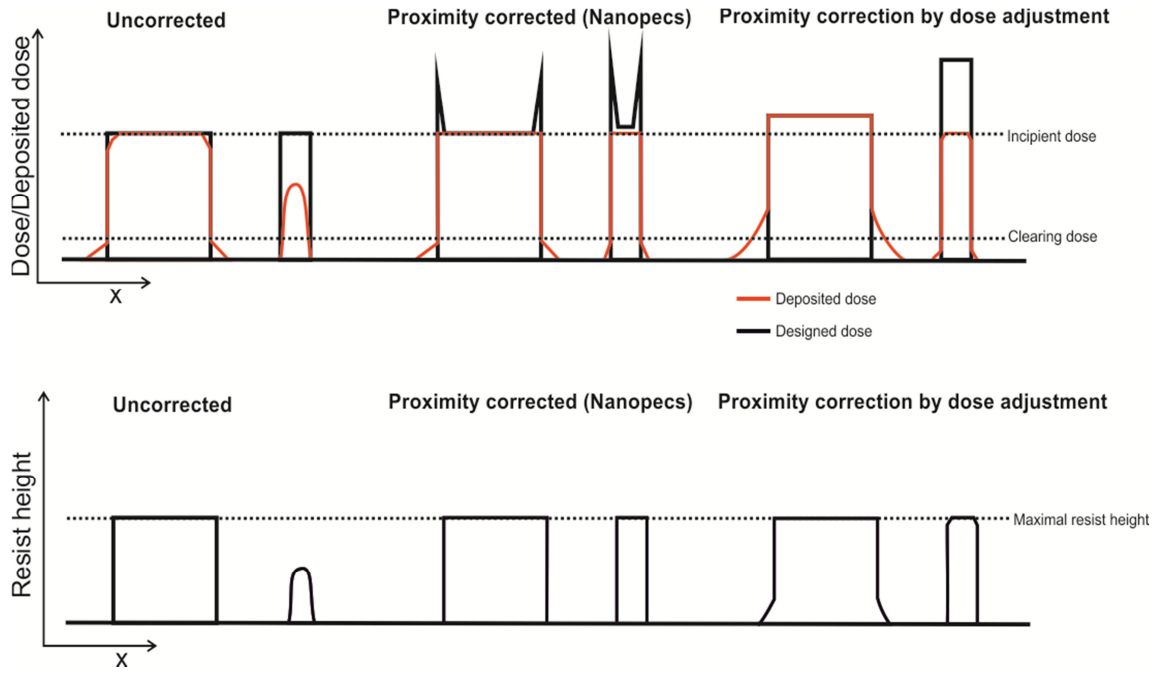

Figure 27: Principles of proximity correction (cross section); Uncorrected structures have rounded edges and their final resist height depends on their widths'. Whereas, all Nanopecs proximity corrected structures have the same height as well as defined edges since they have a uniform deposited dose distribution. Dose adjustment proximity corrected structures have the same final resist height independent of their widths' and also well defined edges but the proximity effect gets important for large structures.

3.2.5.1 Determine the approximate resist height

All elements are designed using normalized doses. The absolute dose the structure is exposed with is then obtained by multiplying the normalized dose with the base dose which is set prior to exposure. Hence, the energy density simulation of the Nanopecs software simulates the normalized deposited dose distribution of a given normalized dose distribution. This simulated normalized deposited dose distribution has to be multiplied by the base dose in order to obtain the absolute deposited dose. Once, knowing the absolute deposited dose, one can obtain the resist height by linear interpolation of the contrast curve. The latter can't be done by the Nanopecs software. For that reason one has to export certain cross sections of the simulated deposited normalized dose and evaluate them by an external software.

3.2.5.2 Proximity correction with the Nanopecs software

The goal of the proximity correction is to achieve a conformal map of the designed structures. The profile of the developed structures is directly related to the solubility of the resist and therefore further to the deposited dose. Thus, a replication of the designed structures is achieved by equalizing the deposited dose distribution to the designed dose distribution, i.e. the applied dose distribution has to be tuned in a way that the corrected deposited dose distribution corresponds to the designed dose distribution.

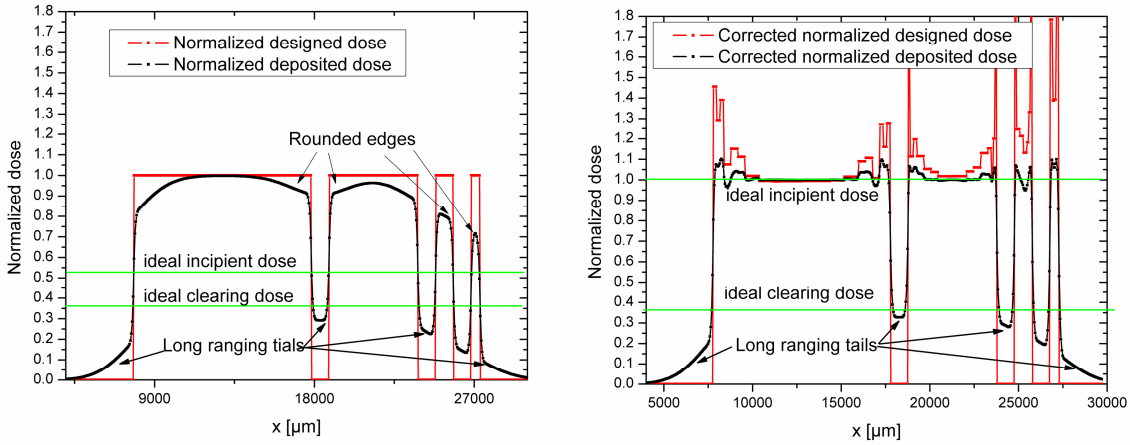

Figure 28: Cross section of the designed dose distributions and actually deposited dose distributions of rectangles of different sizes (simulated by the Nanopecs software with a resolution of 50 nm). The ideal deposited dose window of the resist between incipient and clearing dose are marked with green lines. Left; not proximity corrected rectangles. The deposited dose is smaller for small rectangles and the edges are rounded. The long reaching tails expose the gaps in between the rectangles. Right; cross section of the designed dose and the deposited dose of proximity corrected rectangles. The deposited dose is equal to 1, independent of the rectangle size. The long ranging tails are only slightly more pronounced compared to the uncorrected ones.

Taken the rectangles with a normalized dose of 1 from figure 28 on the left; the simulated normalized deposited dose is not uniform in the rectangles and depends on their size and neighboring rectangles. For example, the deposited dose at the edges is lower compared to the center and the smaller rectangles on the right receive less deposited dose than the large ones on the left. The goal of the proximity correction is a uniform normalized deposited dose distribution in the rectangles of 1 independent of their size. This is done by fracturing the rectangles into small sub elements each assigned to a dose which meets the actual dose requirement (e.g. the sub elements

at the edge receive a higher normalized dose compared to those in the center of a rectangle (see figure 28 on the right)).

Automatic proximity effect correction algorithms are for example presented by G. Owen [**31**], by R. Wüest and coworkers [**23**] and by G. P. Watson [**32**]. The normalized dose of the fractured rectangles is either calculated by an iterative process [**23**], [**32**] or by convolution with Fast-Fourier-Transformation [**31**]. All these methods have in common that they equalize the normalized deposited dose in the exposed structures. Unexposed areas are not taken into account, i.e. the long ranging tails due to the backscattered electrons reaching out of the structures are ignored (see figure 28). In fact, it is impossible to compensate these long ranging tails because they are a consequence of the physical interaction volume. [**31**] The long ranging tails have to be eliminated by the contrast of the resist, i.e. the clearing dose has to be higher than the deposited energy in these tails (see figure 27). That is the reason why proximity corrections are carried out using normalized doses. The absolute applied dose distribution is adjusted by the base dose prior to exposure so as to cut off the tails and at the same time reach the required resist height (the absolute applied dose is the normalized applied dose multiplied by the base dose).

The proximity correction is therefore carried out as follows (see figure 29); first, the structure is designed using a normalized dose distribution. Then, the Nanopecs proximity correction corrects the designed normalized dose distribution in order to obtain a corrected normalized dose distribution. Subsequently, the normalized corrected deposited dose distribution is simulated using the Nanopecs software. The absolute corrected deposited dose distribution is then calculated by multiplying the normalized corrected deposited dose distribution with the base dose. Subsequently, the resist profile is approximated by linear interpolation of the contrast curve. The base dose is varied until the result is satisfying, i.e. until the long ranging tails are cut off and the desired resist height is achieved.

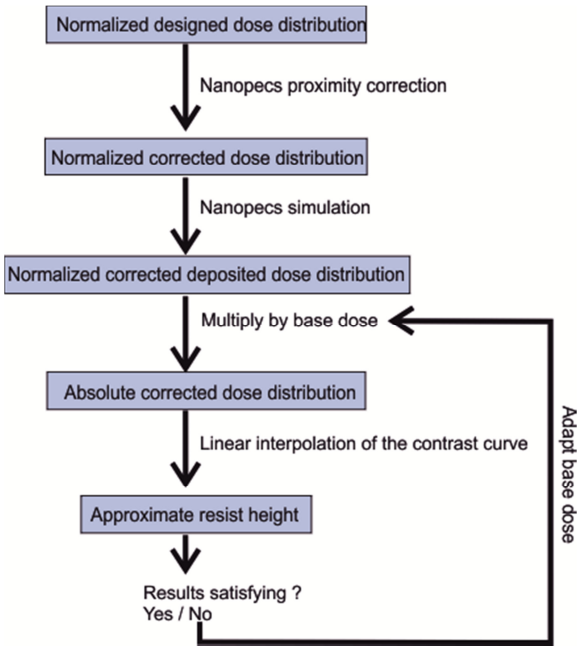

Figure 29: Proximity correction using the Nanopecs software. See text above for details.

Proximity corrected structures do not necessarily require a high contrast resist as uncorrected do (shown in figure 28). The normalized deposited dose in corrected structure is uniform and independent of their lateral dimensions and the ideally required incipient dose is therefore higher compared to uncorrected ones. At the same time, the ideal clearing dose required to cut off the tails, is only slightly larger compared to uncorrected structures. Thus, the ideal contrast required for proximity corrected structures is lower than for uncorrected ones.

3.2.5.3 Proximity correction by dose adjustment

Proximity correction can also be done by assigning each structure a proper dose according to its shape and size. The required dose is determined by simulating the resist profile. The normalized dose of the structure as well as the base dose are adjusted in a way that the approximate resist profile corresponds to the desired result. A rectangle with a length of 10 µm and a width of 500 nm would have a normalized dose 4 times higher than a rectangle with a width of 5 µm and length of 10 µm, for example. The advantage of this system is that one doesn't need to fracture the structures reducing the writing time.

The major disadvantage is illustrated in figure 30. If defined edges are required, the overall designed dose of the structure has to be chosen higher compared to a Nanopecs corrected structure leading to an overall higher deposited dose and thus to a more pronounced proximity effect. As a consequence, the ideal contrast of a dose adjusted structure has to be higher than the ones corrected with the Nanopecs software. This is especially important when dealing with large (> 1 µm) structures having pronounced and long ranging proximity tails. Another disadvantage is that designing multiple joined elements with different dimensions is impossible.

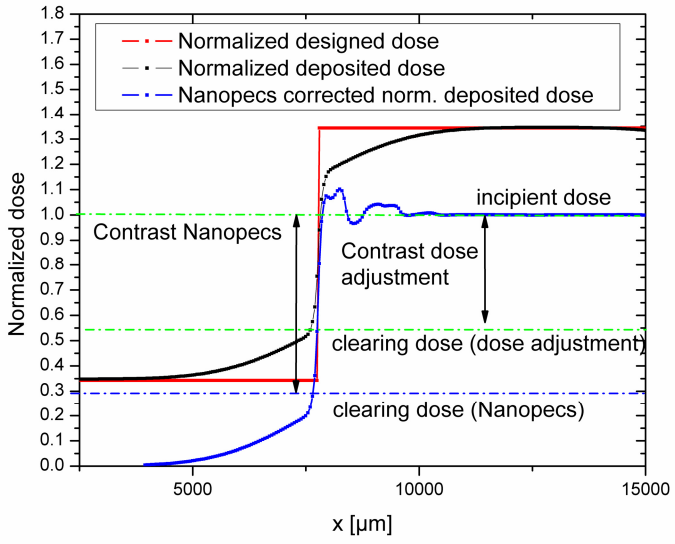

Figure 30: Proximity correction via dose adjustment compared to proximity correction with the Nanopecs software. The dose adjusted structure requires an overall higher designed / deposited dose than a Nanopecs corrected one. The ideal, required contrasts are marked with dotted lines.

3.3. System characterization

Before writing complex structures with electron beam lithography it is essential to characterize the system. The term system used here, includes the E-Line itself as well as the resist, the development process and the substrate.

The whole characterization process is shown in figure 31 and will be elucidated in detail in the following chapters.

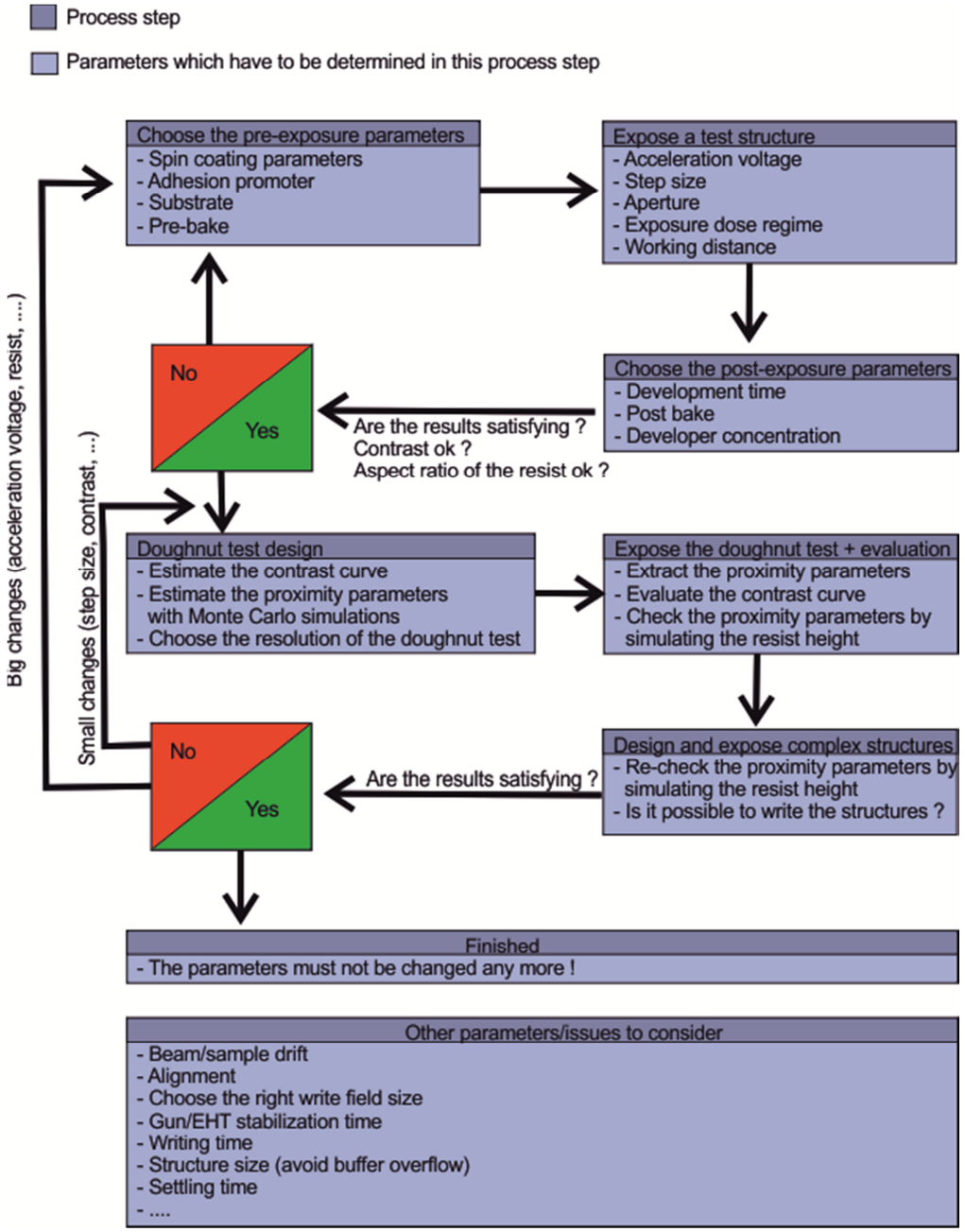

Figure 31: System characterization process; the title of the rectangles correspond to a process steps and the elements of the list of this rectangle represent the parameters which have to be optimized / determined. The details will be explained step by step in the text below.

3.3.1. Pre-exposure parameters

The first step is to select the resist and the substrate which should be well defined and smooth. Thus, Si wavers with thermally grown SiO_2 on-top were used. The resist should meet the following requirements:

- Thick resist: The aspect ratio of channels of PDMS Sylgard 184 is around 1:12. Thus, writing channels with lateral dimensions of a few micrometers requires at least a resist thickness of about 1 µm.
- High contrast: Sharp and well defined edges and thus a high contrast are required to exploit the whole range of the aspect ratio of the PDMS channels. Thick resists always have a lower contrast. Hence, there is a trade-off between resist thickness and contrast.
- High sensitivity: Microfluidic systems take a long time to write. It's therefore preferable to use a resist which is sensitive in order to reduce the writing time.

The negative resist AR 7520.18 from the company All-Resist meets these requirements and was used in this work.

The samples were cleaned with the standard procedure prior to spin coating (see appendix in chapter VIII), on page 114). The spin coating was done immediately after cleaning. The spin parameters were chosen to be 1000 RPM for 50 s with a maximal acceleration leading to a resist height of around 870 nm. This resist has to be pre-baked prior to exposure for 1 min at 85 °C on a hotplate. This pre-bake determines the sensitivity of the resist and has to be done as exact as possible.

One can use HMDS (Hexamethyldisilazane) as an adhesion promoter for the resist, but it changes the contact angle of the Ag ink on the SiO_2 surface causing problems with inkjet printing which is done later on (see chapter 5, sub chapter 5.2, on page 61 for details).

3.3.2. Test structure and post exposure parameters

The test structure should give an overview of the system used. The goal of such a test structure is neither to determine the proximity parameters nor to measure the contrast curve. It is favorable to characterize the resist by sweeping a large parameter space by a fast written test structure rather than by a time consuming doughnut test or contrast curve. An image of the test structure made with the optical microscope is shown in figure 32.

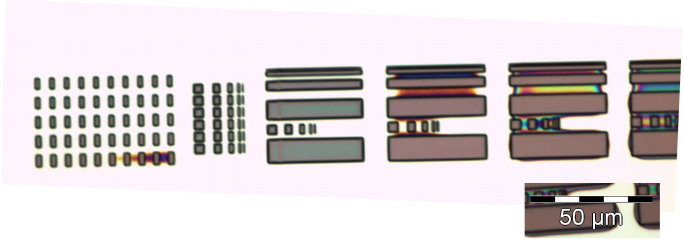

Figure 32: Test structure; exposure parameters: 20 kV; base-dose: 60 µC/cm², aperture: 10 µm; post-exposure parameters: developed for 2 min.; developer (AR 300-47) to water ratio 4 : 1.

The test design shown in figure 32 was exposed at different acceleration voltages and base doses on two separate chips. The contrast of the first chip developed for 90 s was not high enough. For that reason, a second test chip was exposed. The second test chip which was developed for 120 s increasing the contrast. The results of these two test chips are discussed in the following.

3.3.2.1 First exposed test chip

The design of figure 32 was exposed at acceleration voltages of 20 kV, 25 kV and 30 kV at base doses ranging from 20 µC/cm² to 60 µC/cm² on the first test chip which was developed for 90 s in a developer diluted with water (4:1). The resulting test structures were measured by AFM.

The test structure exposed at 20 kV with a base dose of 20 µC/cm² compared to a test structure exposed at 30 kV is shown in figure 33. One can see that the dose required to obtain the full height of the resist (the incipient dose) is higher for 30 kV than for 20 kV. Another interesting detail which is shown in figure 33 is that the proximity effect at 20 kV gets remarkable before the structure reaches its maximum height. The proximity correction through dose variation is therefore impossible and it is questionable if the proximity correction via fracturing could still reach well defined edges.

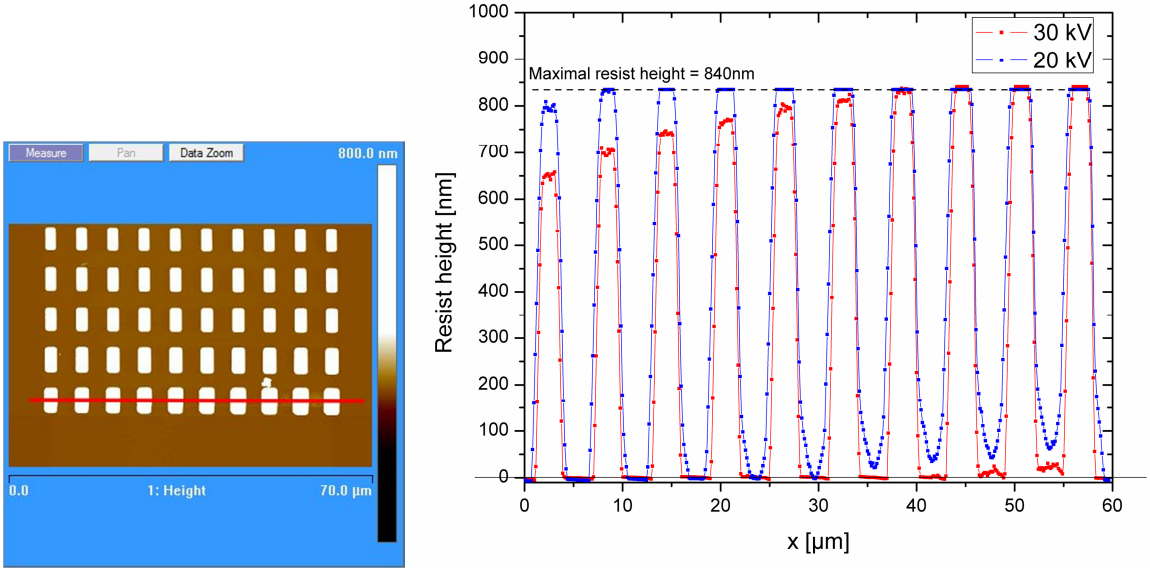

Figure 33: Left; AFM image of the first test design. Right; cross section marked by a red line on the left. The cross section has been measured on a structure exposed at 30 kV (red line) and at 20 kV (blue line). Both were exposed at a base dose of 20 µC/cm². The applied dose of the rectangles varied from 41 µC/cm² to 80 µC/cm² from the left to the right with a dose step size of 4 µC/cm². The dose necessary to reach the maximal resist height is higher at 30 kV (75 µC/cm²) than at 20 kV (54 µC/cm²). The proximity effect on the other hand is more pronounced at 20 kV.

Furthermore, figure 34 is a nice demonstration of the proximity effect. It's not only the „tail" which creates problems, smaller structures on the right also receive less deposited energy than bigger ones. This problem occurs at 20 kV as well as at 30 kV. Another interesting detail which can be seen in figure 34 (marked with 1), is that the usually lower proximity effect has a longer range at 30 kV which can cause problems writing large structures close to each other (first two structures from the left). As soon as the structures get smaller (first three structures from the right), the proximity effect at 30 kV gets overtaken by the proximity effect at 20 kV.

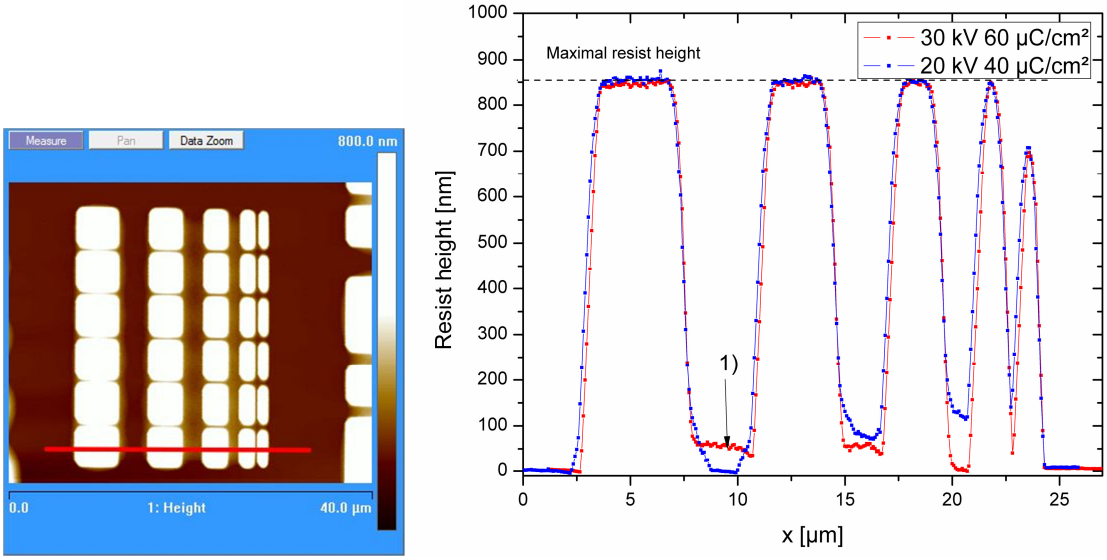

Figure 34: Left; AFM image of the first test chip. Right; cross section marked by a red line on the left. The cross section was measured on a structure exposed at 20 kV with a base dose of 40 µC/cm² (blue) and on a structure exposed at 30 kV with a base dose of 60 µC/cm² (red). Smaller structures receive less exposure at 20 kV as well as at 30 kV than large ones. 1) The proximity effect at 30 kV has a longer range than at 20 kV causing problems using large structures close to each other.

3.3.2.2 Second exposed test chip

The same structures as on the first test chip have also been exposed on the second test chip. The only difference was a longer development time of 120 s intending to increase the contrast. In order to check if the contrast has been increased, AFM measurements of the first test developed for 90 s structure were compared to AFM measurements of the second test structure developed for 120 s. The results are shown in figure 35. One can easily see that the contrast has been increased. The resist height has been decreased at the same time for about 50 nm. However, it is believed that a decrease of 50 nm could also be due to other process variations like developer temperature.

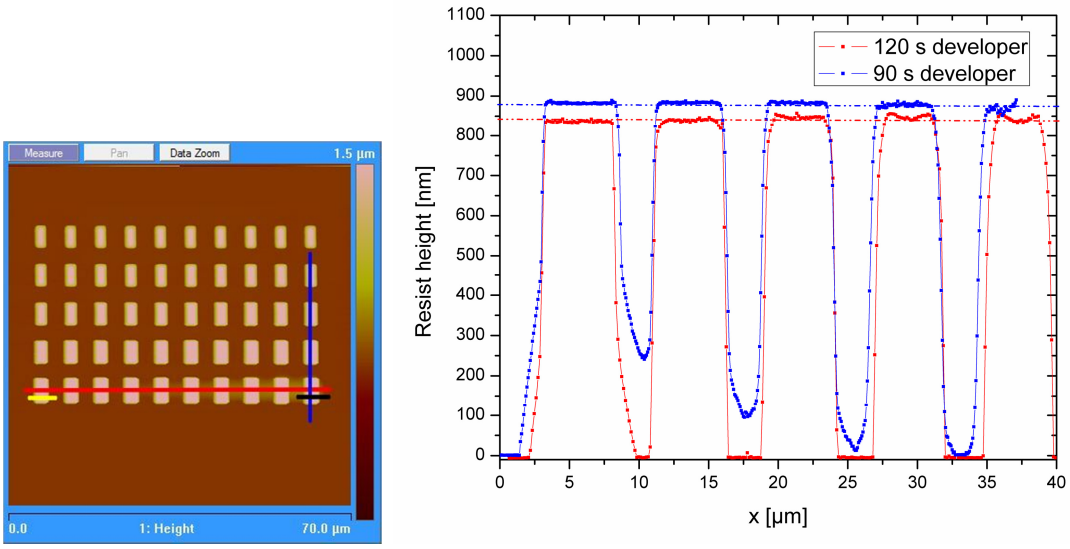

Figure 35: Left; AFM image of the second test chip. Right; cross section marked on the left by a blue line. The cross section has been measured on a structure exposed at 20 kV with a base dose of 50 µC/cm² on the first (blue) and second test chip (red). The first test chip has been developed for 90 s and the second one for 120 s. The contrast has obviously been improved by the longer development time.

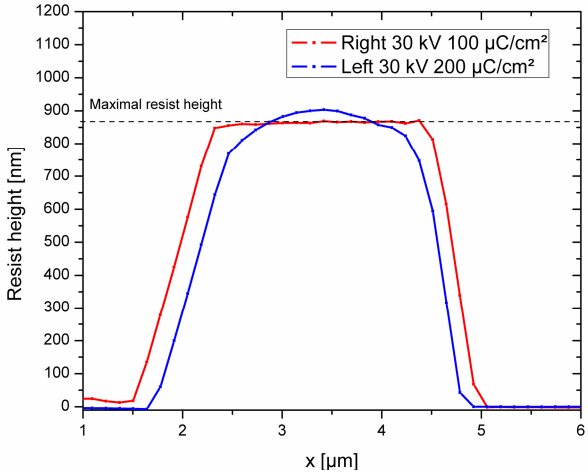

Figure 36: Cross sections marked in figure 35 with yellow and black lines. The resist height decreases with increasing dose but the surface gets smoother.

Figure 36 shows the cross section of a rectangle exposed at different doses. It is interesting to note that the resist height is decreased with an increasing dose if the dose has exceeded the saturation dose. The surface, however, gets smoother. Increasing the dose further doesn't lead to a further reduction of the height. This unexpected effect could be due to a cross-linking related reduction in specific volume. This is of course very speculative. It has however been observed that the edges of large structures which receive less deposited energy are usually higher than the center. This deviation is however very small (~30 nm).

3.3.2.3 Conclusion pre- / post- exposure parameters

The first intuition would be to take an acceleration voltage of 30 kV. But it turned out that the beam current at 30 kV, using an aperture of 10 µm, is too high. One can't apply doses below 50 µC/cm² with a reasonable step size below 10 nm due to the minimal dwell time. The dose adjustment and the proximity correction are also vague since the dose gets discrete with a large step size due to discrete dwell time values (see chapter 3.1.2). Another problem using 30 kV is that the beam booster is deactivated at acceleration voltages higher than 20 kV, rendering the Inlens-detector useless. Using the off-axis secondary electron detector to do aperture alignment, focusing, write field alignment and other tasks is difficult and time consuming because the image contrast is not as good compared to the Inlens detector. It was therefore the better choice to use 20 kV as the acceleration voltage. The imaging is better easing write field alignments and the testing of other software features.

The pre-, post- and exposure parameters are summarized in the following list:

- Substrate: SiO_2, no adhesion promoter
- Spin coating: 1000 RPM, 50 s
- Pre-bake: 85 °C, 1 min
- Exposure: 20 kV acceleration voltage, 9.6 nm step size, Dose variations around 50 µC/cm²
- Development: 2 min at RT in a diluted developer (AR 300-47) to water ratio 4:1

Once these parameters are fixed, one can measure the contrast curve and determine the proximity parameters by a doughnut test.

3.3.3. Proximity parameter and contrast curve determination

It's practical to expose the design used to measure the contrast curve and the doughnut test on the same substrate since the evaluation of the doughnut test requires the knowledge of the incipient dose to extract the proximity parameters.

The results of the contrast curve measurement will be discussed first. The results of the doughnut test are elucidated subsequently.

3.3.3.1 Contrast curve measurement

The contrast curve has been measured by exposing squares with a size of 10 µm. The applied dose of these squares has been swept from 9 µC/cm² to 58 µC/cm² with a dose step size of 1 µC/cm². The design used to measure the contrast curve is shown in figure 37. The contrast curve was determined by measuring the height in the center of each rectangle with the AFM. The resulting contrast curve is shown in figure 38.

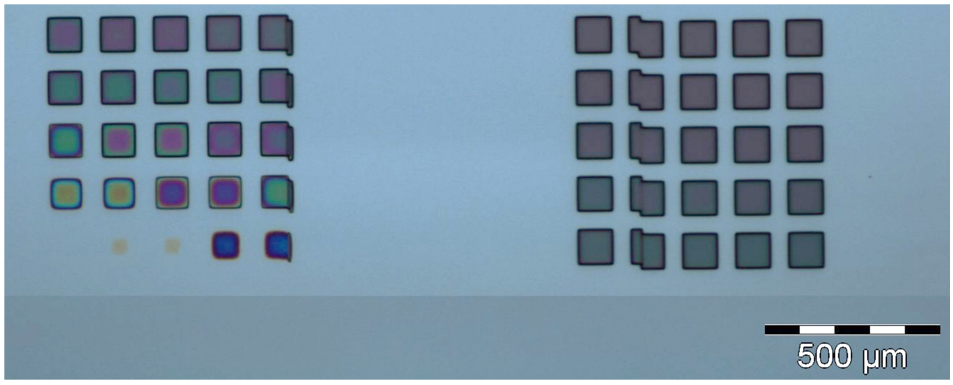

Figure 37: Contrast test; rectangles with a size of 10 µm x 10 µm have been exposed. The dose has been swept from 9 µC/cm² to 50 µC/cm² with a dose step of 1 µC/cm² starting at the lower left corner. The dose was increased from the right to the left and from bottom to the top. The stitching error is due to a long writing time of the doughnut test (beam drift).

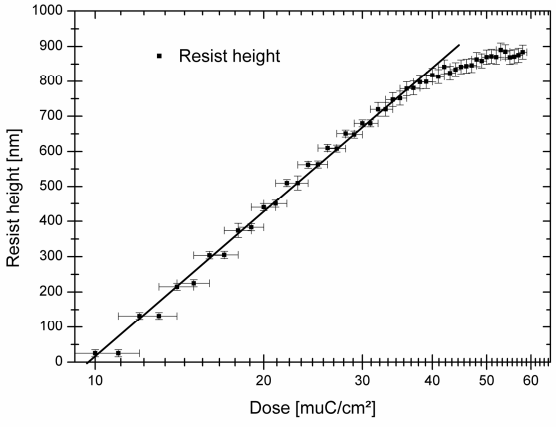

Figure 38: Contrast curve measured by AFM; the thick black line marks the contrast. The maximal resist height is 850 nm.

The incipient dose is 40 µC/cm² and the critical dose is 9 µC/cm² yielding a contrast γ of 1.7 (see figure 38). The data sheet promises a contrast around 5. It is believed that this discrepancy is due to the high resist thickness (the contrast is decreased with increasing resist thickness).

A step size of 2 µC/cm² is below the resolution of our electron microscope: The minimum dwell time is 400 ns which corresponds to a shutter frequency of 2.5 MHz and the minimum dwell time step size is 100 ns which correspond to a modulation frequency of 1 MHz. Consequently the dose step size is:

Equation 3-17) $$\Delta D = \frac{I}{(\Delta x \Delta y)} \Delta t \sim 2\mu C/cm^2$$

ΔD… dose step size; $\Delta x \Delta y$ … area step sizes (in this case they were 9.6 nm each); I … beam current (~30 pA)

For that reason almost each 2nd rectangle had the same height as the previous one. The discrete dose step size is a problem concerning the resist height simulation and the proximity correction. The discrete dose step size is taken into account as an uncertainty factor in the resist height simulation, i.e. the applied dose and therefore also the simulated deposited dose is considered to have an uncertainty of $\Delta D = \pm 1$.

3.3.3.2 Proximity parameters determination – Doughnut test

The doughnut test used to extract the proximity parameters is designed and fabricated as discussed in the appendix in chapter VII), sub chapter 11.1.1, on page 113. Figure 39 shows a developed doughnut test.

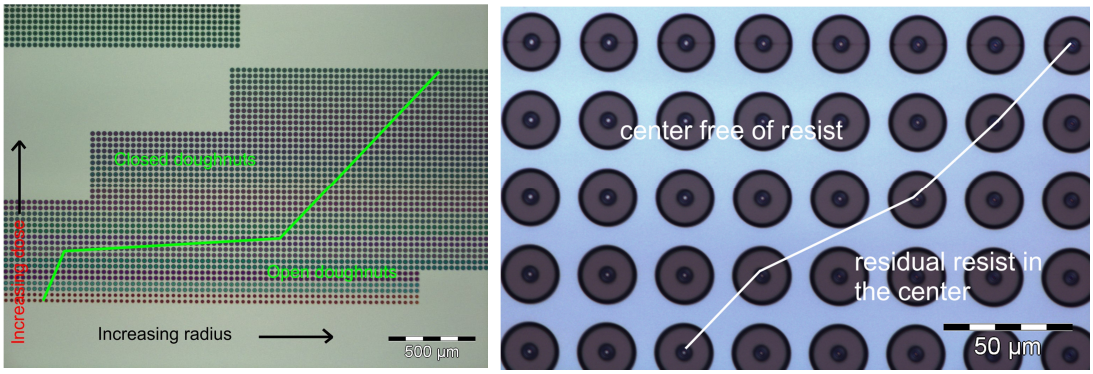

Figure 39: Exposed doughnut test. The data points are extracted by following the line between the doughnuts whose centers just start to get free of resist and those whose centers are still covered by residual resist.

The evaluation of the doughnut test is done as described in the appendix in chapter VII), sub chapter 11.1.2, on page 115. The data points (R, D_{app}) used to fit equation 3-18 are obtained by following the line between the doughnuts whose centers are free of resist and those whose center is just covered by resist. The results are presented in figure 40 and fitted with equation 3-18. The fitting was carried out as described in the appendix in chapter VII), sub chapter 11.1.3, on page 115. It turned out that the data is described best by a proximity function with 3 Gaussians using D_c as a fixed parameter. The results are listed in table 1.

Equation 3-18) $$\frac{D_{app}}{D_c} = \left[\frac{1}{(1+\eta+\nu_1+\nu_2)}\left(e^{-\left(\frac{R}{\alpha}\right)^2} + \eta\, e^{-\left(\frac{R}{\beta}\right)^2} + \nu_1\, e^{-\left(\frac{R}{\gamma_1}\right)^2}\right)\right]^{-1}$$

$\eta, \nu_1, \nu_2, \alpha, \beta$ … proximity parameters to be determined by fitting, R … inner radius of the doughnut; D_{app}…applied dose to the outer circle; D_c… deposited dose at the center of the doughnut. Chosen to be the incipient dose where the resist just starts to stick (determined by the contrast curve 9 µC/cm²); $\frac{D_{app}}{D_c}$ … normalized dose.

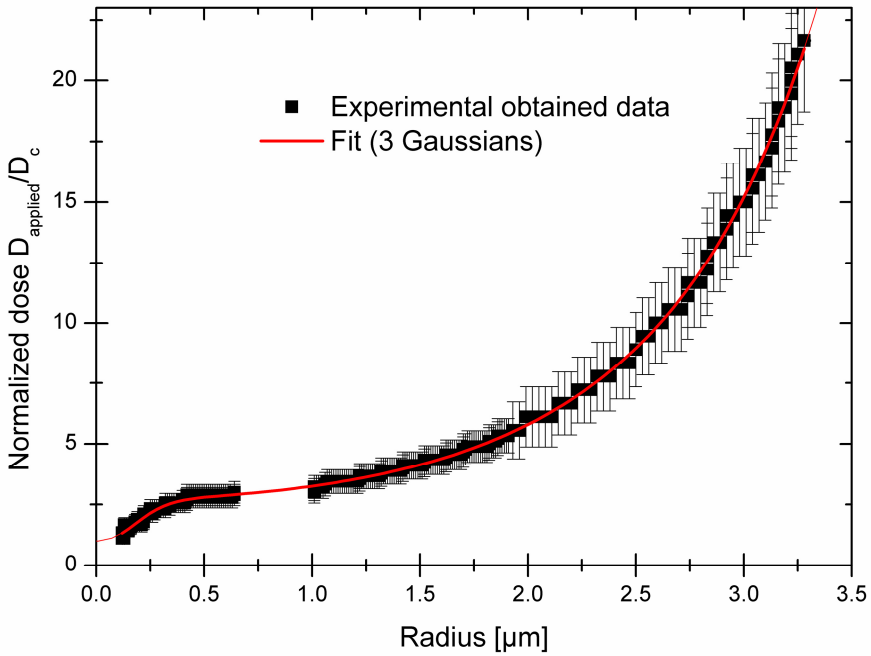

Figure 40: Experimentally data obtained by the doughnut test. The function marked with a red line has been fitted with equation 3-18. The resulting fit parameters are listed in table 1.

Table 1: Fit results of the doughnut test using equation 3-18. D_c was determined with the contrast curve (9 µC/cm²). The shape of the experimental determined proximity function can be described by the fitted proximity function.

Parameters	3 Gauss terms [µm]
α	0.15±0.01
β	2.278±0.005
η	0.93±0.3
γ_1	0.24±0.03
υ_1	0.57±0.46
D_C	9 µC/cm²
Adj. R Square	0.99565

3.3.4. Proximity parameters verification

The proximity parameters are verified by comparing the simulated resist height to the actual resist height measured by AFM and the results are shown in figure 41. The agreement is surprisingly good and the resist height is within the error bars. The error bars are due to the discrete step size of the applied dose.

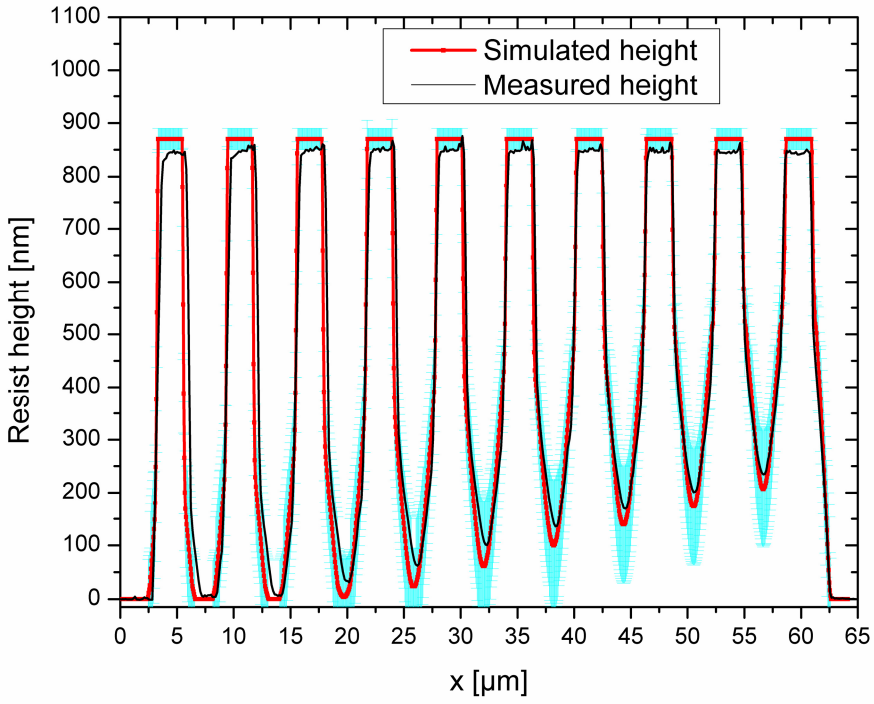

Figure 41: The cross section of the structure shown figure 33 on the second test chip marked with a blue line measured by the AFM (black line) compared to the simulated resist height (red line). The error bars are marked with light green.

Once the proximity parameters were verified, two test chips with proximity corrected rectangles and not proximity corrected rectangles with a length of 10 µm and a varying width ranging from 5 µm down to 100 nm were designed. The doses of these rectangles were varied from 30 µC/cm² to 44 µC/cm² on chip 1 and from 44 µC/cm² to 134 µC/cm² on chip 2. Such a structure is shown in figure 42.

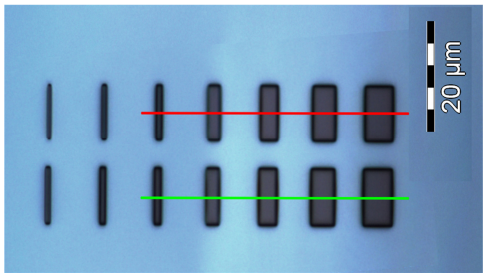

Figure 42: Proximity (lower) and not proximity corrected (upper) rectangles exposed with a base dose of 44 µC/cm². The rectangles widths' ranging from 5 µm to 1 µm (first 5 rectangles from the right) were examined with the AFM. The cross sections examined by the AFM are marked with lines. The rectangles with a width of 500 nm, and 750 nm (first two from the left) were examined with the SEM. Rectangles smaller than 500 nm have been washed off during development.

Rectangles which are proximity corrected by the Nanopecs software with a designed dose of 30 µC/cm² should have a uniform deposited dose distribution of 30 µC/cm² and therefore a resist height of 670 nm independent of their size. If the samples are not proximity corrected, the structures' actual size and height should depend on their designed size. The rectangles bigger than 1 µm (first 5 rectangles in Figure 42) were examined with the AFM and compared to the simulated resist height. Rectangles smaller than 1 µm can't be examined by the AFM anymore because instead of the resist profile the profile of the AFM tip is measured. The results are shown in figure 43 and are as expected.

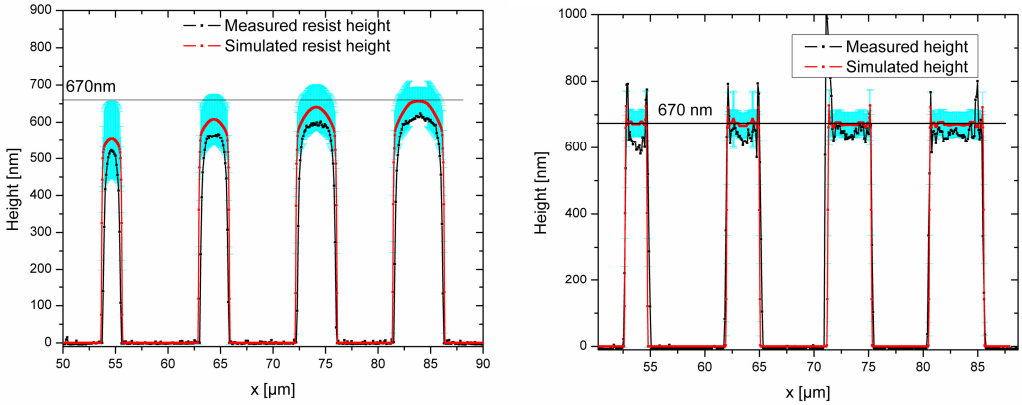

Figure 43: Comparison simulated resist height (red) and resist height measured by the AFM (black) of rectangles with a width ranging from 1 µm to 5 µm exposed at a base dose of 30 µC/cm².. Left; not proximity corrected rectangles. Right; proximity corrected rectangles.

Another interesting aspect to examine is to look if the results are reproducible. This is why the rectangles exposed at base dose of 44 µC/cm² of chip 1 were compared to those of chip 2. The results are shown in figure 44. One can see that the measured resist heights of chip 1 and 2 are both within the error bars of the simulated deposited energy. The height of chip 2 is about 50 nm higher than those of chip 1. This difference is most likely due to varying development parameters like temperature or developer dilution.

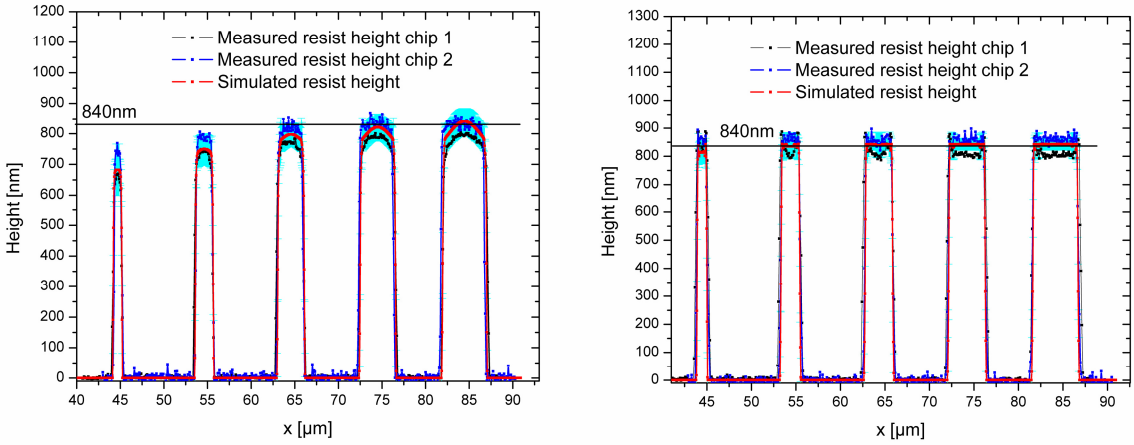

Figure 44: Comparison simulated resist height (red) and resist height measured by the AFM (black) of rectangles with a width ranging from 1 µm to 5 µm exposed at a base dose of 44 µC/cm². Right; proximity corrected rectangles. Left; not proximity corrected rectangles.

It is actually a pity that the height of the structures below 1 µm can't be measured by AFM. They have to be examined by the SEM (see figure 45). The width of the proximity corrected rectangles corresponds to the designed width at a base dose of 33 µC/cm² as well as at 44 µC/cm². Not proximity corrected rectangles aren't present at a base dose of 33 µC/cm². The latter can be seen at a dose of 44 µC/cm² but their width does not agree with the designed width.

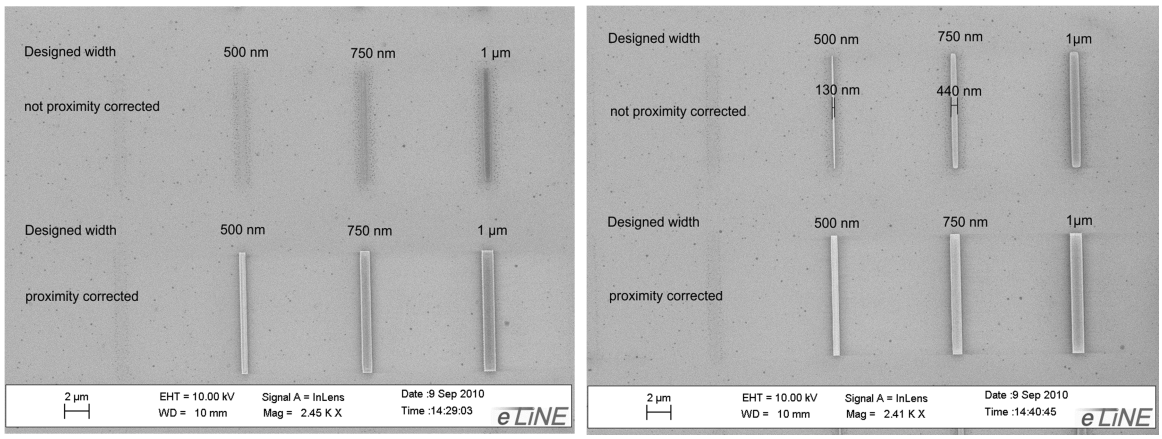

Figure 45: SEM images of proximity and not proximity corrected rectangles with a base dose of 30 µC/cm² (left) and 44 µC/cm².

As far as structures with dimensions below 500 nm are concerned, the proximity correction was not done correctly because the step size of 9.6 nm was in the same range as the fractured elements (10 nm). A SEM image of chip 2 is shown in figure 46. One can see that 250 nm wide rectangles start to appear at a dose of 74 µC/cm². The problem is that the aspect ratio of the resist seems to be around 3.5 consequently the resist starts to bend (figure 46 on the right). The measured width corresponds to the designed and simulated width. Despite the obtained result it is believed that the simulated width does not necessarily fit the actual resist height in structures below 250 nm because the results are very sensitive to the α parameter which is not known exactly. Further, the simulation raster used to calculate the deposited energy by the energy density simulation is limited to about 10 nm because smaller step sizes require a very long calculation time. Simulating these structures can be done by using another algorithm based on FFT convolution. This algorithm calculates 100 nm rectangles with a raster size of 2 nm in about 10 s and not days.

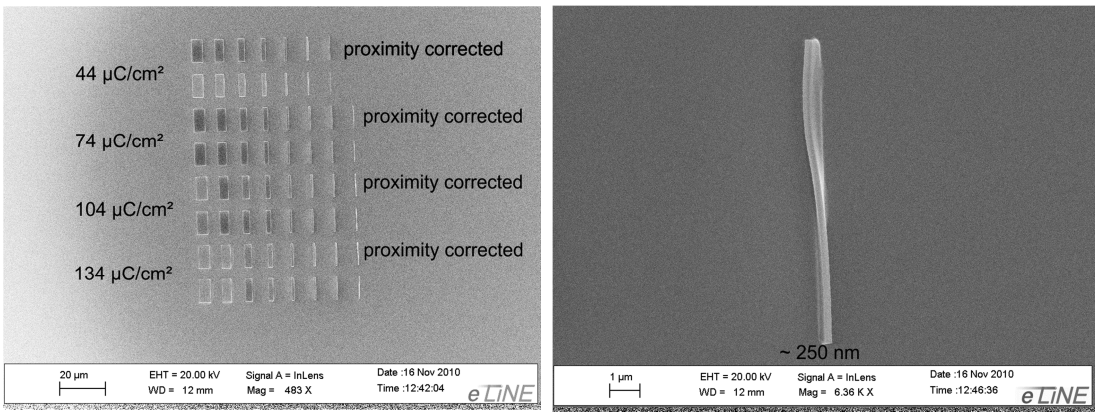

Figure 46: Images of chip 2 made by SEM. The sample has been tilted in order to obtain the image. Left; overview of the chip. Structures with a size of 250 nm start to appear at doses of 74 µC/cm². Right; 250 nm wide rectangle exposed at a dose of 74 µC/cm². The width can't be measured exactly since the sample as well as the rectangle is tilted.

3.3.5. Conclusion system characterization

The major challenge when dealing with micro- / nano- fluidic systems structured by EBL is that they are typically composed of structures / channels with lateral dimensions ranging from sub micrometers up to tenths of µm. Proximity corrections and resist profile simulations are therefore inevitable to actually replicate the designed structures. Furthermore typical microfluidic structures extend over a few mm's requiring long writing times (>24h). Hence, automatic alignment procedures to compensate for drifts are necessary.

For that reason, the electron beam lithography unit (E-Line) and the resist had to be characterized. First the pre- and post- exposure parameters for a 840 nm thick Novolac Ar 7520.18 resist were optimized. Subsequently, the contrast curve and the proximity parameters have been determined by a doughnut test. In order to verify the results, simulated resist profiles were compared to profiles of actual developed structures measured by AFM. The agreement between the simulations and the AFM measurements was surprisingly good. It has also been possible to compensate the proximity effect by a proximity correction and thus, to expose rectangles with lateral dimensions ranging from 500 nm up to 10 µm while keeping the designed integrity.

As mentioned above, drift compensation is an important issue when dealing with long exposure times. For that reason the E-line provides automatic alignment procedures. These procedures were successfully tested. With these alignment procedures, it has further been possible to expose two consecutive aligned exposures, e.g. pending bridges exposed at 5 kV with pillars exposed at 20 kV have been fabricated.

4. PDMS as a material for microfluidic systems

Polydimethylsiloxane (PDMS) has been widely used as a mold material in microfluidic systems. Its major advantage over materials such as silicon and glass is the simple, fast and inexpensive fabrication process via replica molding which allows rapid prototyping. The PDMS Sylgard 184 from Dowcorn used in this master thesis, is transparent down to 280 nm allowing fluorescence microscopy. [**33**], [**34**] Furthermore, it remains stable and flexible at temperatures ranging from -55°C to 200°C [**35**] and it is also suited for biological applications since it is biologically inert and non-toxic. [**34**] Further, it is permeable to gases which is useful when supplying oxygen to cell cultures in closed systems. [**34**] Another interesting property of PDMS Sylgard 184 is that it does not adhere to Novolac or PMMA (poly-methyl-methacrylate) based polymers / resists upon curing, allowing a convenient replication of masters structured by electron-beam lithography. [**36**] An additional aspect regarding the replication is that PDMS is elastic. On the one hand the elasticity allows an easy peel off but on the other hand it's also a major drawback leading to defects of the PDMS replica / mold due to collapsing and sagging of replicated features. [**2**], [**36**] Furthermore, PDMS molds can be bonded to substrates like SiO_2, Si, glass, PMMA by oxygen plasma activation. [**1**], [**34**]

One disadvantage of PDMS is its hydrophobicity, which impedes water based solutions from penetrating the channels due to a high negative capillary pressure. [**37**] Furthermore, some organic solvents and some hydrophobic analytes get adsorbed by the hydrophobic channel walls leading to fouling. [**34**] This, however, can be circumvented by rendering the PDMS hydrophilic which is done by oxygen plasma activation for example. [**1**]

The PDMS Dowcorn Sylgard 184 pre-polymer initially consists of a liquid base and a liquid curing agent which undergo a curing process getting an elastomeric and solid PDMS-polymer upon mixing. In this chapter, the curing process will be discussed first and the relevant surface modification, oxygen plasma activation, and its uses like rendering the PDMS hydrophilic and bonding, are discussed subsequently. Furthermore, the limitations of PDMS regarding replica molding are discussed in the end.

4.1. Curing process

The PDMS pre-polymer consists of a base and a curing agent which are initially liquid, but if mixed undergo a cross-linking reaction, resulting in an elastomeric solid (see figure 47). This cross-linking reaction and the parameters which determine its speed and its quality such as the curing agent to base ratio and the curing time / temperature will be discussed in detail in the following.

4.1.1. Cross-linking reaction

The cross-linking reaction of the PDMS (Dowcorn Sylgard 184) is shown in figure 47.

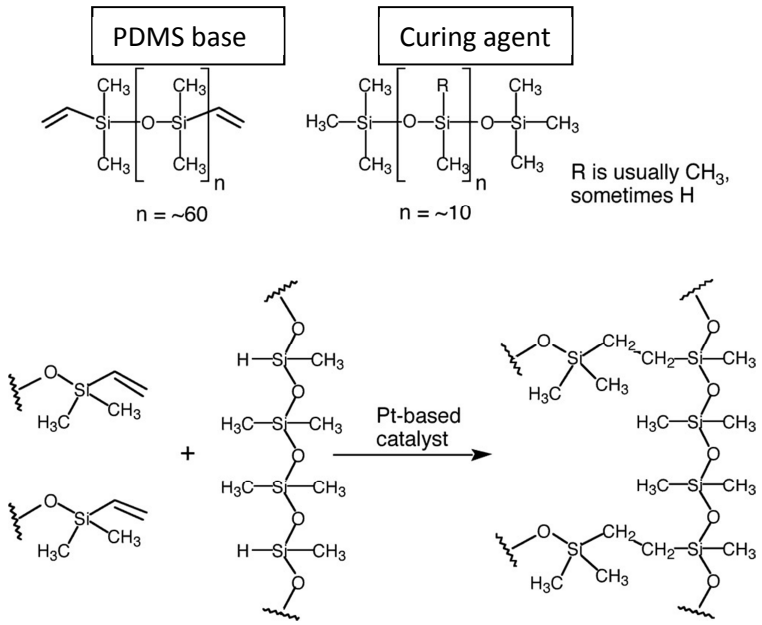

Figure 47: Cross-linking reaction of Dowcorn Sylgard 184 (from reference [38]). Initially the Sylgard 184 consist of two liquid components; the curing agent and the base. These undergo a crosslinking reaction upon mixing. The curing agent also contains the Pt- based catalyst.

The PDMS base is vinyl terminated, while the cross-linking agent is methyl terminated and contains silicon hydride units. During curing the PDMS base monomer-vinyl groups crosslink to the curing agent silicon hydride groups forming Si-CH_2-CH_2-Si linkages. [**33**]

The PDMS has the following chemical properties: [**39**]

- The low surface tension of the PDMS pre-polymer is due to the closely packed methyl groups which show a low intermolecular force. The low surface tension is necessary to replicate the master with high resolution because the PDMS pre-polymer has to penetrate even into its smallest gaps.
- The strength of the siloxane bond Si-O-Si is very strong (dissociation energy 445 kJ/mol). The strength of the Si-C bonds is lower (dissociation energy 306 kJ/mol).
- The siloxane backbone is very flexible.

There will always be uncross-linked low weight molecules (LWM) in the PDMS. [**37**] These LWM can diffuse through the PDMS. Thus, in the case of microfluidic applications these LWM can contaminate the fluids and furthermore influence the samples (e.g. biological samples). [**40**] Anyhow, if necessary,

low weight molecules can be extracted by suitable solvents. [**37**] Further, the concentration of LWM can be minimized if the right curing time and temperature as well as the right curing agent to base ratio is chosen.

PDMS pre-polymer is also believed to be cross-linked to OH groups on SiO_2, oxygen plasma activated PDMS, glass and polyvinyl alcohol (PVA) substrates, since PDMS pre-polymer adheres to the substrates mentioned upon curing. The adhesion is irreversible and the PDMS mold brakes if it is peeled off, leaving residual PDMS left on the substrate (see figure 48 on the right). A detailed discussion of surface OH groups on SiO_2 substrates is given in the appendix in chapter III) on page 111. The chemical reactions which are thought to be possible on a SiO_2 are shown in figure 48. The reactions happening on the other substrates, glass, oxygen plasma activated PDMS and PVA are believed to be similar.

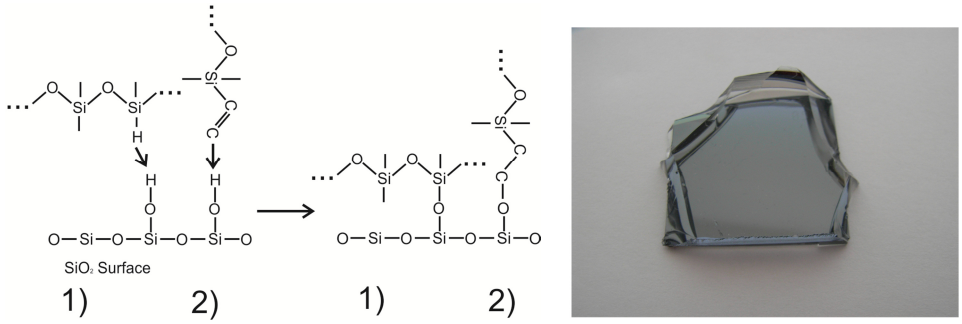

Figure 48: Left; possible cross-linking reactions between a SiO_2 surface and PDMS pre-polymer: 1) the hydroxyl group of the curing agent cross links with the hydroxyl group of the SiO_2 substrate. 2) The vinyl group of the base is cross-linked to the hydroxyl group of the SiO_2 substrate. Right; PDMS on a SiO_2 wafer after unsuccessful peel off. The PDMS polymer can't be peeled off the SiO_2 if it is not coated with HMDS.

If the substrate is coated with HMDS (Hexamethyldisilazane) all surface OH groups are saturated (see figure 49) and no adhesion between the PDMS pre-polymer and the SiO_2 substrate can be observed upon curing. It is believed that the PDMs pre-polymer cannot cross link to the already occupied surface OH groups nor to the $Si(CH_3)_3$ groups of HMDS. It is interesting to mark that HMDS coatings render the substrates hydrophobic and are usually used to improve the adhesion between hydrophobic polymer resists and SiO_2. However, in this case, HMDS serves as an anti-adhesion layer.

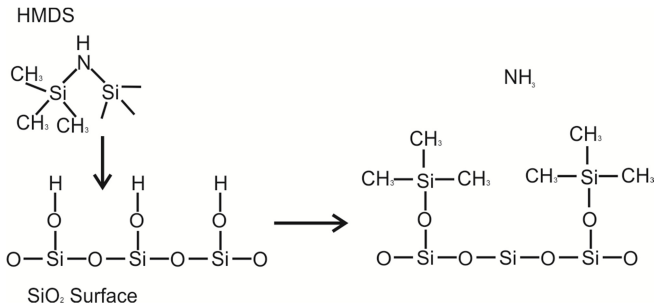

Figure 49: Chemical reactions of HMDS on a SiO_2 surface; The surface OH groups of the SiO_2 are replaced by $Si(CH_3)_3$ groups rendering the surface hydrophobic (as described in reference [41] and cited references therein).

4.1.2. Curing agent : base ratio

The mechanical properties, e.g. hardness, yield strength and young modulus are highest for a certain curing agent to base ratio (A : B) and decrease if the amount of cross-linking agent is increased [**42**] or decreased from this optimum value [**43**]. This optimal ratio depends on the curing time and temperature. [**44**]. Significantly harder PDMS can therefore only be fabricated by using another cross-linking agent or base. [**45**]

The viscosity of the PDMS pre-polymer can be changed by varying the A: B ratio since the viscosity of the agent (0.0011 m^2/s) is lower than that of the base (0.0050 m^2/s). [**35**] Low viscosity is necessary to create spin coated thin PDMS layers which can be used to seal PDMS stamps. [**44**] The drawback of this technique is that the excess curing agent will diffuse into the bulk-PDMS, affecting its mechanical properties (e.g. young modulus). [**46**]

4.1.3. Curing temperature and curing time

Other parameters which are very important for the cross-linking reaction are the curing temperature and the curing time. The curing time necessary to achieve a good cross-linking (minimum LWM concentration) depends on the curing temperature. It is believed, similar to other cross-linking processes, that there are two competing processes during curing. One is the desired cross-linking reaction, the other is the undesired 'back-biting' reaction which creates cyclic polymer chains/oligomers. [**47**]

J. Sun and coworkers [**48**] reported that the yield strength and the young modulus were independent of the curing time at temperatures below 200 °C, as long as the curing times were longer than specified in the technical data sheet. However, temperatures higher than 300 °C led to a decreasing young modulus and yield strength with curing time. [**35**] H. Hillborg and U. W. Gwede [**39**] as well as G. Camino et al. [**47**] showed that curing temperatures above 270 °C lead to a decrease in molar mass. Consequently, it is believed that the back-biting reaction gets dominant at high curing temperatures (>200 °C). [**47**] It is therefore important to use curing temperature below 200°C. The curing time on the other hand is not that critical.

If the curing time is chosen below the values specified in the technical data sheet [**35**], the PDMS is not completely but partially cured. Due to the fact that curing also happens at room temperature the partially cured PDMS stamp will eventually get fully cured in the end.

If mechanical properties, like the young modulus and the yield strength are critical, it's better to cure for a longer time than specified in the technical datasheet. The mechanical properties can only get better as long as the curing temperature is not above 200°C.

4.2. Oxygen plasma activation

The only surface modification discussed here is the plasma activation which was used within this master thesis. Other common surface modifications have been summarized by H. Makamba et al. [**34**].

Plasma activation is a widely used method to render PDMS hydrophilic and thus render it suitable for electrophoretic systems. [**1**] Furthermore, plasma activation allows irreversible bonding to SiO_2, glass, Si, quartz, silicon nitride, polyethylene, polystyrene, glassy carbon [**1**] and PSG, PECVD, silicon nitride. [**49**] The major drawback of plasma activation is that the hydrophobicity of the PDMS is recovered after a certain time which is especially problematic for microfluidic systems (the filling of hydrophobic microfluidic channels by water based fluids requires high pressures compensating the negative capillary pressures).

In the following sub chapters the molecular processes upon oxygen plasma activation are discussed first. Then the mechanisms responsible for the bonding between plasma activated SiO_2 / glass and PDMS are elucidated. The problematic hydrophobic recovery and its investigation by contact angle measurements is discussed in the end.

4.2.1. Processes during plasma activation

There are several molecular processes occurring at the surface during plasma activation. The plasma induced surface effects are still under discussion and not fully investigated yet. Currently, the following relevant processes are proposed in literature (see figure 50):

- The undesired formation of a SiO_x like layer with higher oxygen content than the bulk PDMS. This oxidized layer gets thinner, denser (decrease in specific volume) and less flexible with increasing plasma dose and energy, indicating a conversion from the organic like silicon structure to an inorganic SiO_x layer. [**50**], [**39**] The smaller the specific volume of this surface layer gets, the higher is the stress induced by the bulk and consequently the higher the possibility of cracking spontaneously. [**50**]
- The undesired degradation of the silicon network structure by formation of low weight molecules (LWM) with increasing plasma dose and energy. [**50**], [**51**], [**39**]
- The desired formation of silanol groups (Si-OH) on the SiO_2 surface. The oxygen plasma enriches the PDMS surface with silanol groups (Si-OH) by oxidation of the methyl groups. [**52**], [**50**], [**53**], [**39**], [**53**] H- Hillborg et al. [**39**] also propose additional carbonyl groups formation.

The plasma induced surface OH groups render the PDMS hydrophilic and they are responsible for irreversible bonding to plasma activated SiO_2 / glass. Thus, the goal of plasma activation is to create polar OH groups on the surface and not to degrade the siloxane backbone nor to create an inorganic SiO_x surface layer. The kinetic energy of the oxygen ions is increased with increasing power coupled into the plasma and with decreasing plasma pressure [**54**]. The binding energy of the Si-OH groups is lower compared to the Si-CH_3 groups. In the ideal case the plasma parameters pressure and power are adjusted in a way that the kinetic energy of the oxygen ions in the plasma is high enough to attack the CH_3 bonding while it is too low for the siloxane backbone**.** This way the OH group formation is favored while the silicon network is not degraded.

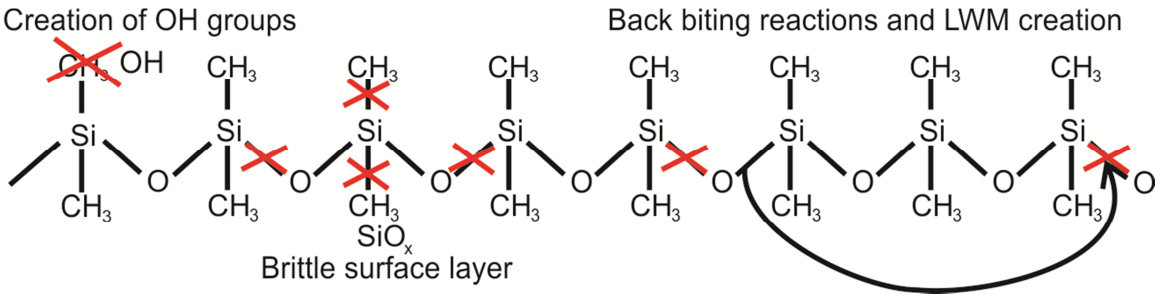

Figure 50: Schematic illustration of the principle mechanisms during oxygen plasma activation.

4.2.2. Oxygen plasma activated bonding

Before starting the discussion it should be mentioned that surface OH groups of SiO_2 substrates are discussed in the appendix in chapter III), on page 111.

The bonding between plasma activated PDMS molds and activated glass / SiO_2 is most likely due to silanol condensations. The Si-OH groups of the SiO_2 / glass form covalent bonds (Si-O-Si) with the Si-OH groups of the activated PDMS stamp by silanol condensation (see figure 51). [**1**], [**53**], [**54**] These covalent bonds are believed to be stronger than the Si-CH_2-CH_2-Si bonds of the cross-linker. Thus, if the PDMS stamp is peeled off the substrate, it rather brakes in the bulk leaving traces of PDMS on it. [**53**] Furthermore, plasma activated PDMS molds can also be sealed to plasma activated PDMS, silicon, quartz, silicon nitride, polyethylene, polystyrene and glassy carbon substrates. In the case of inorganic materials the plasma probably removes the contaminants liberating the surface OH groups, and in the case of the organic materials surface OH or COOH groups are created. [**1**] Similar to a SiO_2 substrate, activated PDMS molds are believed to condense with these groups forming Si-O-R bonds. [**1**]

The adhesion strength between the PDMS mold and the substrate is determined by the OH group density on the surface and by the surface roughness. An overexposure to oxygen plasma leads to a brittle and rough (nm scale) SiO_x surface layer decreasing the contact area PDMS -substrate and therefore also the adhesion strength significantly. [**54**] As a consequence, the plasma activation parameters pressure, power and time have to be adjusted properly to achieve a good adhesion between the PDMS and the SiO_2 / glass substrates, i.e. the goal is to achieve a high OH group density and at the same time to avoid a rough SiO_x surface layer.

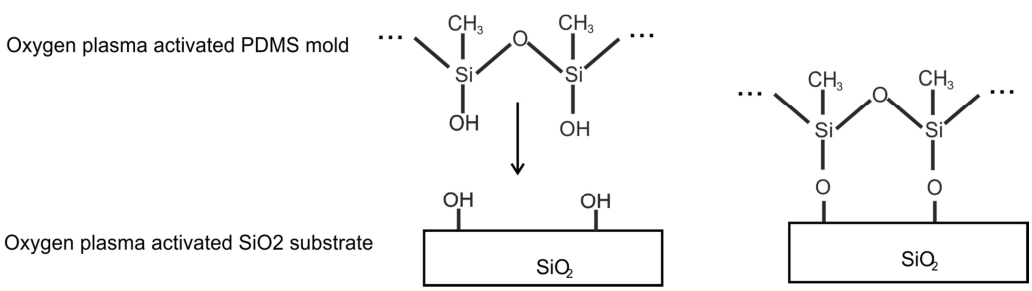

Figure 51: Oxygen plasma activated SiO_2 substrate and PDMS mold; the surface OH groups of the PDMS mold react with the surface OH groups of the SiO_2 via a silanol condensation forming a strong covalent Si-O-Si bond.

Regarding the evaluation of the plasma activated sample, it is important to know that the contact angle of DI (de-ionized) water is correlated with OH group density and therefore also correlated with the bonding strength between PDMS and SiO_2 / glass as long as the sample is not overexposed by oxygen plasma. [**55**]

4.2.3. Hydrophobic recovery

The plasma induced surface OH groups render the activated PDMS hydrophilic. But the plasma activated hydrophilic PDMS recovers its natural hydrophobicity after a while. The mechanisms of this hydrophobic recovery proposed in literature are: [**39**], [**51**]

- Low weight molecule (LWM) diffusion; these low weight molecules diffuse onto the surface covering the polar OH groups.
- Condensation of the silanol groups on the surface.
- Adsorption of organic molecules on the surface.
- Reorientation of polar groups into the bulk.

All of these processes are likely to happen but the dominant mechanism is generally believed to be the migration of LWM to the surface covering the polar OH groups. [**39**], [**50**], [**51**]

Besides the formation of polar OH groups the plasma activation creates an undesired brittle SiO_x surface layer and LWM. The specific volume of the brittle SiO_x surface layer is decreased upon longer exposure with higher energy [**50**], i.e. the surface layer gets denser. The denser the SiO_x surface layer the better it shields LWM from reaching the surface but also the higher the stress induced by the bulk PDMS and therefore the higher the possibility of spontaneous micro cracks. These micro cracks, in turn, enhance the diffusion of LWM and therefore the hydrophobic recovery. Even the onset of mechanical stress can change the rate of the hydrophobic recovery drastically. [**39**] Moreover it should not be disregarded that these LWM are always present in the material and that plasma activation creates additional low weight molecules. The formation of these LWM is favored by long exposure times with high energy. [**51**] The higher the concentration of low weight molecules the faster the hydrophobic recovery. [**50**], [**51**]

The hydrophobic recovery can be hindered by storing the activated molds in polar DI water (deionized water). The polar water shields the un-polar LWM from the surface. Consequently, the polar OH groups are conserved and the wettability is retained. This effect was examined by M. Morra and coworkers [**56**].

4.2.4. Contact angle measurements

In order to quantitatively investigate the hydrophobic recovery of PDMS, contact angles of DI water on PDMS molds were measured as a function of time after their plasma activation. Additionally, the influence of mechanical stress on the hydrophobic recovery was examined. The measurement method and sample fabrication is described in the appendix, chapter VI), on page 113.

The contact angle of DI water measures the hydrophilic OH group density as long as the PDMS has not been overexposed. [**39**] If the sample is overexposed to oxygen plasma the contact angle is decreased but this is due to a rougher surface and not to a decrease in the OH group density.

Please note: The contact angle of DI water of the untreated substrates PDMS, SiO_2 and glass were 110°, 50° and 40°, respectively.

Due to the sensitivity of the activated surface, there is a difference between measuring contact angles on undisturbed samples and on those that have already experienced mechanical stress. An example for mechanical stress could be bending or blow drying the sample with an air gun after a precedent contact angle measurement. Thus, the contact angles used to study the hydrophobic recovery were measured on undisturbed samples which haven't been touched / bended after plasma activation. The results are shown in figure 52 (black line). It can be seen that the undisturbed samples actually recover very slowly.

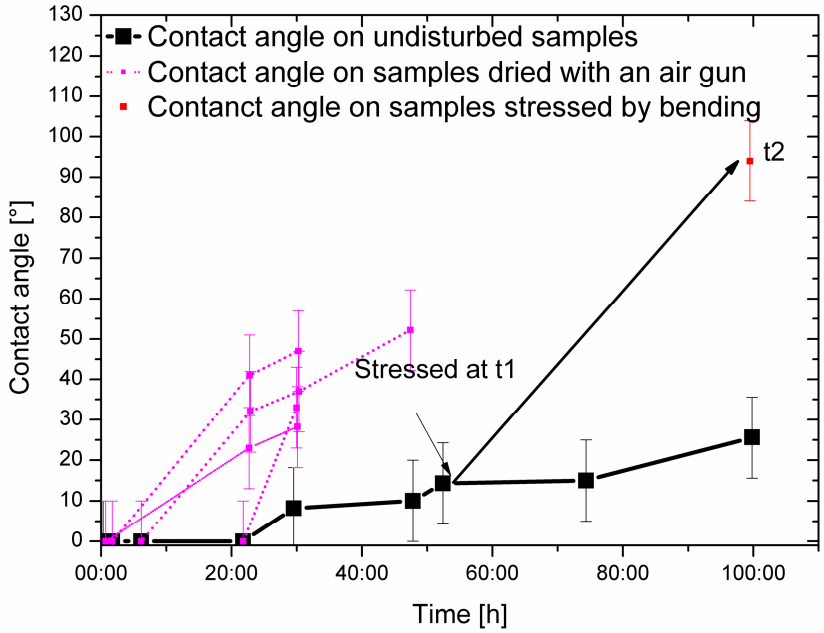

Figure 52: Contact angles of DI water as a function of time after oxygen plasma activation (activated at 50 W for 1 min at a pressure of 0.6 mbar): The black squares are the contact angles measured on undisturbed PDMS samples which had not been touched after plasma activation. The pink squares represent contact angles measured on samples which had already been dried with an air gun after precedent measurements (the samples were measured multiple times). The red points indicate the contact angle of a sample at time t2 which has been bended at time t1.

In order to study the influence of mechanical stress on hydrophobic recovery, contact angles as a function of time on disturbed samples were examined. First, disturbed samples which were stressed by blow drying after precedent measurements were investigated. The results are shown in figure 52 (pink squares). As soon as the sample gets disturbed by blow drying after the first measurement, one can observe a fast increase of the contact angle and thus hydrophobic recovery. This could either be ascribed to micro cracks enhancing the low weight molecule diffusion or to the air gun which contaminates the surface with organic molecules. Therefore, an undisturbed sample has been bended at a time t1 and its contact angle has been measured at a time t2. The result is shown in figure 52 and figure 53. This time the sample can't be contaminated by the air gun but there is still a fast increase of the contact angle compared to an undisturbed sample. This indicates that the hydrophobic recovery is due to low weight molecule diffusion and micro cracks. The same measurements were also carried out on samples which were activated at 100 W for 0.5 min yielding similar results.

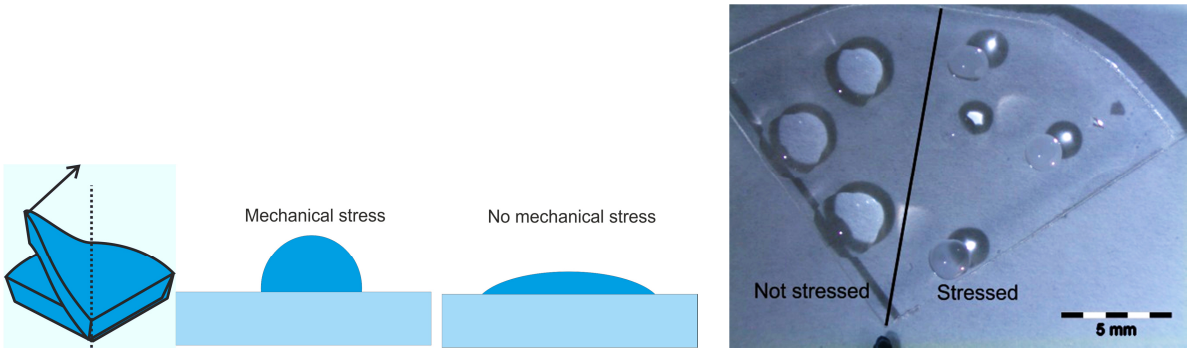

Figure 53: Left; scheme of a water droplet on a half undisturbed and half disturbed sample: The undisturbed sample has been stressed on one side by bending it. The other side stayed untouched. Water droplets with the same volume were brought onto the sample. Right; Picture of the water droplets on the PDMS substrate made with an optical microscope. The contact angle of the droplets is higher on the stressed side than on the untouched side. As a consequence droplets on the stressed side seem to be smaller than on the undisturbed side, even if they have the same volume.

Figure 54 shows the contact angle of two PDMS samples, one activated for 0.5 minutes and the other for 4 min at 50 W and 0.6 mbar oxygen pressure. The samples were dried with an air gun after each measurement. It has already been shown that the contact angle is influenced by the air gun. However, the first data point in figure 54, where the sample is still undisturbed, shows that the sample activated for 4 min recovers faster than the sample activated for 0.5 minutes. This could be due to the denser surface layer at longer exposure times which is more likely to crack

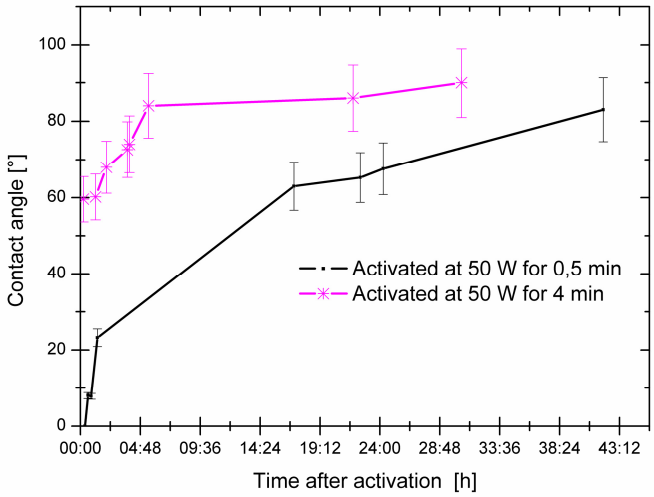

Figure 54: Contact angle on PDMS samples activated at 50 W and 0.6 mBar for 0.5 minutes and 4 minutes as a function of time after oxygen plasma activation. The contact angles were all measured on the same samples. The samples were dried gently with an air gun after each measurement.

4.3. PDMS as a material for replica molding

If PDMS is used as a material for replica molding, there are some limitations to the topography of the master.

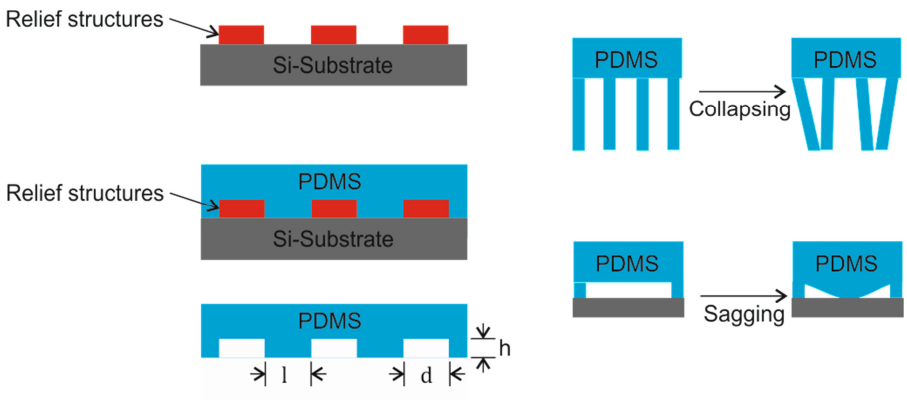

Figure 55: Left; Scheme of the replica molding procedure with PDMS. The height of the replicated structures is marked with h. The width of the replicated, protruding structures on the PDMS is marked with l and the distance between them with d. Right; collapsing and sagging due to the elasticity of the PDMS.

The first limiting factor is that the aspect ratio (h/l) of the replicated, protruding structures on the PDMS mold should not be too high, in order to avoid collapsing (shown in figure 55). These failures are either caused by their own weight or by slight external stresses. [**2**], [**36**], [**57**] The value of the maximum aspect ratio depends on the geometry of the structure and as well as on the distance between neighboring structures. In literature it was found that for straight lines the aspect ratio h/l should be smaller than 2 [**57**] or around 1 [**36**].

The second limitation is that structures protruding out of the PDMS mold should not be spaced too far apart in order to avoid sagging (shown in figure 55). Thus, the aspect ratio (h/d) should be higher than 0.05. [**2**], [**36**] Sagging is especially a problem concerning microfluidic structures such as reservoirs for optical observation or mixing chambers which are usually very wide (they have low aspect ratios h/d). It is possible to increase the aspect ratio of these structures by putting additional posts into their non-contact region. These posts must have an aspect ratio (h/l) lower than 2 themselves.

Another limitation is due to the adhesion between the resist and the PDMS. As the width of the protruding structures on the PDMS / on the resist (l / d) decreases, keeping the height (h) constant, the volume to surface ratio gets smaller. At a certain point, the resist is peeled off with the PDMS / or the PDMS bulk breaks leaving residual PDMS left on the master. Masters using a 300 nm thick (h) PMMA resist on a SiO_2 substrate and gratings with 100 nm features (d) and 100 nm spacing (l) yields reliable molds. [**36**] Further, if the spacing between the protruding resist features is below 200 nm, the viscosity of the PDMS hinders an exact replication of the master, i.e. the PDMS pre-polymer does not penetrate into small crevasses. [**58**] Another issue at these length scales is the material flow, which gets important at features below 100 nm. [**58**] Anyhow, these dimensions are well below the dimensions necessary in this work.

However, working at the limits of the aspect ratios is not recommended. PDMS structures with an aspect ratios d/h higher or close to 0.05 or an aspect ratio h/l close or below 2 tend to collapse or sag at the slightest external distortions. This can be avoided by using a maximal aspect ratio of h/d of 0.08 and a maximal aspect ratio of h/l of 1.5. Therefore, the channels should be smaller than 12 time their height. If posts are used to avoid sagging, their height has to be smaller than one and a half times their width.

5. Master fabrication

The masters were structured by electron beam lithography and by inkjet printing. The electron beam lithography system itself has already been characterized and won't be discussed here. This chapter deals with results of the structures fabricated and the issues which have to be considered.

First the masters structured by EBL are discussed. Secondly the fabrication of the inkjet printed masters is presented. The combination of inkjet printing and EBL is discussed subsequently. After the masters are fabricated, they have to be coated with an anti-adhesion layer. This process is explained in the end.

5.1. Electron beam lithography

The challenge creating microfluidic structures is that their channels extend over a few millimeters and as a consequence their typical writing times can range from 4 h up to a few days. A single failure in a channel can render the whole chip useless. The system is therefore very sensitive to temperature drifts, i.e. temperature drifts have to be compensated. Another challenge arising when dealing with microfluidic structures, fabricated in this work, is that they contain channels having lateral widths ranging from sub µm to tenths of µm. As a consequence proximity correction is absolutely necessary.

The structures fabricated in this work are a mixer, a reservoir and a possible droplet generator which will be discussed in the mentioned order.

5.1.1. Reservoir structured by EBL

Reservoirs can be used to store and mix fluids. The height of the reservoir is determined by the resist height (850 nm). The aspect ratio of the PDMS limits the size of the reservoir to ~10 µm which is not satisfying (see chapter 4, sub chapter 4.3, on page 57 for details). For that reason pillars supporting the PDMS were introduced. These pillars correspond to holes in the reservoir on the master structure (see figure 56). The master to create such a reservoir should meet the following requirements:

- The width of the holes should be bigger than half the pillar height (420 nm).
- The distance between the holes should be smaller than 12 times their height (~ 10 µm).
- The holes have to be free of resist. If this is not the case the PDMS mold collapses.

The problem structuring such a reservoir is that the edges of the holes have to be well defined and at the same time it is important that the holes are free of resist. This is why a proximity correction is required. This way it is ensured that the overall dose to achieve the maximal resist height as well as defined edges is minimized.

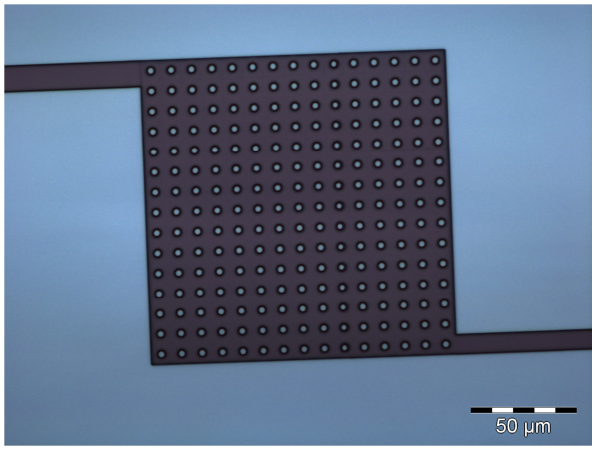

Figure 56: Image made with the optical microscope of a reservoir structured by EBL. The resist appears dark and the substrate bright. Holes in the reservoir serve as pillars to avoid a collapsing of the reservoir.

Furthermore, such a reservoir takes a long time to expose (the area to be exposed is large) and the structure is therefore very sensitive to beam drifts. If only a single hole is not completely free of resist, the structure can't be used. An automatic write field alignment to compensate the beam drifts is therefore necessary. This alignment has been carried out each 15 min in between the write fields (50 µm size).

5.1.2. Mixer structured by EBL

The goal was to create a staggered herring bone structure as explained in chapter 2.1 on page 6. The grooves necessary to obtain the herring bone structure were created by dose variations. The height differences of the channels can be seen by a color change. Such a mixer is shown in figure 57.

Automatic proximity correction was only carried out around the junctions of the channels. This can be done because all channels had a width of 10 µm requiring the same optimized dose.

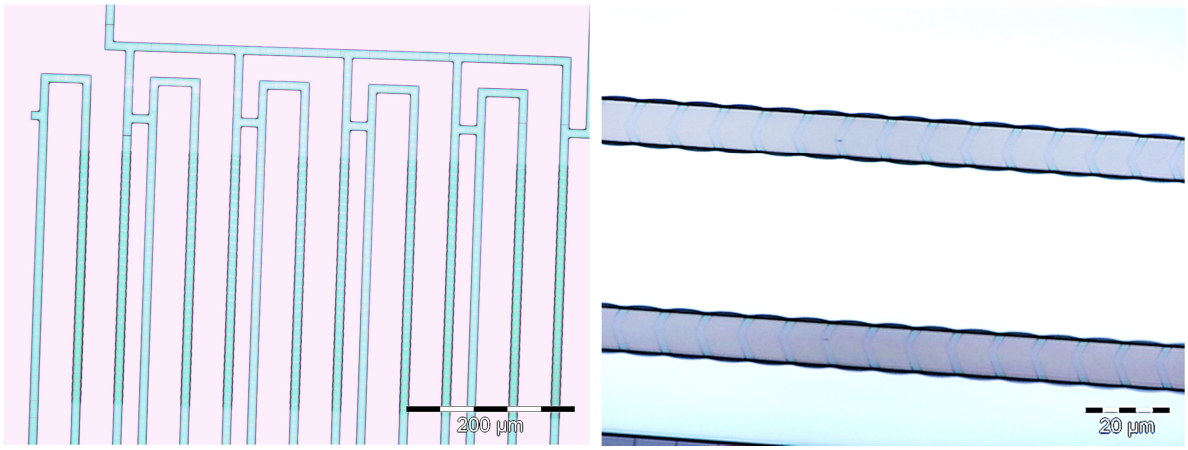

Figure 57: Left; a possible gradient mixer. Right; close up of the structure from the left. The height of the channel was varied by dose variations to create a so called staggered herring bone structure.

5.1.3. Droplet generator structured by EBL

The goal was to structure a droplet generator. The structure is shown in figure 58. This structure has never been used as an actual microfluidic system. Therefore only fabrication aspects are discussed.

The channel widths are ranging from 10 µm to 500 nm. Proximity correction is therefore required. The proximity correction is especially important for the triangles, i.e. the transition between a channel having a width of 10 µm and one with a width of 500 nm.

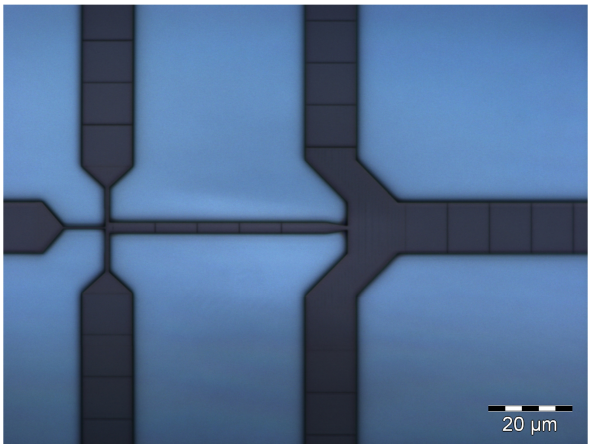

Figure 58: Image made with the optical microscope of a possible bubble generator structured by EBL. Channel widths ranging from 500 nm to 10 µm without a change in color. The height is therefore believed to be the same for all channels.

All channels have the same color independent of their width. It is therefore believed that all of them have the same height and as a consequence that proximity correction worked.

Large structures (> 50 µm) can't be proximity corrected at once. They have to be separated manually into smaller parts and then reassembled. It is for example practical to simulate a rectangle with a length of 10 µm and then duplicate this rectangle 10 times in order to obtain a rectangle / channel with a length of 100 µm. One problem arising by this separation is that the structures must be a multiple of the step size of the exposure rater. This has not been the case and as a consequence one can see the overlaps of the 10 µm rectangles in figure 58.

5.2. Inkjet printed masters

Inkjet printing is fast, cheap and flexible and it can be used to structure masters for the fabrication of microfluidic channels. Furthermore Inkjet printing can be used to create electrodes on the substrate which are rather thick (1 µm - 20 µm+) compared to evaporated or sputtered electrodes (< 1 µm).

The inkjet printed masters were all kindly fabricated by Dr. Karl Popovic. The samples were all printed with an Ag ink at a resolution of 800 dpi. One layer had a height of about 1 µm. In order to increase the height, multiple layers were printed. The design shown in figure 59 on the left has been printed with 5, 10 and 20 layers having an approximate height of 4.5 µm, 9 µm and 18 µm. The relation between the pixel width of a line and the actual width of this line is shown in figure 60 on

the right. The relation between the line width and the number of layers is shown in figure 60 on the left.

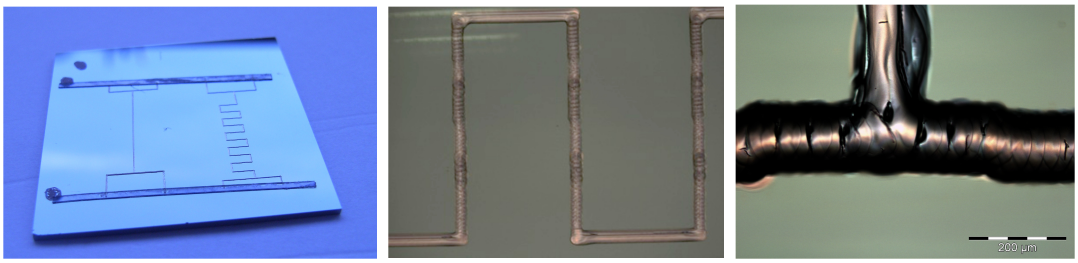

Figure 59: Left; master structured by inkjet printing with Ag-paint (20 layers). Center; master structured by inkjet printing with Ag-paint (20 layers). Right; close up of the master shown on the left. The channels are not smooth and their width varies on a long range (mm) as well as on a short range (µm).

The minimal width of the channels is around 150 µm. Printing a chip with ten layers whose channels have a height of 9 µm would be critical due to the maximum aspect ratio of the PDMS. Thus, the master were printed with 20 layers having a height of 18 µm. Hence, the width of the channels can be varied between 2 pixels (150 µm) and 4 pixels (180 µm)

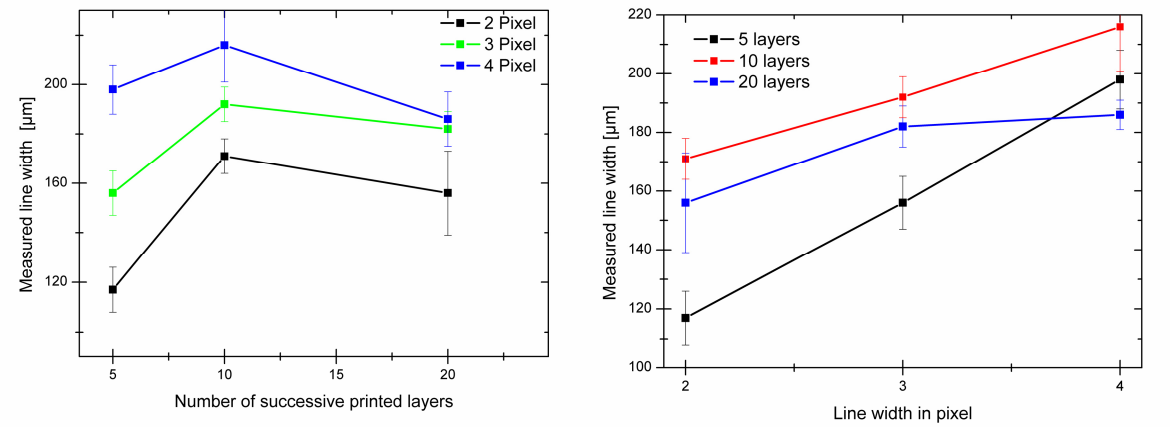

Figure 60: Investigation of the width of lines printed with Ag ink on SiO_2 at a resolution of 800 dpi. Left; measured line width as a function of successive printed layers. Lines with a designed width of 2,3 and 4 pixels were investigated. Right; measured line width as a function of designed width in pixel for different successive printed layers.

As a conclusion one can say that the lines were not smooth and the width of the channel varies. Even if the laminar flow is not influenced by the rough channel walls, the results will not be reproducible from master to master and further optimization is absolutely necessary.

5.3. Combination of inkjet printing and electron beam lithography

The goal of combining inkjet printing with EBL is to structure the heart of the chip by EBL and to print the access channels by inkjet printing. This way, the important functional parts are written by the slow EBL with a high resolution and the large access channels are printed by the fast inkjet printer with a low resolution. This technique is not only interesting for microfluidic systems, but it may turn out to be a practical tool for other applications.

The masters have to be structured by EBL first because else, spin coating the electron beam resist would not be possible without obtaining resist height variation around the thick inkjet printed channels (18 µm). Moreover, changing the surface by HMDS (Hexadimethylsilanzane) coating as an adhesion promoter for the EBL resist is not possible since it would change the contact angle of the Ag ink on the substrate. In fact, the major issue is the alignment of the inkjet printer relative to the master already structured by EBL. For that reason three alignment marks were structured by EBL defining the coordinate system of the sample. The coordinate system of the printer is then aligned with the help of these three marks.

One important issue to consider is that the design printed by the inkjet printer should be drawn prior to the design of the EBL because changing the line width by a pixel would change the design of the EBL. For example, at a line width of 2 pixels, the channel structured by EBL having lateral dimensions of 10 µm have to hit the inkjet printed channel in between the pixels. Whereas, at a line width of 3 pixels, the channel structured by EBL would have to hit the channel at the center of the central pixel. Thus, it is really important to design the inkjet part prior to the EBL part. Examples of masters structured by inkjet printing and EBL are shown in figure 61.

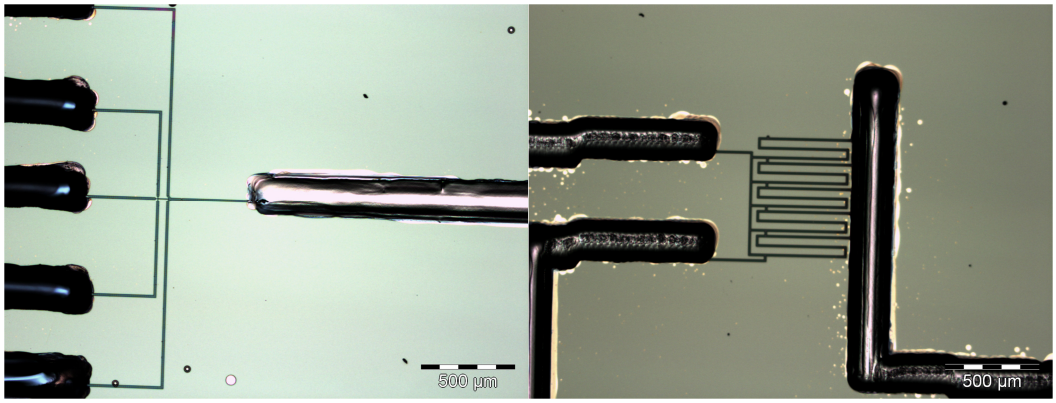

Figure 61: Inkjet printed access channels were properly aligned to the structure designed by EBL. Left; a possible droplet generation system. Right; a possible gradient mixing structure.

The alignment obviously worked. The samples were subsequently coated with HMDS. The problem occurred during the peel off. The PDMS mold tore off Ag-chunks destroying the master and the mold. The problem is that the Inkjet printed master are usually structured at temperatures higher than 100 °C. These temperatures would destroy the resist that's why the samples were printed at 80 °C. This is obviously not enough for the Ag ink to adhere to the SiO_2 surface. Thus, Ag ink is not

suitable for this application. Consequently, if this technique should further be pursued, it has to be done with another material than Ag-ink. A possibility would for example be photo resist.

.

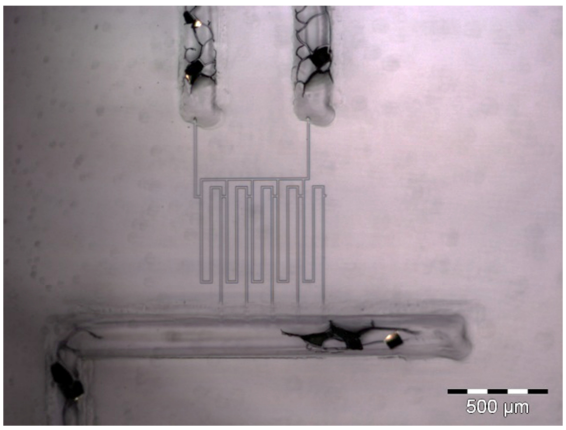

Figure 62: PDMS mold peeled off an inkjet and EBL structured master. Ag chunks were torn of the substrate destroying the master as well as the mold.

5.4. Anti-adhesion layer HMDS

All masters must be coated with an anti-adhesion layer in order to reduce the adhesion between the PDMS and SiO_2 / glass substrates upon curing as already described in chapter 4.1.1, on page 49. This is usually done by coating the substrate with a flour carbon layer polymerized with CF_3 plasma [**59**] or by silanization with tridecafluoro1,1,2,2-tetrahydrooctyl-1-trichlorosilane [**1**]. Both approaches are not possible because the equipment has not been in place. An alternative is HMDS (Hexadimethylsilanzane) as explained in chapter 4.1.1, on page 49. It is believed that HMDS basically does the same as the tridecafluoro1,1,2,2-tetrahydrooctyl-1-trichlorosilane, it replaces the surface OH groups by chemically inert groups. [**41**]

The Novolac resist used, does not withstand temperatures higher than 80°C. This is why the HMDS coating procedure was carried out at 50 °C by the following procedure: Evaporate HMDS for 10 min in a vacuum on a hot plate and subsequently flush for 10 min with NH_3 (10 cycles).

The contact angles on the PDMS mold and the SiO_2 substrate were measured before and after the peel off. The contact angles didn't change. For that reason, it is believed that the HMDS does not influence the mold. The masters can also be used multiple times without recoating them with HMDS and therefore it is further believed that the HMDS stays on the master and is not peeled off by the mold.

Further, if a plasma activated PDMS mold is coated with HMDS one can reuse this mold as a master. The HMDS serves as an anti-adhesion layer on a plasma activated PMDS mold. This is very practical because one can invert a structure, i.e. one can turn a negative master into a positive one. It is believed that HMDS behaves the same way on a plasma activated PDMS surface as on a SiO_2 surface (see chapter 4, sub chapter 4.1.1 for details). It is additionally believed that the reactive HMDS diffuses into the PDMS deactivating the active sites like uncross-linked oligomers.

5.5. Conclusion – master fabrication

The masters were structured by electron beam lithography, inkjet printing and by a combination of inkjet printing and electron beam lithography.

The major challenge of structuring microfluidic systems by electron beam lithography is that the lateral dimensions of microfluidic structures range from a few hundred nm up to tenths of µm making a proximity correction and resist profile simulations inevitable. Another issue is that these systems extend over a few mm requiring long exposure times and thus automatic drift compensations. Nevertheless, it has been shown that complex structures can be designed and exposed in two days providing a great amount of flexibility. As benchmarks, a reservoir, a possible droplet generator and a mixer have been designed and fabricated successfully. The reservoir required long writing times and thus, validated automatic drift compensation. It was further possible to keep the designed integrity of the droplet generator, having lateral dimensions ranging from 500 nm to 10 µm, due to a correct proximity correction. It has also been shown that the channel heights of the mixer can be varied in a controlled way by exposure dose variations and resist profile simulations.

Inkjet printing has the advantages of being fast and flexible. Furthermore, the height of the channels can be varied by printing multiple layers. The masters were printed with nanoparticle Ag ink on a SiO_2 substrate. The minimal width of a channel was 160 µm at a thickness of 18 µm (20 layers). Printing multiple layers lead to long ranging variations (mm) and short ranging variations (µm) of the channels widths at the order of 30 µm. Thus, the accuracy and the resolution of inkjet printing is not suitable for complex microfluidic systems. For that reason, the microfluidic system was separated into a functional part and into the periphery (access channels). Not as the functional part, the access channels don't require a high resolution. The idea was to reduce the fabrication time by combining Inkjet printing and EBL. The functional part was structured with a high resolution by the slower EBL whereas the periphery was structured with a low resolution by the fast inkjet printer. The combination of these techniques requires an alignment between the inkjet printer and the EBL which has been successfully done. The current problem is that the resist used for EBL can't withstand temperatures higher than 80 °C which are necessary for the Ag ink to adhere to the SiO_2 substrate. As a consequence, the inkjet printed channels get peeled off the master during the mold fabrication process. Therefore, other inks which have the same processing temperatures as the EBL resist have to be used in the future.

The PDMS pre-polymer adheres irreversible to the SiO_2 / glass substrates upon curing if they are not coated by HMDS.HMDS coatings do not change the contact angle on the mold nor on the substrate after peel off. Further, it is not necessary to re-coat the master after the first peel off. For that reason, it is believed that the HMDS coating is not peeled off the substrate by the mold and that the mold is not influenced by the HMDS coating.

6. Mold fabrication

In general, creating molds for simple and small microfluidic chips or material investigations is a rather simple task. In contrast, microfluidic systems consisting of channels in sub µm meter range on the other hand require a more complex fabrication procedure. An overview of three different developed and implemented fabrication procedures according to their application is given in figure 63. The first one, which serves to fabricate simple, thick PDMS molds, was only relevant for prior testing and PDMS material investigations. The second one was used to create flat molds which can be bonded reliably to substrates (see chapter 7). For that reason, these molds are suited for simple microfluidic chips. The last one is based on the second one and is used for more complex microfluidic systems containing sub µm channels. The main advantage of the latter is that an optical observation of the channels at a reasonable magnification is possible.

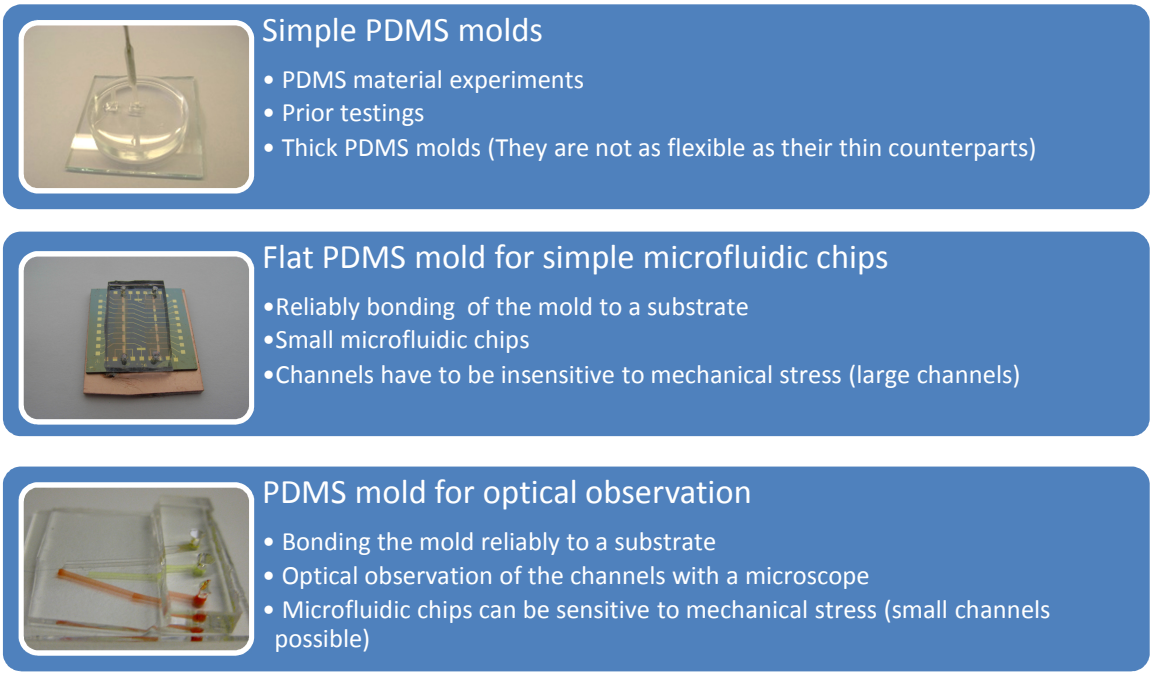

Figure 63: Developed and implemented fabrication processes and their application.

The fabrication process can be separated into a preparation part, the curing itself, the release and the access hole drilling part. Accordingly, several fabrication steps before and after curing the mold will be presented first. Further, the fabrication of flat PDMS molds and molds for optical observation will be explained in detail.

6.1.1. Preparation and curing

Figure 64 shows an overview of the mold preparation procedure. The first task is to place a transparency onto a glass sheet (figure 64, step 1). This is necessary to avoid any damage of the master. If the master is placed directly onto the glass sheet, the PDMS penetrates into the gap between the master and the glass sheet gluing the master onto the glass. As a consequence, it is almost impossible to peel off the master without damaging it. The advantage of the transparency is that it is flexible and that the transparency can be peeled off the master without any problems. After the transparency is placed on the glass sheet it is covered with double sticking scotch tape (figure 64 step 2). The scotch is necessary for the following reasons:

- The tape has a very viscous polymer on top, filling tiny holes in the frame placed onto it which would lead to a leaking of the PDMS. This problem also occurs, if the scotch tape is placed too far apart or if it overlaps.
- The master placed on-top of the scotch tape, has to be fixed. If this would not be the case the master would start floating around in the PDMS pre-polymer.

Afterwards a frame is placed onto the scotch tape (figure 64, step 3). This frame was usually cut out of plastic sheets but can also be made out of other materials. The frame should meet the following criteria:

- The frame should be slightly larger than the master, i.e. there should be a gap of about 5 mm between the master and the frame. This facilitates the handling afterwards.
- The frame should be elastic to reduce tensions during peel off.
- The frame should have a smooth surface and no overhangs. If this is not the case, air bubbles get entrapped in the PDMS-pre-polymer during curing leading to damaged PDMS molds.
- The frame should not adhere to the PDMS.

The master is subsequently placed onto the scotch tape into the frame and is carefully pushed down at the edges to ensure that it sticks to the scotch tape and that there is no air trapped underneath (figure 64 step 4). If the master does not adhere to the scotch tape it starts floating around in the PDMS pre-polymer during curing. Further, air trapped underneath the master will lead to bubbles in the mold finally destroying it.

After the preliminary work is done, liquid PDMS, which is prepared as described in the in chapter II) 2, on page 110, is carefully poured into the frame (figure 64 steps 5). Any enclosure of air bubbles can be avoided if the PDMS is poured very slowly. Finally the PDMS is placed onto a hot plate and cured according to a process described in the appendix in chapter II), on page 110.

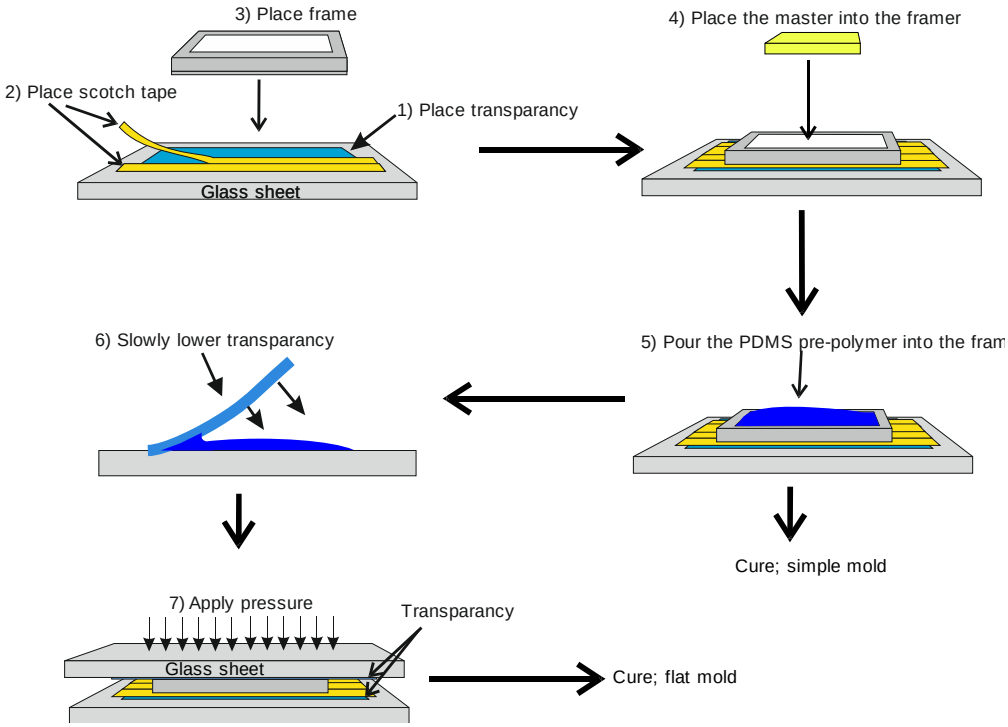

Figure 64: Fabrication of flat and simple PDMS molds. 1)-3) The transparency is placed on the glass substrate and cover with scotch tape. The scotch tapes have to be carefully aligned to avoid any overlaps or gaps. Subsequently the frame is placed onto the scotch tapes. 4) The master is placed in the frame onto the transparency / scotch layer. After that the master is pushed carefully at the edges with tweezers in order to ensure that it sticks. There should be no gaps between the master and the scotch, in order to avoid PDMS penetrating underneath the master. 5) The PDMS pre-polymer is carefully poured into the frame. The PDMS must not contain any air bubbles. If a flat mold is required: 6) Carefully place a transparency onto the PDMS-pre polymer. Air bubbles must not get entrapped underneath the transparency. 7) A pressure is applied from above by glass sheets placed on top of the transparency (their weight is ~1 kg).

6.1.1.1 Creating flat PDMS molds for simple microfluidic chips

The goal of this process is to create flat PDMS molds. The fabrication steps are is basically the same as described by B. H. Jo and al. [**60**] used to create three dimensional microfluidic systems. The proceeding is the same as for simple PDMS chips expect that a second transparency is placed onto the liquid PDMS prior to curing (figure 64, step 6). The transparency is placed onto one side of the frame and subsequently the transparency is lowered very slowly leaving enough time for the air to escape. This way it is ensured that no air bubbles get entrapped underneath the transparency. After that, a pressure is applied from above by placing a weight on top of the transparency (figure 64, step 7). In this work glass sheets were used as weights. This system is subsequently placed onto the hotplate and cured according to a process described in the appendix in chapter II) 2, on page 110.

Please note: If the glass slide is placed onto the chip right away (transparency isn't used) air bubbles get entrapped very easily and it is also very hard to remove the slide after curing.

The height of the mold is determined by the height of the frame. Molds of a height of 500 µm have been created. These thin molds allow an optical observation with a reasonable magnification (> 20 x). But the problem is that the thinner the PDMS mold gets the more sensitive its channels get to mechanical stress on the surface. For example, a tiny touch with the tweezers leads to a collapse of the inkjet structured channels if molds of at thickness of 500 µm are used.

6.1.1.2 Creating PDMS molds for optical observation

Molds for optical microscopy should be as thin as possible in order to allow a reasonable magnification (> 20 x). At the same time these molds should also be insensitive to external stress, especially underneath interconnects (see chapter 8.1.2). This is achieved by creating a mold with two heights. The chip is thick around the interconnections, whereas it is thin around the microfluidic system itself as shown in figure 63.

A tiny amount of liquid PDMS is poured in to the main frame in a way that it just covers the main frame. Then a transparency glued to a second frame with scotch is lowered carefully onto the main frame (figure 65 on the left). After that additional PDMS is poured into the second frame. In the end a second transparency is lowered onto the second frame. As before pressure is applied onto the whole mold by using a spacer and multiple glass sheets (figure 65, on the right).

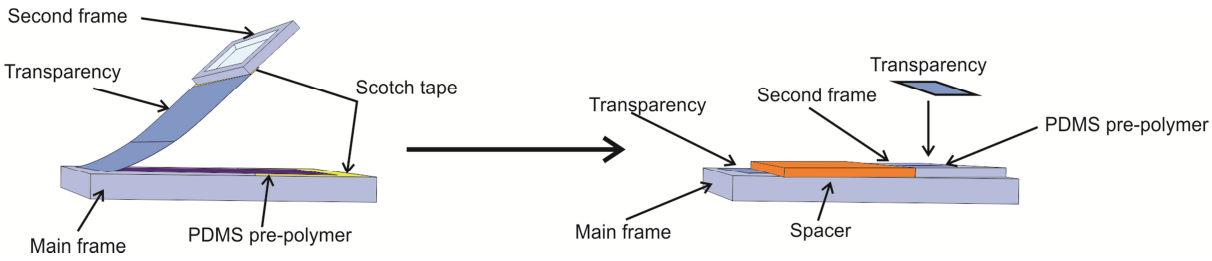

Figure 65: Fabrication of a PDMS mold for optical observation: Left; a transparency fixed to a second frame is put on to the PDMS pre-polymer. The main frame is covered with scotch tape to ensure sealing between the main frame and the second frame. Right; PDMS is carefully poured into the second frame. Subsequently a transparency is placed onto the second frame. After that a spacer is used to apply uniform pressure over the whole structure.

6.1.2. Release the mold and hole drilling

After the PDMS is cured the mold has to be released. First, in order to remove the frame one has to cut around it to separate it from the PDMS. After removing the frame, the PDMS mold is obtained by carefully pealing it off from the master. The frame is slightly larger than the master leading to elevated edges (see figure 66). The PDMS mold can be touched at these elevated edges facilitating the handling of the mold.

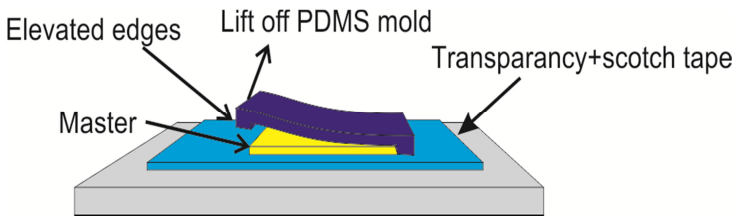

Figure 66: Scheme of the mold release; the PDMS can be touched at the elevated edges which don't belong to the actual mold. This eases the handling.

After the PDMS mold is released access holes are drilled using a biopsy punch which has an outer diameter of 2 mm. Holes with smaller diameters were punched with modified syringes. The drilling instrument has to have a shape as shown in figure 67. The ordinary shape of a syringe doesn't make

a hole but rather a cut which closes itself after retracing the syringe. [**61**] If is important to remove PDMS from the drilling tool before retracing it to avoid a clogging of the channel (see figure 67).

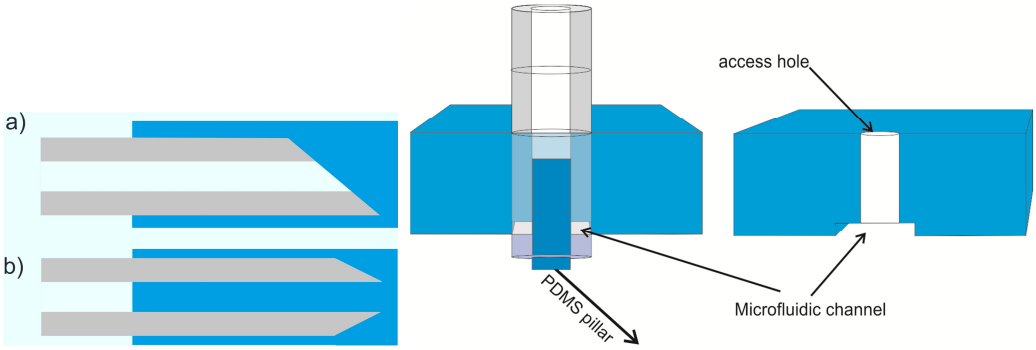

Figure 67: Left; punching the access holes with a biopsy punch. Right; drilling tools: a) Syringe: cuts the PDMS; no PDMS is penetrating into the syringe. The hole closes itself after retracing it. b) Modified syringe / Biopsy-Punch: The PDMS penetrates into the tool and thus an access hole stays after retracing the tool.

After the access holes were drilled, the whole excess PDMS (elevated edges) should be cut away by a scalpel otherwise bonding of the chip to a substrate won't be possible at all

6.2. Conclusion – mold fabrication

Fabrication processes for three types of molds have been implemented including simple molds, flat molds and molds for optical observations. These fabrication processes proved to be reliable and air bubble free. They further required simple and cheap equipment.

Moreover, it was shown that flat molds with a thickness of 500 µm can be fabricated without difficulties. The corresponding fabrication process can also be used to fabricate multilayer microfluidic systems having a high potential for future applications such as valves and pumps.

Furthermore, molds for optical microscopy were fabricated which combine the advantage of insensitivity to external stresses around their interconnects with the ability to investigate their channels with a high magnification. This was realized by fabricating molds which were thick (5 mm) around the interconnects / the periphery and very thin (500 µm) around the interesting functional part of the microfluidic chip.

In addition, it was possible to successfully replicate EBL structured masters with feature sizes of 500 nm with the developed fabrication processes.

7. Bonding of the mold

One key issue of microfluidic systems is the bonding between the mold and the substrate. In order to generate flows in microfluidic channels as well as in order to use fluid control elements like valves and pumps, an external pressure is usually required. Hence, a good adhesion between the chip and substrate is necessary.

There are a several possible bonding techniques. For that reason an overview will be given first. Basically, there are two different kinds of bonding; reversible and irreversible bonding. Reversible bonding is believed to be due to Van der Waals interaction while irreversible bonding is believed to be due to chemical interactions like covalent bonding between PDMS and the substrate for example. [**62**]

Per definition in this master thesis, reversible bonding will be the kind of bonding where the PDMS-mold can be removed from the substrate without damage and without leaving any visible traces, whereas irreversible bonding will be defined as the bonding where the PDMS mold is more likely to crack before it can be peeled off the substrate. Examples of irreversible bonding and reversible bonding are shown in figure 68.

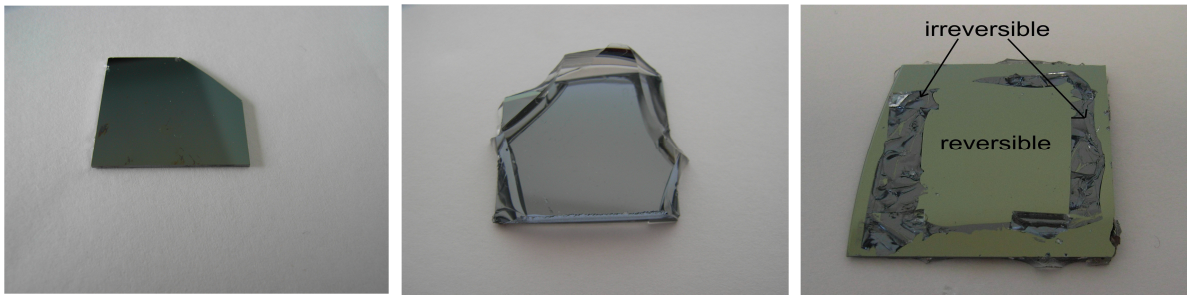

Figure 68: Left; reversible bonding; the PDMS-mold can be peeled off the SiO_2 substrate without leaving any traces. Center; irreversible bonding; the PDMS mold can't be peeled off the SiO_2 substrate. The PDMS rips at the edges before being relieved from the substrate. Right; substrate after peeled off; the PDMS rips before being peeled off the substrate around the edges (irreversible) whereas the center didn't leave any traces (reversible).

There are the following reversible bonding techniques:

- The PDMS mold is placed on a glass / SiO_2 substrate. The completely cured PDMS mold seals weakly reversibly to the glass / SiO_2 substrate. This is believed to be due to van der Waals forces. However, this adhesion is very poor (around 300 mbar). [**62**]
- Pressure assisted reversible sealing: The PDMS mold is placed on to the substrate and a pressure is applied from above via a stiff plate.

Irreversible bonding techniques:

- Plasma activated bonding: The PDMS mold and the substrate are oxygen plasma activated and brought into contact. An irreversible seal is established without the need of pressure or additional temperature. Possible substrates are silicon, quartz, silicon nitride, polyethylene, polystyrene and glassy carbon. [**1**]
- Stamp and stick bonding (SSB) [**63**], [**64**], [**65**]: A thin adhesive layer is spin coated onto a substrate. The layer is transferred via contact printing onto the PDMS-mold which is subsequently placed onto another substrate. This is especially important if electrodes have to be sealed.
- Partial cured PDMS mold is placed onto the substrate and post cured. [**66**]

The techniques pursued here were pressure assisted reversible bonding, plasma activated bonding and the stick and stamp bonding technique. The other bonding techniques won't be discussed any further.

7.1. Pressure assisted bonding

Pressure assisted reversible bonding is done by placing the PDMS mold onto the substrate and applying a pressure from above (see figure 69). This technique is quite simple and the maximal pressure which can be applied to the microfluidic structures basically depends on the pressure applied from above. The advantage is that this technique does not modify the substrate. This could for example be interesting for the integration of sensible organic field effect based sensor into microfluidic systems.

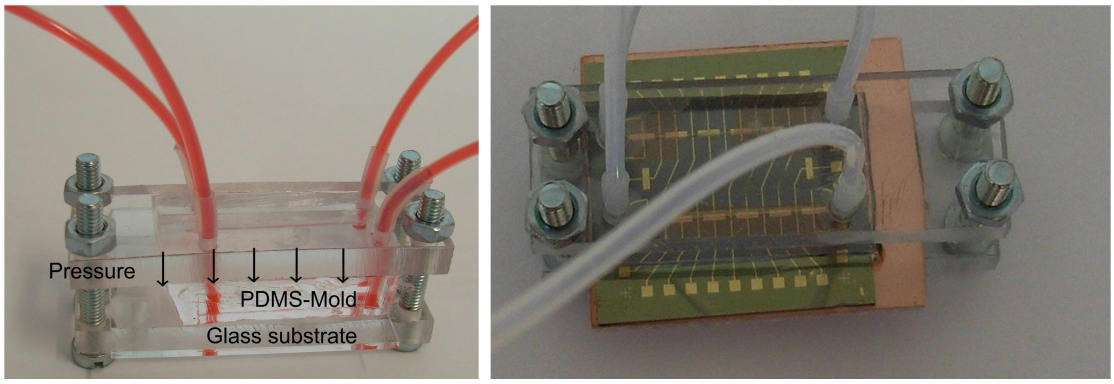

Figure 69: Left; PDMS mold sealed with the pressure assisted reversible bonding onto a glass substrate. Red dyed water was run through the channels of the chip. Right; PDMS mold sealed with pressure assisted reversible bonding onto a SiO_2 substrate with gold electrodes on top. The gold electrodes were fabricated by a lift off process. The electrodes were sealed.

The main disadvantage is that optical observation of the system is hindered by the plate necessary to apply the pressure. Another drawback is that channels sensitive to external stresses tend to collapse. Hence, this approach is not suitable for our purposes.

7.2. Plasma activated bonding

As already discussed in chapter 4.2, on page 52, the oxygen plasma enriches the PDMS, SiO_2 and glass surface with OH groups. These OH groups on the PDMS mold and the surface OH groups of the SiO_2 / glass substrate condense via a silanol condensation forming a strong covalent Si-O-Si bond. The parameters of the oxygen plasma activation, power, and time and oxygen pressure have to be well adjusted in order to achieve a good bonding quality. The values of the oxygen pressure can be taken from the literature, whereas the power which is actually coupled into the plasma differs from the power fed into the generator and strongly depends on the plasma oven used. If the power is adjusted poorly the activation process is very sensitive to the exposure time and oxygen pressure variations [**54**] since the rate of degradation (creation of SiO_x) is very high compared to the formation of OH groups. Thus, it gets very difficult to find a time window where the backbone degradation is acceptable and the OH group density sufficient (see chapter 4.2). Parameters which are commonly used to achieve a good bonding quality found in literature are an oxygen pressure of 0.6 mbar and activation times between 10 s and 150 s at a power of 50 W. [**54**] Therefore, it seemed reasonable to use an oxygen pressure of 0.6 mbar. The powers examined were 50 W and 100 W and the exposure times ranged from 6 s to 10 min.

A peel test was performed in order to quantify the bonding quality. The peel test is basically done by peeling off the PDMS mold bonded onto the substrate. The bonding quality is then defined as the ratio between the reversible bonded area to the irreversible bonded area. It's important to mark that the bonding quality is stochastic and also depends on other parameters like the substrate treatment prior to plasma activation and how the PDMS sample has been placed on to the substrate. These random effects are believed to be included by determining the variance of the bonding quality, i.e. by doing statistics. In order to bond microfluidic chips reliably, the mean bonding quality has to be good and the variance of this bonding quality has to be small (see in the appendix in chapter IV), on page 111 for details).

The PDMS molds used for this test are fabricated by the standard procedure of simple PDMS molds and they were cured at 100 °C for 1 h. The plasma oven has been flushed at a pressure of 0.6 mbar with oxygen for 15 minutes. The results of the bonding quality as a function of plasma activation time between the plasma activated PDMS samples and the substrates which were activated at the same time are shown in figure 70. According to the peel test results, the future working point for glass and SiO_2 will be 50 W at an oxygen pressure of 0.6 mbar and an activation time of 1 min. This point is in the middle of a "plateau" with little variance and high bonding quality. The bonding quality at 100 W does not have a "plateau" and a working point at this activation power would be very sensitive to activation time and oxygen pressure variations.

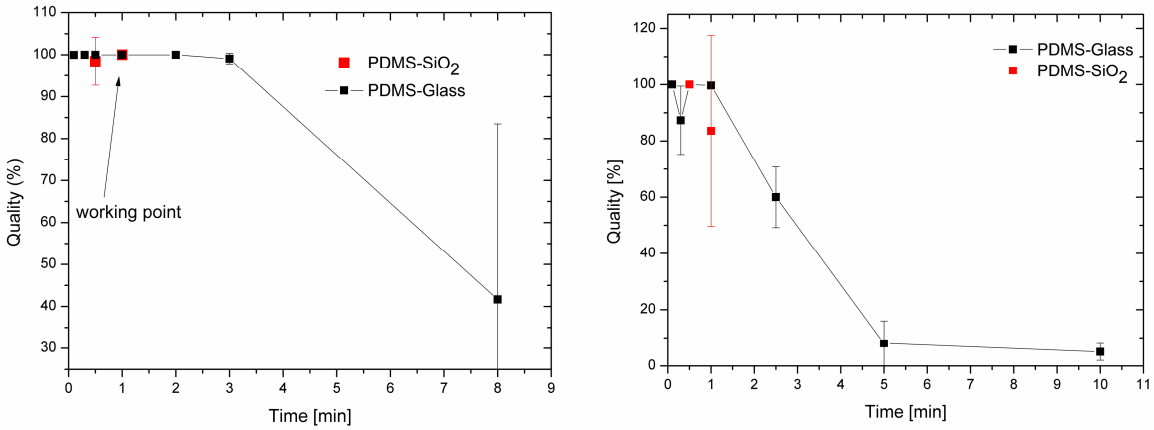

Figure 70: Bonding quality as a function of plasma activation time (results peel test); plasma activation at 0.6 mbar and 50 W (left) and 100 W (right). The black line shows the bonding quality between activated glass and PDMS. The red line shows the bonding quality between activated PDMS and activated SiO_2. The error bars correspond to the variance.

Besides that, following additional observations were made:

- All substrates, glass and SiO_2 as well as the PDMS have to be activated before bonding. In the case of glass substrates, bonding was achieved one time without activating the glass substrate. However, this is dependent on the glass type and was not reproducible. The OH groups on glass and SiO_2 adsorb organic molecules which hinder bonding. Plasma activation cleans the substrate from these contaminants. [**1**], [**67**]
- The bonding quality as a function of time after plasma was also examined. No changes in bonding quality were detected if the samples are bonded within 10 minutes after plasma activation. However, longer times can lead to a worsening of the bonding quality. [**60**] It is believed that this basically depends on the sample treatment after plasma activation (e.g. contamination, bending).
- It was further observed that the bonding after the activated PDMS was placed onto the substrate takes less than a minute. But still, if the PDMS stamp is pooled away right after the contact, no bonding occurs at all. It's therefore important that the PDMS stamp is placed at the first attempt. Thus, retracting or aligning the sample isn't possible. A way to circumvent this problem is by drop casting DI water onto the activated PDMS stamp (B.H. Jo [**60**] used methanol). The water layer protects the sensible activated surface and the PDMS mold can be aligned on the substrate. The water has to be evaporated subsequently on a hot plate. However, this alignment procedure was not optimized.
- If one wants to partially bond PDMS, one can either shield the substrate or the PDMS stamp from plasma activation by a scotch tape or by placing a glass sheet on top. Note that it is important to squeeze out any air bubbles underneath the glass sheet. An example of partially bonding is shown in figure 68.

7.3. Stamp and stick bonding

The stamp and stick bonding (SSB) is a non-invasive technique. This technique can for example be used to integrate sensible organic field effect based sensor (SensFETs) into microfluidic systems. The fabrication and the principles of such SensFETs are discussed in reference [**68**]. One major problem of these systems is that the organic active layer is very sensitive to oxygen and water vapor. Thus, bonding techniques like plasma activation are usually prohibited. Further, the stamp and stick bonding technique also allows to seal electrodes and rough surfaces which is a major advantage compared to pressure assisted bonding (see figure 71 right at the bottom).

Figure 71 illustrates the stamp and stick bonding technique. An adhesive is spin coated onto a substrate and then the PDMS mold is placed on this substrate. Some of the adhesive stays on the PDMS mold after its removal. The PDMS mold is then placed on the substrate of the chip and the adhesive is cured subsequently.

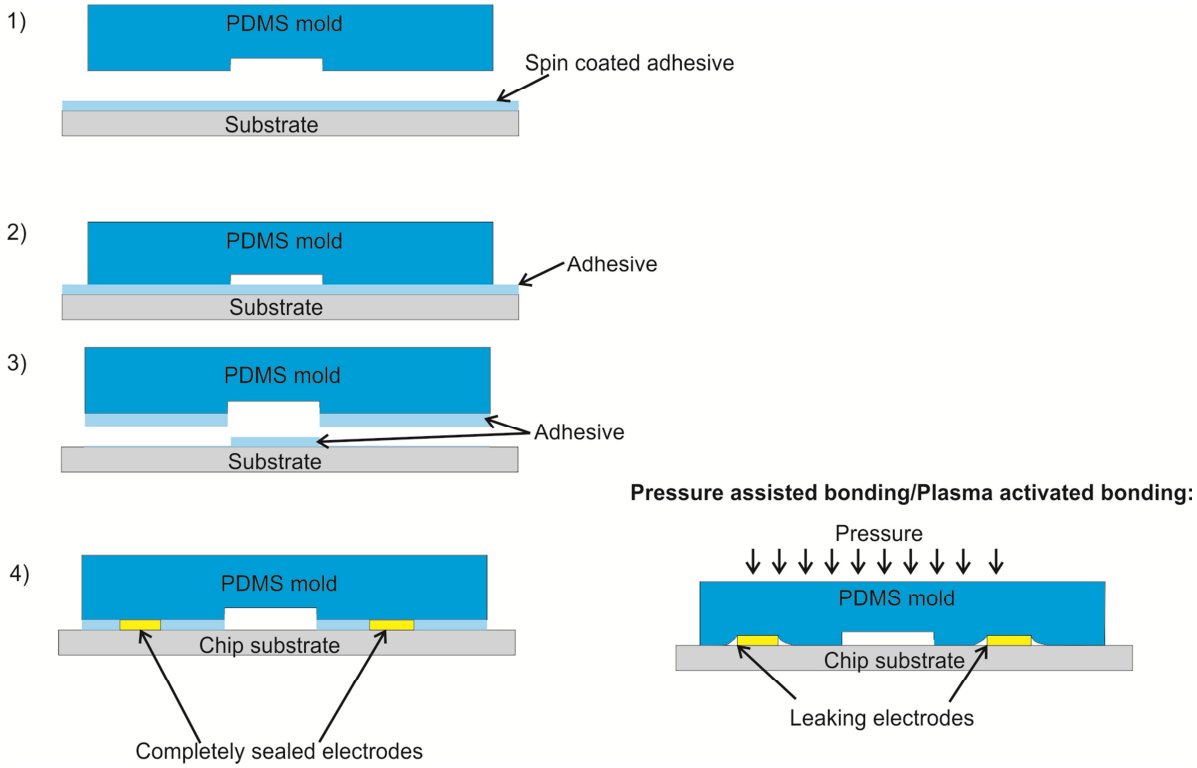

Figure 71: Left; stamp and stick bonding process. 1) The adhesive is spin coated onto a substrate. 2) The PDMS mold is placed onto the substrate. 3) The PDMS is removed from the substrate. The adhesive is transferred on to the PDMS mold. 4) The PDMS mold with the adhesive is placed onto the final substrate. Right; Scheme of pressure assisted / plasma activated bonding onto a substrate with electrodes. The electrodes can't be sealed completely.

Concerning the adhesive, PDMS pre-polymer and curing agent seem to be a good choice because they show a strong adhesion to SiO_2, glass and also to the PDMS mold upon curing (see chapter 4.1.1 for details). [**63**] [**64**] [**65**] Another advantage of these two adhesives is that curing can be done at RT under inert conditions in an argon glove box. Since PDMS pre-polymer adhesive has a high viscosity, it is impossible to spin coat a thin adhesive layer without diluting it with toluene. Another issue to look at is the bonding strength for plasma activated, completely cured and partially cured PDMS molds. The adhesive / mold combinations investigated are listed in table 1.

Table 2: Stamp and stick bonding: adhesives and mold combinations investigated in this work

PDMS Mold	Adhesive
Partially cured at 50 °C 1 h	PDMS
	PDMS diluted with toluene (1 : 6)
	PDMS diluted with toluene (1 : 1)
	Curing agent
Completely cured at 100 °C, 1 ½ h	PDMS
	Curing agent
Completely cured and plasma activated	PDMS
	Curing agent

In order to investigate the bonding quality of the mold - adhesives combinations mentioned above, a pressure test has been performed. This test is done by increasing the pressure in a reservoir until it leaks (see appendix in chapter IV)).

After the pressure test were performed the stamp was peeled off the substrate to further examine the bonding quality between the substrate, the adhesive and the mold. The bonding quality is determined by two interfaces. First there is the interface between the adhesive layer and the SiO_2 and secondly there is the interface between the PDMS stamp and the adhesive layer. The bonding quality between the interfaces can be investigated by tearing off the mold. Ideally the second interface vanishes, meaning that the adhesive layer is completely cross-linked to the PDMS-bulk and that the chemical structure and mechanical properties are the same. The adhesive layer should therefore be indistinguishable from the PDMS bulk. As far as the SiO_2 interface is concerned, the adhesive layer should bond as good as possible.

The results are discussed starting with the adhesive PDMS pre-polymer undiluted / diluted with toluene. The results obtained using curing agent as an adhesive are elucidated subsequently. This chapter gives a summary of the results obtained, the fabrication processes like spin coating are discussed in the appendix in chapter IX).

7.3.1. PDMS pre-polymer as an adhesive

The results of the pressure tests using PDMS pre-polymer as an adhesive are listed in table 3. It can be seen that the best results were obtained for partially cured and completely cured plasma activated PDMS molds in combination with undiluted PDMS pre-polymer as an adhesive (6 bar). In this case no residual layer was observed after peel off (see figure 72 right). If the PDMS pre-polymer was diluted with toluene, on the other hand, a residual layer stayed on the substrate. This layer seemed to get thinner with increasing toluene concentration. As shown in figure 72 on the left (PDMS : toluene, 1:6) and in the center (PDMS : toluene, 1:1). If the PDMS mold was completely cured without plasma activation the adhesion was not as strong (4.5 bar) and a residual layer could again be observed on the substrate after peel off even if undiluted PDMS pre-polymer was used as an adhesive.

The presented results principally agree with those in literature. M. A. Eddings and coworkers [**69**] investigated PDMS molds bonded onto other PDMS molds by the SSB technique using PDMS pre-

polymer as an adhesive. They obtained bond strengths, determined by a pressure test, of 6.5 bar. . H. Wu and coworkers [**63**] measured the bond strengths of completely and partially cured PDMS molds which have been bonded onto glass substrates by SSB using PDMS pre-polymer as an adhesive. The bond strength of completely cured PDMS molds, was around 4 bar, whereas the bond strength of partially cured PDMS molds was stronger than the PDMS-bulk.

Table 3: Results stamp and stick bonding with PDMS pre-polymer as an adhesive

Mold	Adhesive	Pressure test	Peel test
Partially cured	PDMS:toluene (1:6)	2.5 bar	Thin layer (see figure 72 left)
Partially cured	PDMS:toluene (1:1)	6 bar	Thick layer (see figure 72 center)
Partially cured	PDMS	6 bar	No layer (see figure 72 right)
Completely cured	PDMS	4.5 bar	Thick layer (see figure 72 center)
Completely cured and plasma activated	PDMS	5 bar	No layer (see figure 72 right)

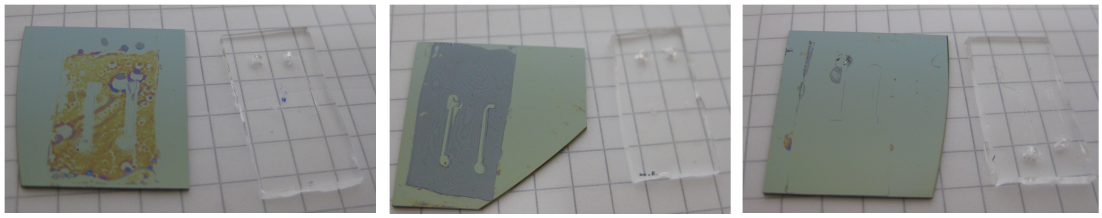

Figure 72: Exemplary images of PDMS molds and substrates after peel off (peel test). There were basically three different layers left on the substrate after peel off. Either a thin (left) or a thick (center) residual layer stayed on the SiO_2 substrate after peel off or there was no layer at all (right).

As a conclusion we can state, that if the mold is completely cured prior to SSB, a thin PDMS layer is left on the SiO_2 surface. This indicates that the PDMS adhesion layer adheres stronger to the SiO_2 surface than to the mold. A possible explanation can be that if the mold is completely cured, all polymers at the surface are cross-linked and as a consequence the bonding quality adhesive – mold is decreased. In the case of a partially cured mold there are still uncross-linked polymers available. This increases the bonding strength mold – PDMS adhesive and therefore no residual layer is left on the substrate. Plasma activation induces OH groups on the surface of the mold which are believed to be cross-linked by the adhesive, increasing its adhesion to the mold. Again, no residual layer is left on the SiO_2 substrate after the mold has been torn off.

Diluting the PDMS with toluene leads to decreasing thinner layers with increasing dilution ratio, but also causes a swelling of the PDMS mold. This leads to a worsening of the bonding quality between the mold and the diluted PDMS pre-polymer. If the mold is peeled off, a thin layer stays on the SiO_2 surface, even if the molds were partially cured prior to bonding. This could be due to mechanical stress induced by the swelling between the mold and the adhesive layer.

7.3.2. Curing agent as an adhesive

As a second adhesive PDMS curing agent was used and the bonding quality between substrate and mold were evaluated by pressure tests whose results are listed in table 4. It can be seen that the highest bonding quality is achieved if a partially cured mold was used (6 bar). If the PDMS was

completely cured and plasma activated no bonding was achieved at all. The peel test showed that a thin residual layer was left on the substrate after peeling off the mold. In the case of plasma activated PDMS-mold this layer was lubricious, i.e. it could be transferred another time if this PDMS mold was placed onto another substrate. This is probably because the curing agent / LWM cannot diffuse through the thin, polar OH surface layer into the bulk / out of the bulk. This leads to an uncured, liquid layer between the mold and the substrate. The result principally agree with those obtained in literature, B. Samel et al. [**65**] used curing agent as an adhesive to bond completely cured molds onto a glass substrate achieving bonding strengths of 3 bar.

Table 4: Pressure test results of SSB using curing agent as an adhesive.

Mold	Adhesive	Pressure test	Peel test
Partially cured	Curing agent	6 bar	Thin layer (see figure 72 left)
Completely cured	Curing agent	4 bar	Thin layer (see figure 72 left)
Completely cured and plasma activated	Curing agent	0 bar	Liquid layer (see figure 72 left)

7.3.3. Applications of SSB

As mentioned before, one of the major advantages of the SSB is that it can be used to integrate SENSFETs into microfluidic systems and to seal electrodes. An example of the latter is shown in figure 73.

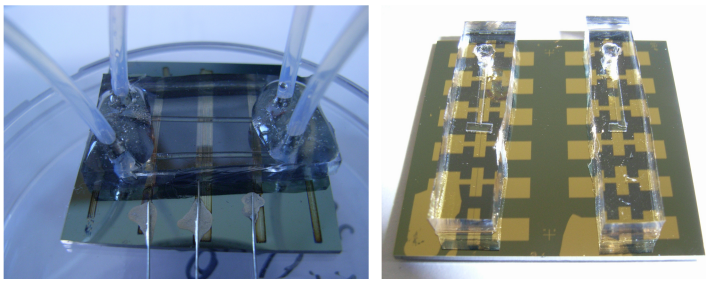

Figure 73: Completely cured PDMS mold bonded by SSB onto a substrate whose electrodes were structured by inkjet printing with Ag-ink (left) and onto a substrate whose Au electrodes were structured by a lift off process (right). PDMS pre-polymer was used as an adhesive. Leaking occurred around 2-2.5 bar.

The bonding quality of the microfluidic chips shown in figure 73 was verified by a pressure test and it turned out that the sample on the left (2.5 bar) seals remarkably better than the sample on the right (1 bar). This could have two reasons. The first one is that the SiO_2 surface gets contaminated by the resist used for the lift of process impeding a good adhesion between the PDMS-pre polymer and the SiO_2. The other one would be that the Ag electrodes adhere stronger to the PDMS pre-polymer than the gold electrodes due to OH groups on the Ag surface.

A SensFET based microfluidic device is shown in figure 74 and figure 75. This device was fabricated by spin coating polyvinyl alcohol (PVA) pre-polymer onto the SensFET device which has been fabricated as described in reference [**68**]. The completely cured plasma activated PDMS mold was then bonded on this device by SSB using PDMS-pre polymer as an adhesive. Subsequently, the whole system was cured leading to cross-linked PVA polymer and PDMS polymer. The PDMS pre-polymer shows a strong adhesion to the PDMS mold as well as to cross-linked PVA allowing leak free fluid

injection at pressures up to approximately 1 bar. Furthermore if the PDMS mold is peeled off, the cross-linked PVA layer is torn off with it without damage. Thus, the PVA layer serves as a cap for the microfluidic channels and one can pump liquid through these channels without leakage (see figure 77). The strong adhesion between PDMS adhesive and PVA could be due to a cross-linking between the PDMS pre-polymer and the PVA pre-polymer (see chapter 4.1 for details). It is important to mark that the whole procedure was carried out in a argon glove box in order to protect the sensible semi conducting organic layer from oxygen and water vapor.

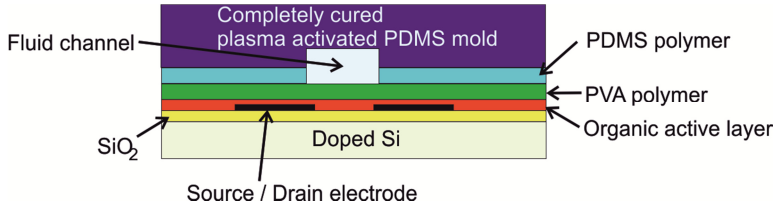

Figure 74: Scheme of an SENSFET based microfluidic system. The PDMS mold is bonded onto the SensFET by SSB using PDMS pre-polymer as an adhesive.

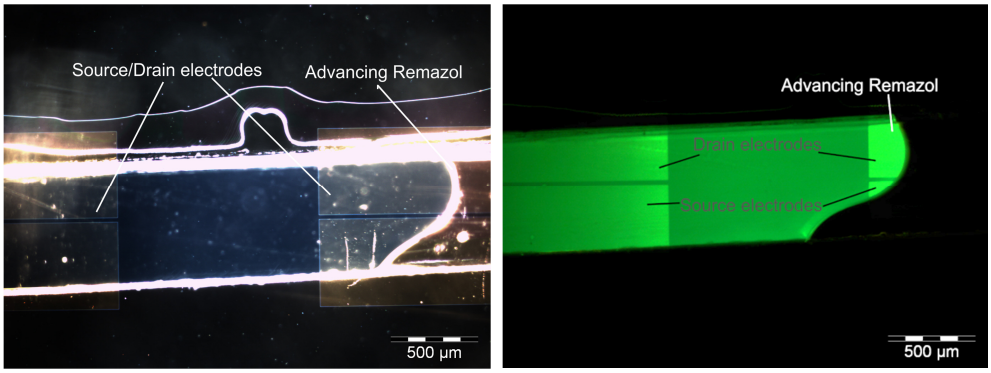

Figure 75: Left; image made with an optical microscope of a SensFET base microfluidic device filled with Remazol. Right; Image made with fluorescence microscope of a SensFET base microfluidic device filled with Remazol. The microfluidic channel is filled and no leaking can be observed.

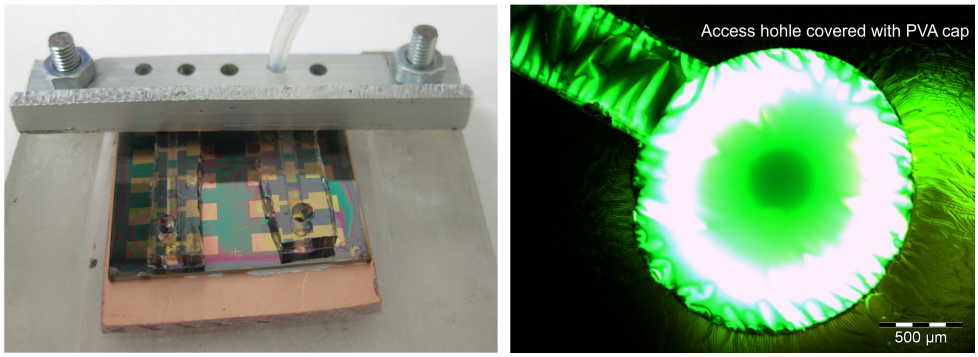

Figure 76: Left; connected SensFET based microfluidic device filled with fluorescent Remazol. The fluid can be injected at pressures of 1 bar without leaking. Right; If the PDMS mold is peeled off, the cross-linked PVA layer is torn off with it without damage. Thus, one can fill the microfluidic channels from below and the cross-linked PVA serves as a cap sealing the microfluidic channels.

7.4. Bonding conclusion

One key issue of microfluidic systems is the bonding between the mold and the substrate. Thus, several bonding techniques such as pressure assisted reversible sealing, SSB and plasma activated bonding were investigated. It turned out that pressure assisted reversible sealing is not suited for optical microscopy and consequently not suited for our purposes. For that reason the irreversible bonding techniques SSB and plasma activated bonding were examined in detail. The bonding strength of these techniques was quantified by pressure tests and the results are shown in figure 77. It can be seen that plasma activated bonding shows the best bonding quality on smooth and clean plasma activated SiO_2 / glass substrates. However, SSB can be used to seal electrodes / rough surfaces and to integrate sensFETs into microfluidic systems. As far as SSB is concerned, undiluted PDMS pre-polymer and a partially or plasma activated stamp are preferable (they seal pressures up to 6 bar). If a thin adhesive layer is desired, one can dilute the PDMS 1:1 with toluene. Further dilution is not recommended because the adhesion between the mold and the substrate is weakened. Another problem occurring if the PDMS pre-polymer gets diluted with toluene is that it swells the PDMS and as a consequence, small structures could be destroyed.

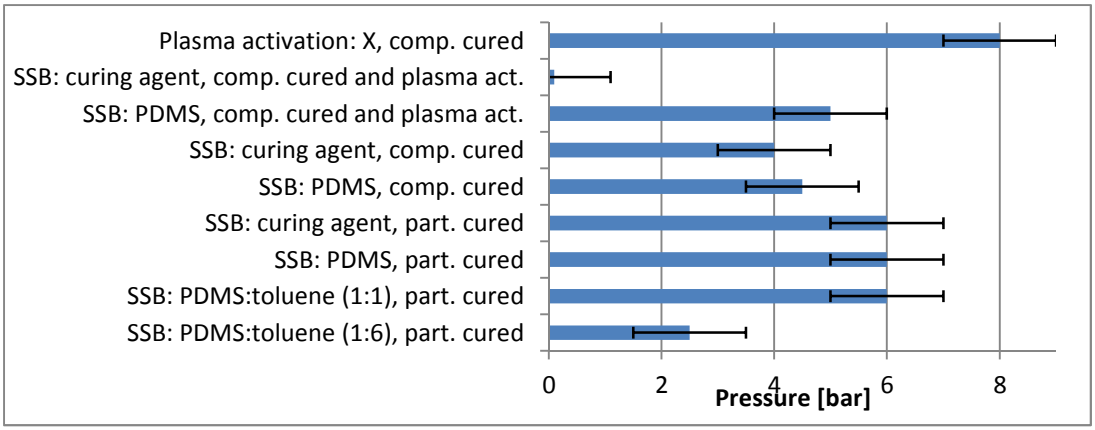

Figure 77: Results of the pressure test of the oxygen plasma activated bonding and the stamp and stick bonding with different adhesives and molds. The labeling is the following: "Bonding technique: adhesive used, mold type"

Thus, two bonding techniques were implemented. Plasma activated bonding can be used to seal microfluidic devices reliably onto smooth and clean SiO_2 / glass substrates sealing pressures up to 8 bar. SSB can be used to bond molds onto electrodes / rough surfaces and to integrate SensFETs into microfluidic systems. These sensors were integrated into a microfluidic device by using PVA as an intermediate layer between the semiconducting organic layer and the fluidic channel. This PVA layer showed remarkably good adhesion to the PDMS adhesive layer. SensFETs can detect low concentration of analytes through inherent signal amplification [**68**] and consequently they are very interesting concerning microfluidic sensing systems since the number of detectable molecules in microfluidic channels is small (see chapter 1). A possibility would be for example, to do sample pre-treatment like filtration and mixing automatically in a microfluidic system whose outlet channels are then analyzed by sensible SensFETs.

8. Connecting the chip

After the microfluidic chip is fabricated it has to be connected to the macroscopic world, e.g. to syringes. The connection macroscopic-microscopic world, the so called interconnects and the subsequent injection of fluids into the chips via syringe pumps will be discussed in the following chapters.

8.1. Interconnects

The microfluidic chip has to be connected to the macro world, e.g. a syringe / tube, via a so called interconnect. However, these interconnections pose a problem since there is no “interconnection” standard and suitable interconnects are not commercially available. Therefore, proper interconnects had to be designed and developed. There exist two types of interconnects which will be discussed in the following; reversible and irreversible ones. Reversible interconnects can be re-used, whereas irreversible interconnects can’t.

8.1.1. Irreversible interconnects

Irreversible interconnects were fabricated by sealing a tube which has been inserted into the access hole with epoxy or PDMS pre-polymer adhesive. The tubes used were either made out of silicon, Teflon or PVC. A sample of such irreversible interconnects is shown in figure 78.

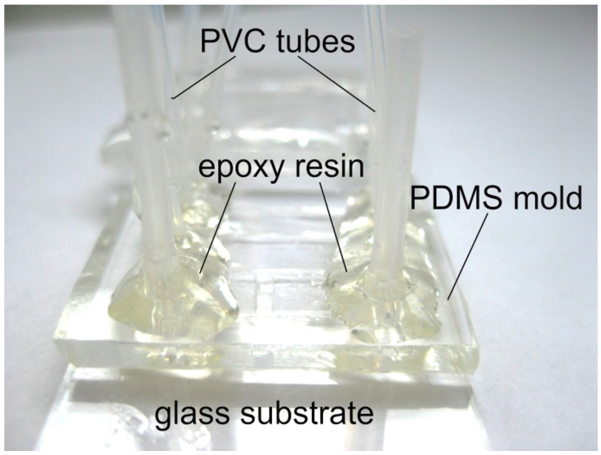

Figure 78: Irreversible interconnects made with an epoxy resin and PVC tubes.

The main problem is that the quality of these interconnects determined by pressure tests were irreproducible. However, the overall trend showed that PDMS pre-polymer as the sealant in combination with silicon tubes lead to the best results. These interconnects could seal pressures up to 5 bar because the PDMS pre-polymer adheres to PDMS as well as to the silicon tubes. The combination epoxy as an adhesive and PVC tubes did not yield reproducible results since the epoxy adhesive does not adhere to the PDMS.

Non-flexible Teflon tubes would be preferable because they are chemically inert and high pressures can be applied without inflating them. Mentioned tubes show poor adhesion to epoxy resist as well as to PDMS pre-polymer. Another problem is that the interconnects made with Teflon tubes are very sensitive to deflections, e.g. if a Teflon tube sealed by epoxy resin gets deflected the interconnect starts to leak.

In addition, the possibility of inserting a plasma activated silicon tube into the access hole in order to achieve a sealing between the silicon tube and the PDMS has been investigated. It turned out that it's impossible to insert the silicon tube into the access hole due to a very strong friction and that if the hole is made wider, the silicon tube does not adhere to the PDMS anymore.

As a conclusion one can say, that it is not preferable to use irreversible interconnects. For that reason another approach is chosen.

8.1.2. Reversible interconnects

Irreversible interconnects aren't very practical, especially for fluid injection at high pressures (> 1 bar, see chapter 8.2 for details). For that reason reversible interconnection systems are preferable. Reversible interconnects range from simply connecting the channel by a syringe [**70**] to specially designed pressure assisted interconnects which are sealed by some sort of O-ring [**71**], [**72**], [**73**]. The point is, that the fabrication of these different O-ring systems is complicated. D. Snakenborg [**74**] replaced the O-ring systems by soft silicon tubes. This system is not suited for high pressure applications due to the elasticity of the soft silicon tubes. For that reason, Teflon tubes were inserted into the silicon tubes. It turned out that this system which is shown in figure 79, is very practical and reliable.

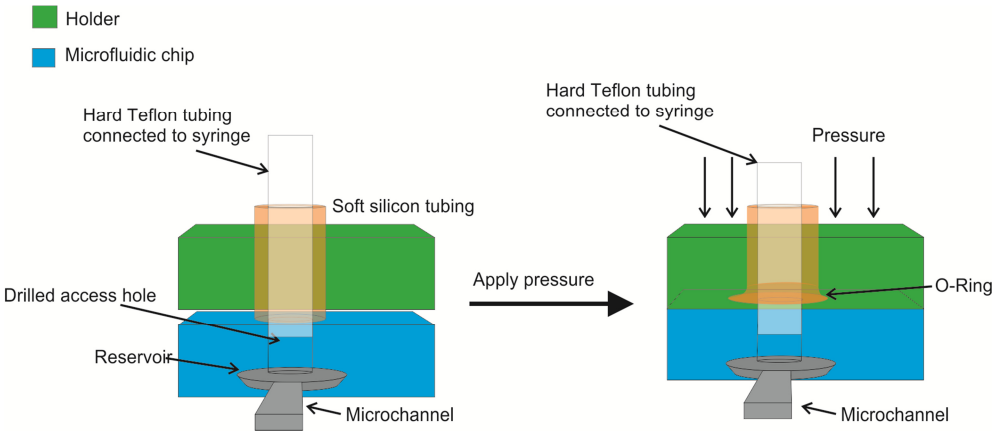

Figure 79: Scheme of reversible interconnects: A soft silicon tube forms an O – ring which seals the hard Teflon tube. This system turned out to be very practical.

The Teflon tube is inserted into a slightly bigger silicon tube. This tube is then inserted into a plate, which has been made out of Plexi glass first (see figure 80, left). Later on, it has been made out of metal which doesn't bend if a pressure is applied (see figure 80, right). The silicon tube sticks out for about 0.5 mm and the Teflon tube sticks out for further 1 mm. The plate is then lowered over the chip and the Teflon tube is inserted into the access hole which has a diameter which is large enough for the Teflon tube but too small for the soft silicon tube to penetrate into the hole. This way the soft silicon tube forms an O-ring around the Teflon tube, sealing it (see figure 79, right).

The huge advantage of this system, other than being reversible, is that the fluid can be injected into the tubes prior to connecting them. This way, the tubes are already filled upon injection and the fluid is already as close to the microfluidic chip as possible. Thus, it is not necessary to push out the air of the whole tube which can take hours.

Experiments showed that pressures up to 1 bar can be sealed safely. The maximum pressure which can be sealed depends on the pressure which is applied from above via the plate. We could also seal pressures up to 8 bar if the tubes are properly aligned, but it is still not recommended to use pressures higher than 1 bar because a slight misalignment can lead to leaks at higher pressures.

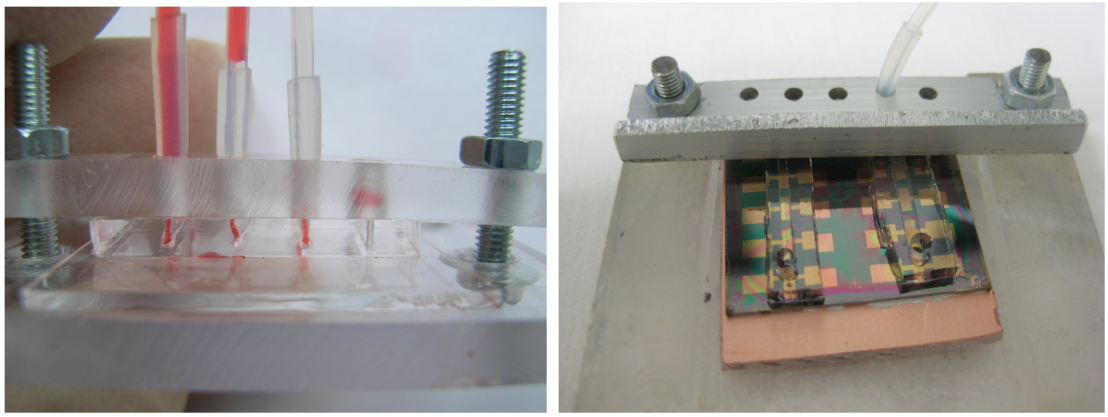

Figure 80: Reversible interconnection of a microfluidic chip. Reversible interconnect with a Plexi glass holder (left) which is not very stiff. Consequently, it is bend if a pressure is applied and the interconnects at the edges are sealed better (higher pressure) than the ones in the center (lower pressure). For that reason the Plexi glass was replaced by a stiff metal bar (right).

8.2. Fluid injection into a microfluidic chip

The experimental setup of a connected microfluidic chip is shown in figure 81. The Teflon tubes of the interconnects are connected to a syringe and this syringe is then clamped onto the syringe pump. Afterwards, the microfluidic chip is placed underneath an optical microscope for analyses and evaluation and fixed by scotch tapes.

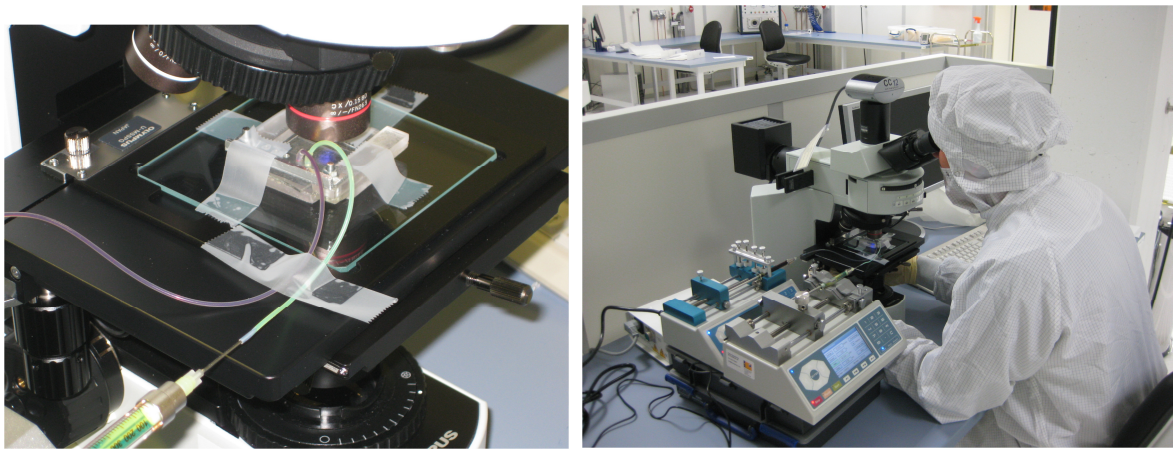

Figure 81: Experimental setup; a microfluidic chip is connected to syringe pumps. Left; microfluidic chip placed underneath the microscope for optical observation. The tubes are fixed by scotch in order to avoid a moving of the tubes during observation. Right; two syringe pumps connected to a microfluidic chip.

Syringe pumps (Fusion 400, Nexus 3000) create a steady flow rate but they don't have any pressure sensors. If the flow rate is chosen too high, pressure will slowly be build up in the microfluidic chip. As the pressure increases either the syringe pump stalls, the interconnects start to leak or in the worst case the bulk PDMS blows up. Neither of this is very pleasant. For that reason, the maximum flow rate possible at a maximal pressure should be estimated before injecting the fluid.

Another issue to consider is that syringe pumps have a step motor and thus also a minimal step size. The minimal step size of the Fusion 400 pump is 20 nm and of the Nexus 3000 pump 12 nm. In order to achieve a continuous flow there should be as many steps per second as possible. Taken for example a flow rate of 10 µL/h, with a syringe of an inner diameter of 4.61 mm (1 mL syringe). The plunger of the syringe has to move with an average velocity of 40 nm/s which corresponds to 2 steps (Fusion 400) and 3.3 steps (Nexus 3000) per second. This does not correspond to a continuous flow. It is believed that the flow rate should be at least higher than 30 µL/h (standard 4.61 mm syringe), in order for the flow to be considered continuous.

Please note: Bending the tubes also changes the flow rate and the applied pressure. Any movements or touching of the tubes should therefore be avoided during pumping.

8.3. Conclusion – connecting the chip

The microfluidic chip has to be connected to the macro world to a syringe / tube via a so called interconnect. There are no commercially available interconnects and therefore, proper interconnects had to be designed and developed. It turned out that irreversible interconnects were not practical and their quality (maximum pressure they can seal) was not reproducible. Whereas reversible interconnects fabricated with a combination of soft silicon and hard Teflon tubes were reliable and practical. This interconnection system could safely seal pressures up to 1 bar.

The fluid flow in the microfluidic system was created by syringe pumps (Fusion 400 and Nexus 3000), connected to the chip via reversible interconnects and stiff Teflon tubes. The maximal flow rate in the channels of the chip is determined by the maximal applied pressure the system can withstand (1 bar) whereas the minimal flow rate is determined by the minimal step size of the syringe pumps (at least > 30 µL/h using a 4.61 inner diameter 1 mL syringe).

9. Nano- / Micro- fluidic devices principles and validation of function

First of all, the inkjet printed chip is discussed. Then microfluidic chips made by EBL are presented.

9.1. Microfluidic systems fabricated by inkjet printing

The master fabricated by inkjet printing is shown in figure 82. The chip had two T-junctions one of which had a meander. This meander was used to prolong the channel.

First, the laminar flow has been examined. After that, the master was used as a droplet / plug generator which is discussed at the end.

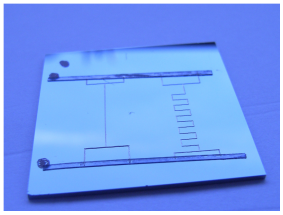

Figure 82: Master structured by inkjet printing using Ag ink. Two T-junctions: The right one has a meander to prolong the channel length.

9.1.1. Laminar flow

Two liquids, one colored red with „Sissi Lebensmittelfarbe“ and Remazol which is a water solvable fluorescent dye got injected into the T-junction (see figure 83). The liquids were filtered by a 200 nm filter prior to injection.

Before injecting the fluids, one has to calculate the maximum flow rate and also the average flow velocity at a certain pressure. The following assumptions were made in order to calculate the average flow rate at a certain pressure: The access channels to the T-junction were neglected and it was supposed that liquids in the mixing channel after the T-Junction behave as if they were one liquid. As a consequence, it is assumed that the flow rates of both liquids can simply be summed up. The results are shown in table 5.

Table 5: Characterization of the inkjet printed chip. The values were calculated by the equations given in chapter 2. The surface tension and the viscosity of olive oil have been measured at room temperature.

	Maximal flow rate T-junction		Maximal flow rate T-junction with meander	
	Water	**Oil**	**Water**	**Oil**
Channel height [nm]	20000.0	20000.0	20000.0	20000.0
Channel width [µm]	150.0	150.0	150.0	150.0
Length [µm]	16000.0	16000.0	22600.0	22600.0
Viscosity [kg/(s m)]	1.0E-03 [**10**]	7.0E-02	1.0E-03 [**10**]	7.0E-02
Surface tension [mN/m]	72.00 [**10**]	30.00	72.00 [**10**]	30.00
Contact angle[°]	0.00	0.00	0.00	0.00
Density [kg/m³]	1000.00	861.00	1000.00	861.00
Max. pressure difference [bar]	1.0	1.0	1.0	1.0
Max. flow rate [µL/h]	2250.0	32.1	1592.9	22.8
Max. average velocity [mm/s]	208.3	3.0	147.5	2.1
Time t [s]	1.00	1.00	1.00	1.00
Capillary pressure [bar]	81.60	34.00	81.60	34.00
x(t) [mm]	737.56	56.90	737.56	56.90

The maximum flow rate at the maximal pressure of 1 bar is 2250 µL/h. Thus, both fluids can be injected safely with a maximum flow rate of 1000 µL/h (total flow rate of 2000 µL/h in the mixing channel) without leaking. Optical images were made at the inlet and the outlet (see figure 83).

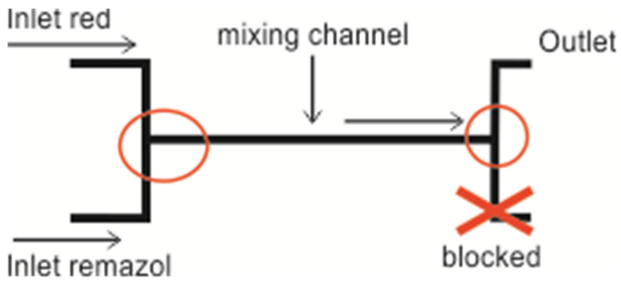

Figure 83: Illustration of the T-junction. Red dyed water and Remazol have been injected into the T-junction. The points which have been observed optically are marked with red circles. The lower arm of the outlet has been blocked.

Both fluids got injected at a flow rate of 40 µL/h which corresponds to 80 µL/h in the mixing channel after the T-Junction where the fluids flow with an average speed of 3.8 mm/s. A fluid element stays 4 s in this mixing channel which is time enough for the dye molecules to diffuse to the other side and for the fluids to mix (see figure 84).

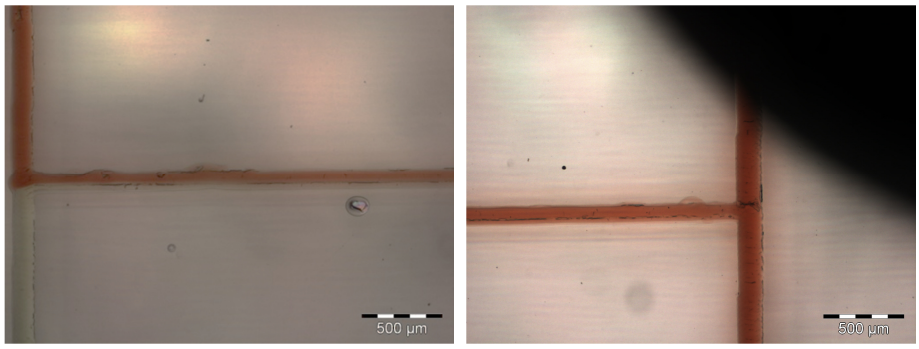

Figure 84: Remazol and red dyed water were injected into a T-junction. The lower arm at the outlet was blocked. The flow rate of both liquids was 40 µL/h. Left; picture made at the inlet of the T-junction. The liquids don't mix and they are in the laminar flow regime flowing parallel without turbulent mixing. Right; picture made at the outlet. The liquids did completely mix.

If the flow rate of both fluids is increased to 1000 µL/h and therefore to 2000 µL/h in the mixing channel, the average time a fluid stays in the mixing channel is around 0.09 s. This is not enough time for the red dye molecules / Remazol molecules to diffuse to the other side of the channel. As a consequence no mixing occurs. It is very interesting to see that the fluid flows around the corner at the outlet without noticing it, indicating purely laminar flow.

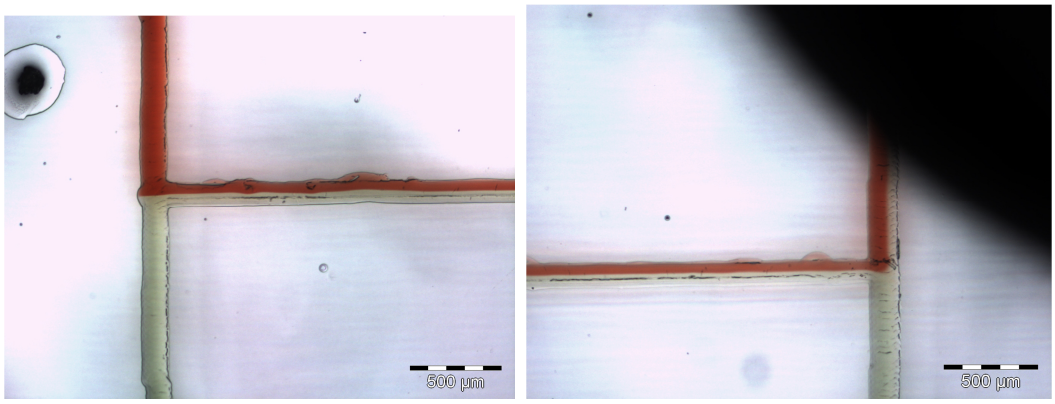

Figure 85: Remazol and red dyed water injected into a T-junction. The lower arm at the outlet was blocked. The flow rate of both liquids was 1000 µL/h. Left: Picture made at the inlet of the T-junction. The liquids did not mix and they are in the laminar flow regime. Right: Picture made at the outlet: The fluids did not mix at these high flow rates.

9.1.2. Droplet / Plug generator

In order to create droplets, olive oil and blue colored water are injected into the T-junction. The water and oil had been filtered with a 200 nm filter prior to injection. The olive oil can't be seen in microfluidic channels and for that reason, it had been replaced by pumpkin seed oil in a subsequent experiment. It has been supposed that the pumpkin seed oil has the same viscosity and interfacial tension as olive oil. The interfacial tension between the olive oil and the water was measured to be 40 mN/m.

Again the maximum flow rate has been calculated. This time it has been assumed that the mixing channel was filled with olive oil solely. The results are shown in table 5. The maximum flow rate at 1 bar is 32 µL/h, which is at the lower limit of the syringe pump (standard 1 mL syringe with an inner diameter of 4.61 mm). For that reason, the oil has also been pumped at exceptional high pressures of 3 bar driving a flow rate of 100 µL/h through the mixing channel.

The flow rate of the carrier fluid in the droplet regime (Ca < 0.002) has to be smaller than 800 µL/h for water and smaller than 10 µL/h for oil (calculated with equation 2-7). A continuous flow below 10 µL/h can't be achieved by the syringe pumps used (1 mL syringe). Consequently, the droplet regime can only be reached using water as the continuous phase. The flow rate of the carrier fluid in the droplet regime and therefore at Ca numbers between 0.01 and 0.3, has to be between 10 mL/h and 20 mL/h for water and between 100 µL/h and 1800 µL/h for oil (calculated with equation 2-7). Flow rates higher than 2000 µL/h for water are not possible since the required pressure would be too high. Thus, the droplet regime can only be achieved by using the olive oil as the continuous phase. It is important to mark that the flow rates of the dispersed fluid have to be below the flow rates of the carrier fluid.

The oil and the water were injected at flow rates ranging from 30 µL/h to 300 µL/h. Droplet, plug formation and parallel flow has been observed but the results were not reproducible. Some exemplary results are shown in figure 86 and figure 87.

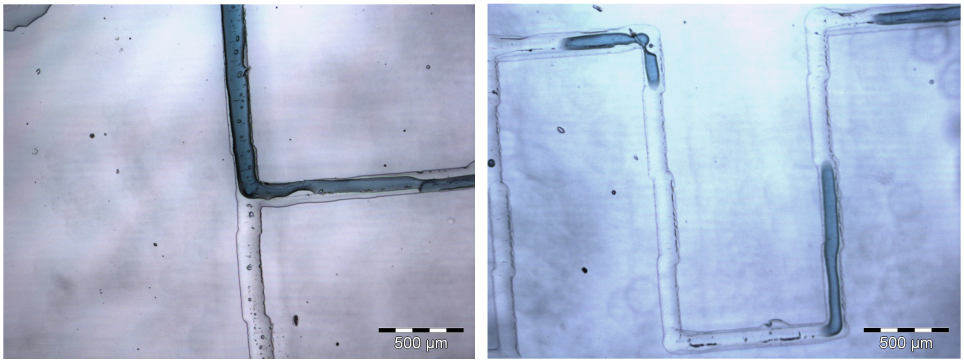

Figure 86: T-junction; olive oil injected from below and blue dyed water injected from above. Parallel flow (left); the water has been injected with a rate of 50 µL/h and the oil with a rate of 100 µL/h. The capillary number would therefore be 0.00012 for water and 0.016 for oil. This would correspond to the plug flow regime. The parallel flow could be caused by the grooves in the channels' ceilings. This would explain the strange stream line of the blue water. Droplet flow (right); The olive oil has been injected at rate of 160 µL/h and the water at a rate of 90 µL/h. The capillary number would therefore be 0.0002/0.026 for water / oil corresponding to the plug / dripping regime. Plugs were generated but this is believed to be due to mechanical instabilities.

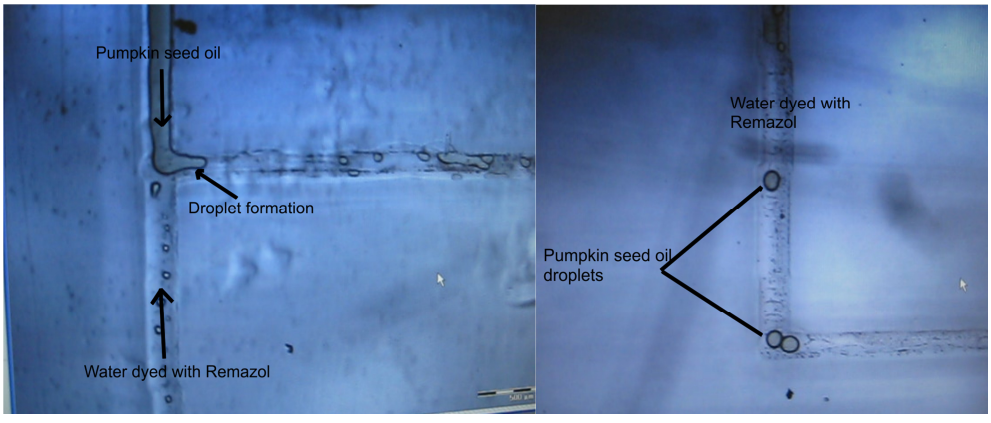

Figure 87: T-junction; water dyed with Remazol injected from below and pumpkin seed oil injected from above. The water has been injected with a rate of 1000 µL/h and the oil with a rate of 15 µL/h. The capillary number is 0.0023 and the system should actually be in a plug flow regime but it is in the droplet flow regime. The droplet formation can be seen on the left. The right picture shows the pumpkin seed oil droplets at the outlet.

The results were irreproducible. This is due to the following problems:

- This geometry is actually not suited for droplet / plug generation. The dispersed phase is usually injected perpendicular to the continuous flow. In this case, the average flow velocity of the dispersed phase would be zero upon perpendicular injection and the average flow rate of the continuous phase can be calculated as in chapter 2.2. However, the average flow rate right at our T-junction of the continuous phase and the dispersed phase is not known. Therefore, it is believed that the actual capillary number also differs from the Ca number calculated with equation 2-7.
- The whole channel is hydrophilic; both olive oil and water wet the channel (contact angle 0°) and the channel walls have grooves. The water / oil can flow in these grooves reducing the contact area between the two phases hindering a droplet / plug formation. Such a groove can be seen in figure 86; the blue dyed water flows from the upper side of the channel to the lower one. This is due to a groove in the ceiling of the channel.
- Another issue to consider is the elasticity of PDMS. PDMS is very soft and deforms if a pressure is applied. This deformation increases the volume of the cavities, around the access holes which are large compared to the channels in the chip. Instead of flowing through the chip, the fluid is stored in this additional volume. Therefore, the fluid volume injected into the system does not correspond to the volume flowing through the system. For that reason, the flow rate pumped by the syringe pump does not correspond to the actual flow rates in the channels. This problem is especially significant for fluids which have a high viscosity like oil. Taken olive oil as example, the pressure required for a flow rate of 10 µL/h in the channel after the T-junction is 310 mbar leading to large deformations of PDMS. As a consequence, the oil continuous to flow for about 30 min at slowly decreasing flow rates, if the pumping is turned off.
- Another problem to consider is that the pressure of the two inlet channels at the T-junction has to be equal. If this is not the case, the oil penetrates into the inlet channel of the water inlet or vice versa. For example, if one starts to pump at a flow rate of oil and water of 10 µL/h. At the beginning the pressure of the water at the T-junction is higher than that of the oil because its viscosity is lower. As a consequence, the water will penetrate into the inlet channel of the oil. The pressure will build up until its high enough to push the water out of the inlet channel. In equilibrium the pressure at the T-junction of both fluids will be equal and both fluids actually flow down to the outlet. However, at high flow rates / pressures the system oscillates around the equilibrium, i.e. the fluids are not flowing parallel in the mixing channel, they are more or less retraced from the T-junction / from the mixing channel inlet. This also creates plugs but these are not due to interfacial forces but to mechanical oscillations of the PDMS.

9.2. Micro- / Nano-fluidic devices fabricated by EBL

The devices created by EBL were a reservoir and a possible mixer. The access channels were fabricated by scotch.

The channels had an average length of 1 mm, a height of 840 nm and a width of 10 µm. The flow rate at a maximal pressure of 1 bar is 0.2 µL/h for water and 0.003 µL/h for oil (see table 6).This flow rate can't be achieved by syringe pumps using a standard syringe with an inner diameter of 4.61 mm. The goal was therefore not to create a constant flow rate but to inject the fluid by applying a pressure. This was done by injecting high flow rates leading to a high pressure and subsequently by turning off the syringe pump.

Table 6: Characterization of the micro / nano fluidic chips structured by electron beam lithography. The values were calculated by the equations given in chapter 2. The surface tension and the viscosity of the oil have been measured at room temperature.

	Maximal flow rate	
	Water	**Oil**
Channel height [nm]	840.0	840.0
Channel width [µm]	10.0	10.0
Length [µm]	1000.0	1000.0
Viscosity [Pa s]	1.0E-03 [**10**]	7.0E-02
Surface tension [mN/m]	72.00 [**10**]	30.00
Contact angle[°]	0.00	0.00
Density [kg/m³]	1000.00	861.00
Max pressure difference [bar]	1.0	1.0
Max. flow rate [µL/h]	0.2	0.003
Max. average u [mm/s]	5.9	0.1
Max. flow rate [µL/h]	0.2	10.0
Max. average velocity [mm/s]	6.61	330.69
Time t [s]	1.00	1.00
Capillary pressure [bar]	1858.29	774.29
x(t) [mm]	147.83	11.41

The injected fluid was water dyed with the fluorescent Remazol. The fluids have to be fluorescent for optical observation. The concentration of the Remazol was chosen to be 2 mg Remazol per mL which yielded the best fluorescence intensity after filtration using a 200 nm filter.

First, the reservoir is discussed, secondly the mixer is presented.

9.2.1. Reservoir

The microfluidic chip prior to filling is shown in figure 88.

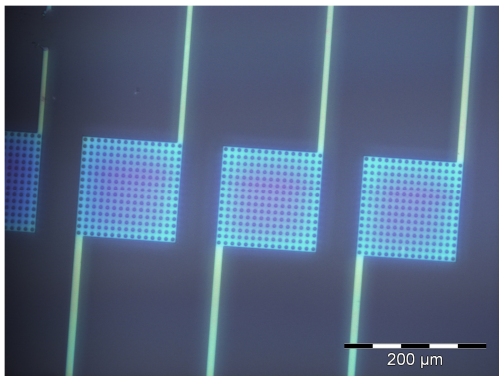

Figure 88: The reservoir device prior to filling. The reservoirs have different colors. This structure is therefore at the limits of the aspect ratio of the PDMS. The channel of the reservoir on the left has been destroyed on purpose in order to study the capillary pressure.

The chip was filled with Remazol right after fabrication. Hence, it has been ensured that the channels were hydrophilic. The chip under operation is shown in figure 89. The outlets of the first three reservoirs from the left have been destroyed on purpose, in order to study capillary pressure.

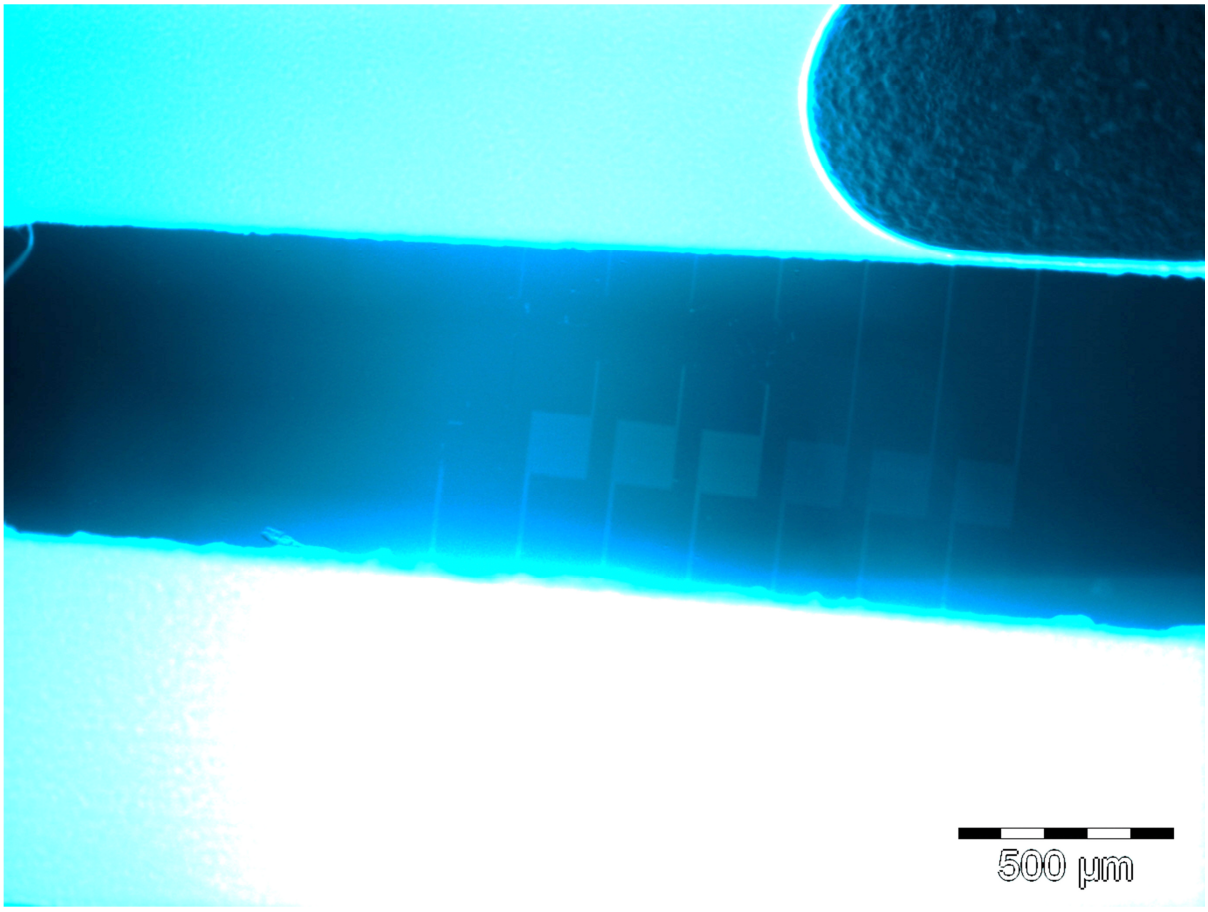

Figure 89: Reservoir filled with water dyed with Remazol. The fluid has been injected from below. The first three reservoirs from the left were filled by capillary pressure. The fluid flows through the last three reservoirs from the right.

There are two interesting aspects to look at. The first one is that the flow rate is higher than expected. The access channel at the top made by scotch with an average height of 100 µm and a width of 300 µm is already filled at a length of more than 1000 µm after ½ h. This corresponds to a minimal flow rate of 60 µL/h. The channels structured by EBL connecting the inlet and the outlet have a length of at least 500 µm. The maximum flow rate at a pressure of 5 bar would therefore be around 5.4 µL/h (calculated with Equation 2-3). Consequently, it is impossible to explain flow rates at this magnitude by the conventional theory with the given channel geometry. The difference between the model and the reality could be due to slipping at the interface channel–fluid (the no-slip boundary condition is violated) or due to an enlargement of the elastic PDMS channels. The latter seems more reasonable because the slipping effect is usually not important in hydrophilic channels. [**8**]

The other aspect is that the channels get filled by capillary pressure immediately after being in contact with the liquid. They even get filled if they don't have an outlet. This is due to the capillary pressure which is high enough to push the air out of the channel. The capillary pressure in these systems was calculated to be 1800 bar.

After Remazol was pumped through the chip, pumpkin seed oil was pumped through from the other side. This oil contains chlorophyll fluorescent red [**75**]. The images are shown in figure 90. Again the flow rate of the pumpkin seed oil is higher than expected.

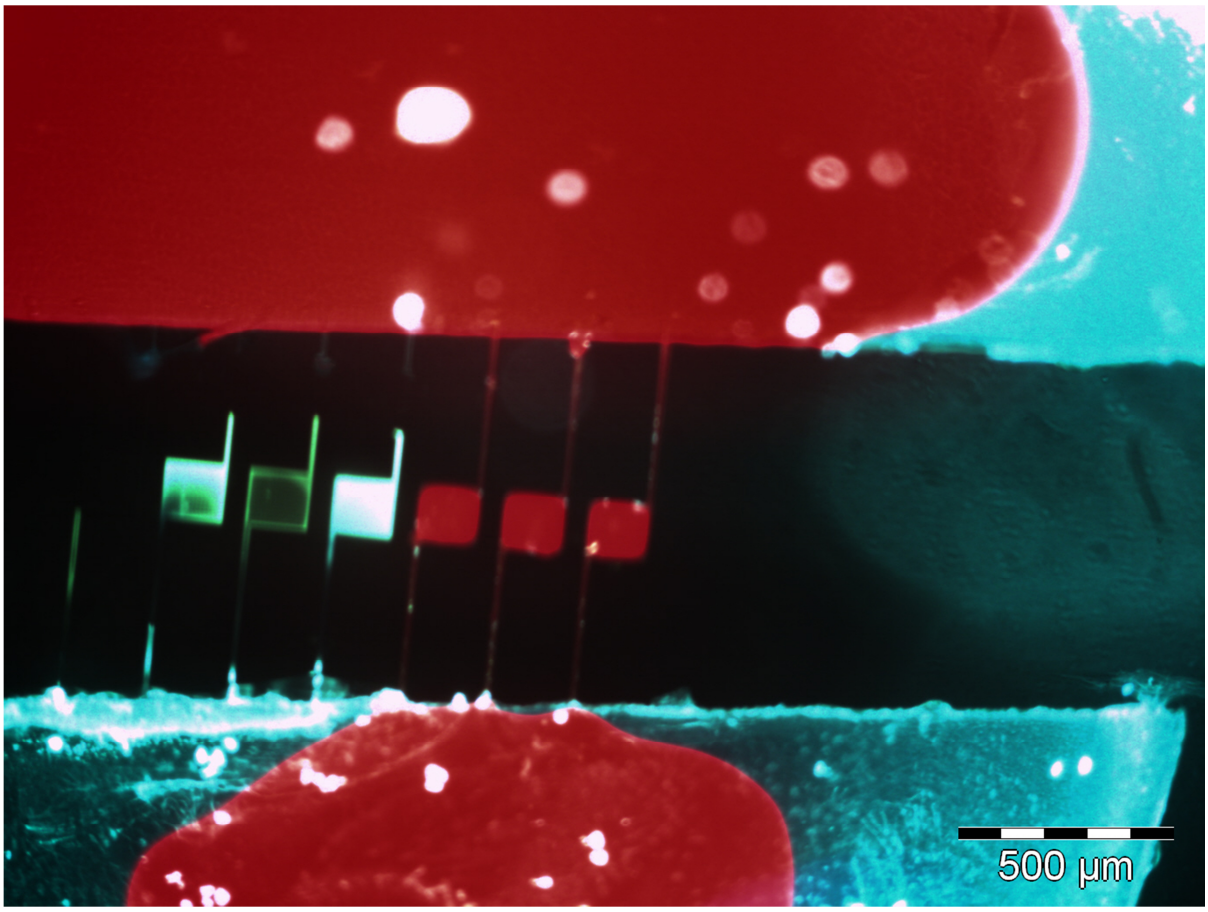

Figure 90: Reservoir filled with water dyed with Remazol (blue) and pumpkin seed oil (red). The pumpkin seed oil was pumped through from the other side and pushed the Remazol out of the channel.

9.2.2. Mixer

The microfluidic mixing chip prior to filling is shown in figure 91.

.

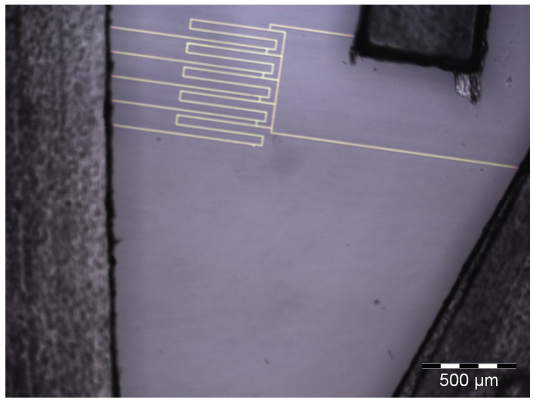

Figure 91: Possible mixing structure prior to filling. The access channels were made with scotch.

.

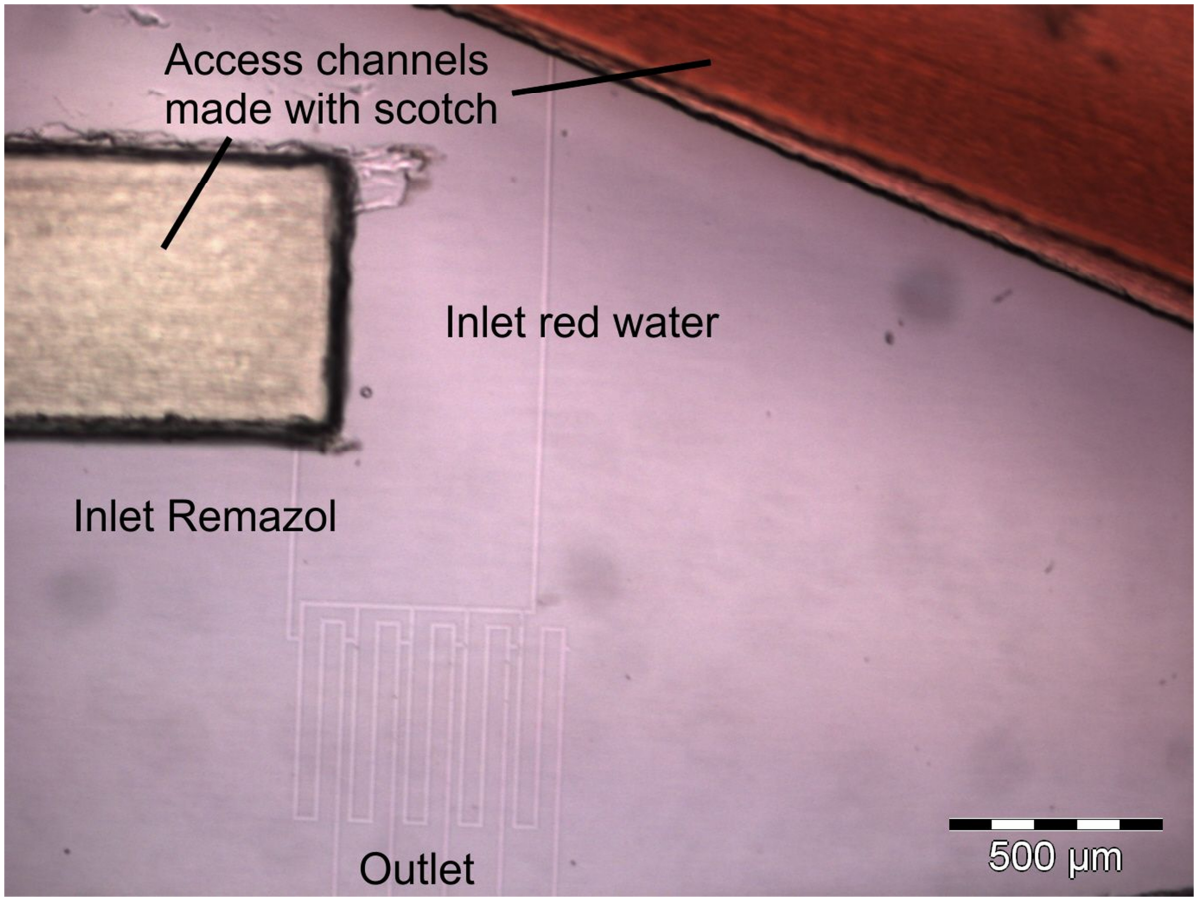

Figure 92: Mixing device filled with water dyed with Remazol and with red color ("Sissi Lebensmittelfarbe"). The red water can be seen in the access channels (height 100 µm) but it cannot be seen in the channels structured by the E-line (height 840 nm).

Figure 93 has been recorded using fluorescence microscopy. Remazol appears green, whereas the red dyed water can't be seen (black). The distance access channel - mixer is shorter at the left inlet (Remazol) than at the right inlet (red water). For that reason, if the same pressure is applied at both inlets, almost the whole chip is filled with Remazol. There is hardly any flow between the points 1) and 2) in the channel marked with a x, because the pressure difference between point 1) and 2) is too small to drive a significant flow through the channel. For the same reason there is almost hardly any flow through channel 3), i.e. the flow is too small to drive the Remazol out of the channel immediately. One can see a color change compared to the other channels at the outlet of the mixing channel (marked with "Mixing") indicating a mixing between fluorescent Remazol and red dyed water.

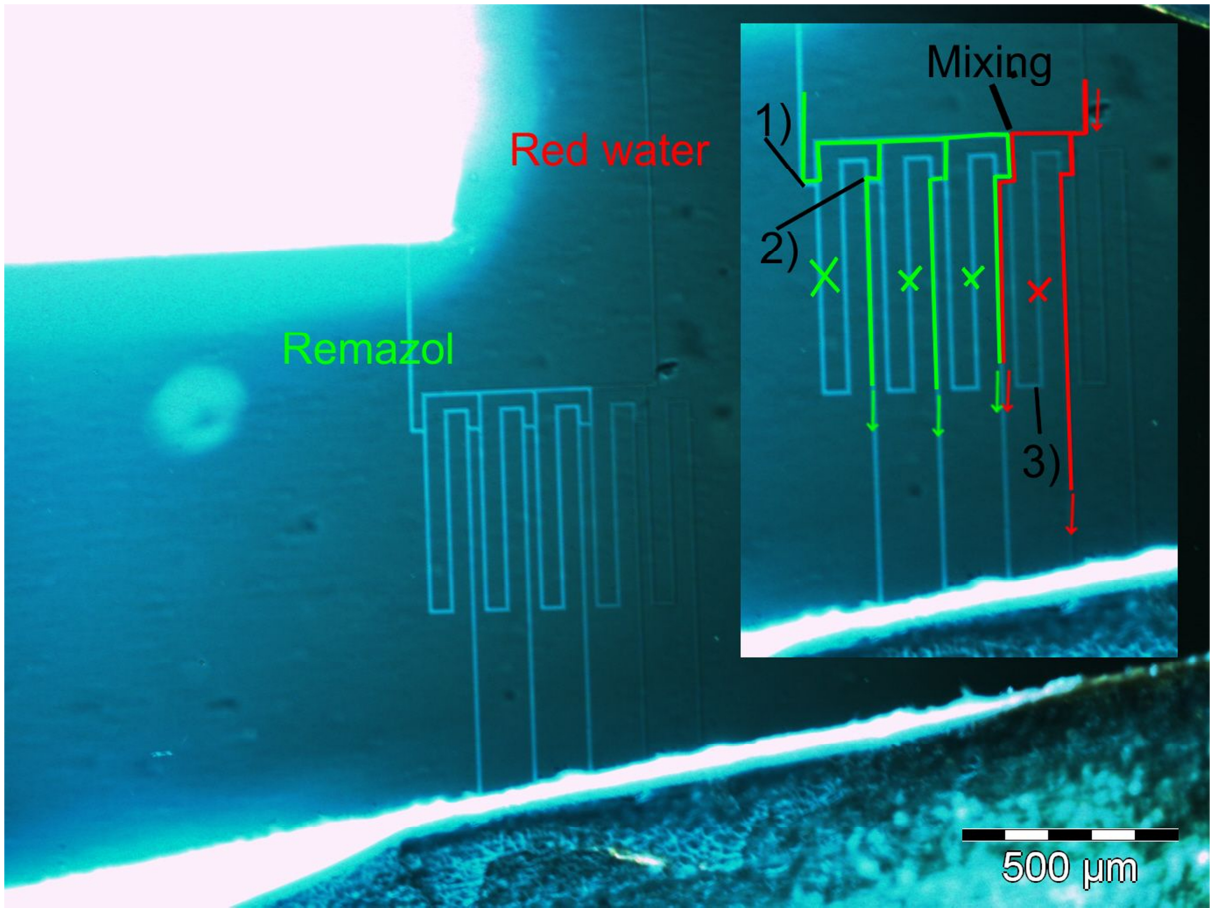

Figure 93: Mixing structure filled with Remazol and red water; the pressure at both inlets was approximately the same. The fluid flow is marked in the inset on the right; there is almost no flow between the points 1) and 2) in the channel marked with x. The pressure difference between point 1) and 2) is too small to drive a significant flow through the channel. A fluid flow through channel 3) is very small and not high enough to drive the Remazol out of the channel as on the right side. One can see a color change at the outlet of the mixing channel compared to the outlets of the other channels compared to the other channels indicating a mixing between fluorescent Remazol and the red dye.

The pressure at the red inlet was increased in order to see if the red water can be shifted to the left slowly pushing out the Remazol. The result is shown in figure 94. As expected, increasing the pressure at the inlet of the red water shifted the Remazol to the left. An interesting detail is marked in figure 94 with 1); the flow in this channel is very slow and one can actually see the red water advancing.

The goal was to fill all the channels with red water, but the PDMS bulk burst before that. This usually happens at pressures above 6 bar.

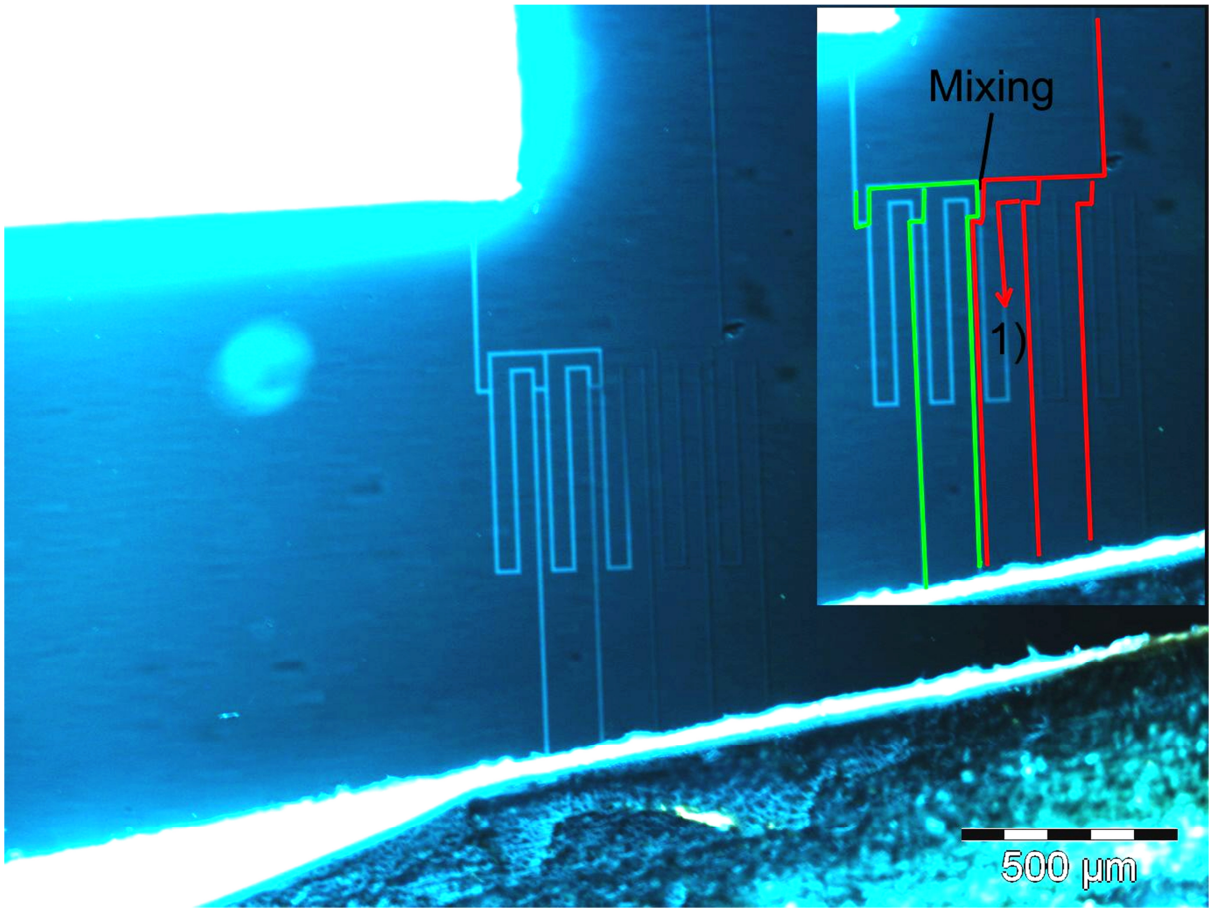

Figure 94: Mixing structure filled with Remazol and red water; the pressure at the inlet of the red water was higher than at the inlet of the Remazol. The fluid flow is marked in the inset on the right; and is basically the same as in figure 93. The difference is that the flow of the Remazol is shifted to the right as expected. The point marked with 1) shows the slowly advancing red water.

9.3. Conclusion – validation of function

It has been possible to pump liquid through inkjet structured as well as EBL structured microfluidic devices.

The channels of the inkjet structured microfluidic systems are very rough and their width varies on a long range (mm) as well as on a short range (µm) at the order of 30 µm. However, these rough channels are not influencing the laminar flow. Therefore, inkjet printing is suited for simple microfluidic systems. The functioning of such a simple system, a T-junction, has been validated. This T-junction was also used to create droplets and bubbles but the pressure required to pump viscous fluids like oil through the channels (160 µm x 20 µm cross-section) is too high to achieve a controlled and stable fluid flow. At high pressures, the elasticity of PDMS leads to mechanical oscillations and further to flow rates differing from the flow rate pumped into the system by the syringe pumps. Thus, viscous fluids would require wider and smoother channels with cross sections of 150 µm x 200 µm to reduce the pressure necessary for pumping.

A nano- / micro-fluidic reservoir as well as a mixer structured by EBL were fabricated. It was possible to pump liquid and oil through both systems. Their behavior was studied by fluorescence microscopy and their function was validated. Microfluidic systems structured by EBL have a high resolution and a typical cross section of 10 µm x 840 nm. These small channels require pressures higher than 1 bar to achieve a flow in the channels (0.2 µL/h). There are strong indications that these pressures deform the micro- / nano-fluidic channels leading to unknown flow rates and also unknown channel geometries. Hence, other pumping techniques which are not driven by external pressure should be preferred. Capillary- or electrophoretic- pumping could for example be used.

10. Conclusion

The fabrication procedure of microfluidic systems via replica molding using PDMS has been optimized. The masters were structured by electron beam lithography, inkjet printing and a combination of both. Furthermore, the principle function of the fabricated microfluidic devices was validated.

The major challenge of structuring microfluidic systems by EBL is that their lateral dimensions range from a few hundred nm up to tenths of µm making proximity corrections and resist profile simulations inevitable. Another issue is that these systems extend over a few mm requiring long exposure times and thus automatic drift compensations. Nevertheless, it has been shown that complex structures can be designed and exposed within two days providing a great amount of flexibility and at the same time a high resolution. As benchmarks, a reservoir, a possible droplet generator and a mixer were designed and fabricated successfully. Thus, it was shown that proximity correction, automatic drift compensation as well as controlled resist height adjustments through resist profile simulations are possible. Microfluidic systems were also structured by inkjet printing. Inkjet printing has the advantages of being fast and flexible. Furthermore, the height of the channels can be varied by printing multiple layers. However, the resolution and the accurateness of the printer is only sufficient for simple microfluidic applications. For that reason, the microfluidic systems were separated into the functional part and the periphery. The functional part was structured with a high resolution by the slower EBL whereas the periphery was structured with a low resolution by the faster inkjet printer. Thus, resources and writing time were reduced. The combination of these techniques requires an alignment between the inkjet printer and the EBL which has been done successfully.

The procedure to replicate structured masters by replica molding using PDMS had been optimized and it was possible to replicate structures with lateral dimensions of 500 nm. Subsequently, the replicas (molds) were bonded onto SiO_2 / glass substrates by stamp and stick or plasma activated bonding. The bonding strength of these techniques was examined by pressure tests. The plasma activated bonding yielded the strongest bonds on clean and smooth SiO_2 / glass substrates rendering it useful for high pressure applications (6 bar) in microfluidic channels with lateral dimensions in the sub µm regime. The stamp and stick bonding technique was used to seal electrodes and integrate sensitive SensFETs into microfluidic systems.

The principle function of the fabricated microfluidic devices has been validated. The T-junction device structured by inkjet printing has been used to mix dyed fluids and to generate droplets and plugs. However, the droplet / plug formation wasn't stable. Furthermore, a reservoir as well as a mixing device structured by EBL were studied by fluorescence microscopy. The fluid pumping was done by syringe pumps which were connected to the microfluidic devices by especially designed interconnects based on pressure assisted sealing with silicon soft tubes.

This master thesis is a foundation for future activities in the fields of microfluidic systems structured by EBL and inkjet printing, fabricated via replica molding using PDMS.

11. Bibliography

[1] D. C. Duffy, J. C. McDonald, O. J. A. Schueller, G. M. Whitesides, "Rapid Prototyping of Microfluidic Systems in Poly(dimethylsiloxane)", *Analytical Chemistry*, vol. 70, pp. 4974-4984, 1998.

[2] Y. Xia, G. M. Whitesides, "Soft Lithography", *Angewante Chemie International Edition*, vol. 37, pp. 550-575, 1998.

[3] N. T. Nguyen, S. T. Wereley, *Fundamentals and application of microfluidics*, ed. 2nd. Nordwod, London: Artech House, 2006, pp. 1-9.

[4] T. M. Squires, S. R. Quake, "Microfluidics: Fluid physics at the nanoliter scale", *Reviews of modern physics*, vol. 77, pp. 977-1026, 2005.

[5] S. Colin, *Microfluidics*. Hoboken, USA: Wiley, 2004, pp. 1-23.

[6] A. D. Strook, S. K. W. Dertinger, A. Ajdari, I. Mezic, H. A. Stone, "Chaotic Mixer for Microchannels", *Science*, vol. 295, pp. 647-650, 2002.

[7] N. T. Nguyen, S. T. Wereley, *Fundamentals and applications of microfluidics*, ed. 2nd. Nordwod, London: Artech House, 2006, pp. 11-54.

[8] L. Shui, J. C. T. Eijkel, A. v. d. Berg, "Multiphase flow in micro- and nanochannels", *Sensors and Actuators B*, vol. 121, pp. 263-276, 2007.

[9] J. Koo, C. Kleinstreuer, "Liquid flow in microchannels: experimental observations and computational analyses of microfluidic effects", *Journal of Micromechanical Microengineering*, vol. 13, pp. 568 - 579, 2003.

[10] H. E. Jeong, P. Kim, M. K. Kwak, C. H. Seo, K. Y. Suh, "Capillary kinetics of water in homogeneous hydrophilic polymeric micro- to nanochannels", *Small*, vol. 3, no. 5, pp. 778-782, 2007.

[11] J. H. Xu, S. W. Li, J. Tan, G. S. Luo, "Correlations of droplet formation in T-junction microfluidic devices: from squeezing to dripping", *Microfluid Nanofluid*, vol. 5, pp. 711-717, 2008.

[12] P. Garstecki, M. J. Fuerstman, H. A. Stone, G. M. Whitesides, "Formation of droplets and bubbles in a microfluidic T-junction scaling and mechanism of break up", *Lab on a Chip*, vol. 6, pp. 437-446, 2006.

[13] T. Fu, Y. Ma, D. Funfschilling, C. Zhu, H. Z. Li, "Squeezing to dripping transition for bubble formation in a microfluidic T-junction", *Chemical Engineering Science*, vol. 65, pp. 3739-3748,

2010.

[14] J. D. Tice, A. D. Lyon, R. F. Ismagilov, "Effects of viscosity on droplet formation and mixing in microfluidic channels", *Analytica Chemica Acta*, vol. 507, pp. 73-77, 2004.

[15] Raith support, "Technical description E-Line", Raith, Datasheet 2006.

[16] R. J. Hawryluk, "Exposure and development models used in electron beam lithography", *Journal of Vacuum Science and Technology*, vol. 19, no. 1, pp. 1-17, 1981.

[17] K. Vutova, E. Koleva, G. Mladenov, "Computer Simlation of Processes at Electron and Ion Beam Lithography, Part 1: Exposure Modeling at Electron and Ion Beam Lithography", in *Lithography*, M. Wang, Ed. Vukovar, Croatia: Intech, 2010, pp. 319-350.

[18] C. S. Wu, Y. Makiuchi, C. Chen, "High Energy Electron Beam Lithography for Nanoscale Fabrication", in *Lithography*, M. Wang, Ed. Vukovar, Croatia: Intech, 2010, ch. 13, pp. 257-283.

[19] K. Vutova, E. Koleva, G. Mladenov, "Computer Simlation of Processes at Electron and Ion Beam Lithography, Part 2: Simulation of Resist Developed Images at Electron and Ion Beam Lithography", in *Lithography*, M. Wang, Ed. Vukova, Croatia: Intech, 2010, pp. 351-378.

[20] S. A. Rishton, D. P. Kern, "Point exposure distribution measurements for proximity correction", *Journal of Vacuum Science and Technology B*, vol. 5, no. 1, pp. 135-141, 1987.

[21] M. G. Rosenfield, S. J. Wind, W. W. Molzen, P. D. Gerber, "Determination of proximity effect correction parameters for 0.1 µm electron beam lithography", *Microelectronic Engineering*, vol. 11, pp. 617-623, 1990.

[22] M. Parikh, D. F. Kyser, "Energy deposition functions in electron resist films on substrates", *Journal of Applied Physics*, vol. 50, no. 2, pp. 1104-1111, 1979.

[23] R. Wuest, C. Hunzikera, F. Robina, P. Strassera, D. Ernib, H. Jackela, "Limitations of Proximity-Effect Correction for Electron-Beam Patterning of Photonic Crystals", *Proc. of SPIE*, vol. 5277, pp. 186-197, 2004.

[24] I. Raptis, N. Glezos, E. Valamontes, E. Zervas, P. Argitis, "Electron beam lithography simulation for high resolution and high-density patterns", *Vacuum*, vol. 62, pp. 263-271, 2001.

[25] C. Dix, P. G. Flavin, P. Hendy, M. E. Jones, "0.1 µm scale lithography using a conventional electron beam system", *Journal of Vacuum Science and Technology B*, vol. 3, no. 1, pp. 131-135, 1985.

[26] L. Stevens, R. Jonckheere, E. Froyen, S. Decoutere, "Determination of the proximity parameters in electron beam lithography using doughnut-structures", *Microelectronic Engineering*, vol. 5, pp. 141-150, 1986.

[27] T. H. P Chang, "Proximity effect in electron beam lithography", *Journal of Vacuum Science and Technology*, vol. 12, no. 6, pp. 1271-1275, 1975.

[28] P. Hudek, D. Beyer, "Exposure optimization in high resolution e-beam lithography", *Microelectronic Engineering*, vol. 83, pp. 780-783, 2006.

[29] K. Keil, M. Hauptmann, K. H. Choi, J. Kretz, L. M. Eng, J. W. Bartha, "Fast backscattering parameter determination in e-beam lithography with a modified doughnut test", *Microelectronic Engineering*, vol. 86, no. 12, pp. 2408-2411 , 2009.

[30] S. Babin, I. Z. Kuzmin, "Experimental verification of the TEMPTATION temperature simulation ", *Journal of Vacuum Science and Technology B*, vol. 16, no. 6, pp. 3241-3247, 1998.

[31] G. Owen, "Methods for proximity effect correction in electron lithography", *Journal of Vacuum, Science and Technology B*, vol. 8, no. 6, pp. 1889-1892.

[32] G. P. Watson, L. A. Fetter, J. A. Liddle, "Dose modification proximity effect correction scheme with inherent forward scattering corrections", *Journal of Vacuum Science and Technology*, vol. 15, no. 6, pp. 2309-2312, 1997.

[33] A. A. S. Bhagat, P. Jothimuthu, I. Papautsky, "Photodefinable polydimethylsiloxane (PDMS) for rapid lab-on-a-chip prototyping", *Lab on a Chip*, vol. 7, pp. 1192-1197, 2007.

[34] H. Makamba, J. H. Kim, K. Lim, N. Park, "Surface modification of poly(dimethylsiloxane)", *Electrophoresis*, vol. 24, pp. 3607–3619, 2003.

[35] Swiss composite, "PDMS Sylgard 184 hochtransparentes RTV silicon", Swiss composite, Datasheet 2010.

[36] H. A. Biebuyck, N. B. Larsen, E. Delamarche, B. Michel, "Lithography beyond light: Microcontact printing with monolayer resists", *IBM Journal of Research and Development*, vol. 41, pp. 159-170, 1997.

[37] J. N. Lee, C. Park, G. M. Whitesides, "Solvent Compatibility of PDMS-Based Microfluidic Devices", *Analytical Chemistry*, vol. 75, pp. 6544-6554, 2003.

[38] G. Lisensky. (2008, July) University of Wisconsin - Cross-linking of Polydimethylsiloxane. [Online]. http://mrsec.wisc.edu/Edetc/nanolab/PDMS/PDMS.html

[39] H. Hillborg, U. W. Gedde, "Hydrophobicity Changes and Silicone Rubbers", *IEEE Transactions on Dielectrics and Electrical Insulation*, vol. 6, no. 5, pp. 1070-9878, 1999.

[40] J. K. Kallio, "PDMS and its Suitability for Analytical Microfluidic Devices", in *EMBS Annual International Conference*, New York City, 2006, pp. 2486-2489.

[41] J. A. Voorthuyzen, K. Keksin, P. Bergveld, "Investigations of the surface conductivity of silicon

dioxide and methods to reduce it", *Surface Science*, vol. 187, pp. 201-211, 1987.

[42] D. T. Eddington, W. C. Crone, D. J. Beebe, "Development of process protocols to fine tune PDMS material properties", in *7th International Conference on Miniaturized Chemical and Blochemlcal Analysts Systems*, Squaw Valley, Callifornia USA, October 5-9, 2003, pp. 1089-1092.

[43] D. Fuard, T. T. Chevolleau, S. Decossas , P. Tracqui, P. Schiavone, "Optimization of poly-di-methyl-siloxane (PDMS) substrates for studying cellular adhesion and motility", *Microelectronic Engineering*, vol. 85, pp. 1289–1293, 2008.

[44] A. Mata, A. J. Fleischman, S. Roy, "Characterization of Polydimethylsiloxane (PDMS) Properties for Biomedical Micro/Nanosystems", *Biomedical Microdevices*, vol. 7, no. 4, pp. 281–293, 2005.

[45] H. Schmid, B. Michael, "Siloxane Polymers for High-Resolution, High-Accuracy Soft Lithography", *Macromolecules*, vol. 33, pp. 3042-3049, 2000.

[46] D. Guo, S. J. Xiao, H. B. Liu, J. Chao, B. Xia, J. Wang, J. Pei, Y. Pan, Z. Z. Gu, X. Z. You, "Diffusion of Hydrosilanes from the Control Layer to the Vinylsilane-Rich Flow Membrane during the Fabrication of Microfluidic Chips", *Langmuir*, vol. 21, pp. 10487-10491, 2005.

[47] G. Caminoa, S. M. Lomakinb, M. Lazzaria, "Polydimethylsiloxane thermal degradation, Part 1. Kinetic aspects", *Polymer*, vol. 42, pp. 2395-2402, 2001.

[48] M. Liu, J. Sun, Q. Chen, "Influences of heating temperature on mechanical properties of PDMS", *Sensors and Actuators A* , vol. 151, pp. 42–45, 2009.

[49] K. C. Tang, E. Liao, W. L. Ong, J. D. S. Wong, A. Agarwal, R. Nagarajan, "Evaluation of bonding between oxygen plasma treated polydimethyl siloxane and passivated silicon", *Journal of Physics: Conference series*, vol. 34, pp. 155-161, 2006.

[50] H. Hillborg, J. F. Ankner, U. W. Gedde, G. D. Smith, H. K. Yasuda, K. Wikström, "Crosslinked polydimethylsiloxane exposed to oxygen plasma studied by neutron reflectometry and other surface specific techniques", *Polymer*, vol. 41, pp. 6851-6863, 2000.

[51] J. Kim, M. K. Chaudhury, M. J. Owen, T. Orbeck, "The Mechanisms of Hydrophobic Recovery of Polydimethylsiloxane elastomeres exposed to partial electrical discharges", *Journal of Colloid and Interface Science*, vol. 244, pp. 200–207, 2001.

[52] J. C. Mcdonald, G. M. Whitesides, "Poly(dimethylsiloxane) as a material for fabricating microfluidic devices", *Accounts of Chemical Research*, vol. 35, no. 7, pp. 491-499, 2002.

[53] A. Y. N. Hui, G. Wang, B. Lin, W. T. Chan, "Microwave plasma treatment of polymer surface for irreversible sealing of microfluidic devices", *Lab on a Chip*, vol. 5, pp. 1173-1177, 2005.

[54] B. Millare, M. Thomas, A. Ferreira, H. Xu, M. Holesinger, V. I. Vullev, "Dependence of the Quality of Adhesion between Poly(dimmethylsiloxane) and Glass surface on the Conditions of

Treatment with Oxygen Plasma", *Langmuir*, vol. 24, no. 22, pp. 12218-13224, 2008.

[55] S. Bhattacharya, A. Datta, J. M. Berg, S. Gangopadhyay, "Studies on Surface Wettability of PDMS and glass under oxygen plasma treatement and correlation with bond strength", *Journal of Microelectromechanical Systems*, vol. 14, no. 3, pp. 590-597, 2005.

[56] M. Morra, E. Occhiello, R. Marola, F. Garbassi, P. Humphrey, D. Johnson, "On the aging of oxygen plasma-treated PDMS surfaces", *Journal of Colloid and Interface Science*, vol. 137, no. 1, pp. 11-24, 1989.

[57] E. Delamarche, H. Schmid, B. Michel, "Stability of Molded Polydimethylsiloxane", *Advanced Materials*, vol. 9, no. 9, pp. 741-746, 1997.

[58] N. Koo, U. Plachetka, M. Otto, J. Bolten, "The fabrication of a flexible mold for high resolution soft ultraviolet nanoimprint lithography", *Nanotechnology*, vol. 19, p. 225304, 2008.

[59] X. Yu, D. Zhang, T. Li, L. Hao, X. Li, "3-D microarrays biochip for DNA amplification in PDMS elastomer", *Sensors and Actuators A*, vol. 108, pp. 103-107, 2003.

[60] B. H. Jo, L. M. Van Lerberghe, K. M. Motsegood, D. J. Beebe, "Three-Dimensional Micro Channel Fabrication in PDMS elastomer", *Journal of Microelectromechanical Systems*, vol. 9, no. 1, pp. 76-81, 2000.

[61] A. M. Christensen, D. A. Chang-Yen, B. K. Gale, "Characterization of interconnects used in PDMS microfluidic systems", *Journal of Micromechanic and Microengeneering*, vol. 15, pp. 928–934, 2005.

[62] J. C. McDonald, J. R. Anderson, D. T. Chiu, H. Wu, G. M. Whitesides, "Fabrication of microfluidic systems in poly(dimethylsiloxane)", *Electrophoresis*, vol. 21, no. 1, pp. 27-40, 2000.

[63] H. Wu, B. Huang, R. N. Zare, "Construction of microlfuidic chips using PDMs for adhesive bonding", *Lab on a chip*, vol. 5, pp. 1393-1398, 2005.

[64] S. Stayanarayana, R. N. Karnik, A. Majumdar, "Stamp and Stick room temperature bonding technique for microdevices", *Journal of Microelectromechanical Systems*, vol. 14, no. 2, pp. 392-399, 2005.

[65] B. Samel, M. K. Chowdhury, G. Stemme, "The fabrication of microfluidic structures by means of full wafer adhesive bonding using PDMS catalyst", *Journal of Micromechanic and Microengeneering*, vol. 17, pp. 1710-1714, 2007.

[66] J. S. Go, S. Shoji, "A disposable, dead volume-free and leak-free in-plane PDMS microvalve", *Sensors and Actuators A: Physical*, vol. 114, no. 2-3, pp. 438-444, 2004.

[67] S. Takeda, M. Fukawa, Y. Hayashi, K. Matsumoto, "Surface OH group governing adsorption

properties of metal oxide films", *Thin Solid Films*, vol. 339, pp. 220-224, 1999.

[68] A. Klug, K. Schmoltner, E. J. W. List, "Organic field-effect transistors applicable for gas and ion detection", in *Organic Semiconductors in Sensors and Bioelectronics III*, vol. 7779, San Diego, California, USA, 2010.

[69] M. A. Eddings, M. A. Johnson, B. K. Gale, "Determining the optimal PDMS-PDMS bonding technique for microfluidic devices", *Journal of Micromechanic and Microengeneering*, vol. 18, 2008.

[70] R. Lo, E. Meng, "Integrated and reusable in-plane microfluidic interconnects", *Sensors and Actuators B*, vol. 132, pp. 531-539, 2008.

[71] C. K. Fredrickson, Z. H. Fan, "Macro-to-micro interfaces for microfluidic devices", *Lab on a Chip*, vol. 4, pp. 526-533, 2004.

[72] A. A. S. Bhagat, P. Jothimuthu, A. Pais, O. Papautsky, "Re-usable quick release interconnect for characterization of microfluidic systems", *Journal of Micromechanic and Microengineering*, vol. 17, pp. 42-49, 2007.

[73] D. Sabourin, D. Snakenborg, M. Dufva, "Interconnection block: a method for providing reusable, rapid, multiple, aligned and planar microfluidic interconnections", *Journal of Micromechanic and Microengineering*, vol. 19, p. 035021, 2009.

[74] D. Snakenborg, G. Perozziello, O. Geschke, J. P. Kutter, "A fast and reliable way to establish fluidic connections to planar microchips", *Journal of Micromechanic and Microengeneering*, vol. 17, pp. 98-103, 2007.

[75] R. P. Schmitz, M. W. Tausch. (2011, Feb.) Chemie interaktiv. [Online]. http://www.chemie-interaktiv.net/ff.htm#

[76] D. Drouin, A. R. Couture, D. Joly, "Casino V2.42- A fast and easy to use modeling tool for scanning electron microscopy and microanalysis users", *Scanning*, vol. 29, pp. 92-101, 2007.

[77] T. A. Fretwell, R. Gurung, P. L. Jones, "Curve fitting to Monte Calro data for the determination of the proximity effect correction parameters", *Microelectronic Engineering*, vol. 17, pp. 389-394, 1992.

Appendix

I) Electron interaction – simulations

It is very important to get insight of the interaction between the resist, the substrate and the electrons. There is a Monte Carlo based simulation software called CASINO (Version 2.42) used to simulate these interactions. The results of this software are known to agree with experimental results. [**76**]

The parameters used for all following simulations are:

- Number of electrons 100 000
- Total cross section: Mott by interpolation
- Partial cross section: Mott by interpolation
- Effective section ionization: Casnati
- Ionization Potential: Joy and Luo
- Random number generator: Press et al. [1986]
- Directin Cosin: Soum et al.
- dE/dS: Joy and Luo
- Energy absorption graphs: X Division = Y Division = Z Divisions = 400 (The program will crash if the number of divisions are increased)
- Distributions graphs: Divisions = 1000

A typical system in electron beam lithography consists of a resist layer on top of a substrate. There are two interesting topics, which will be examined by CASINO. One is the behavior of backscattered electrons from a Si substrate. The other one is the energy deposition in a representative two layer system consisting of a Si substrate covered with 800 nm PMMA resist. Please note that since the structure of our Novolac resist isn't known, PMMA was used as a dummy. The principle behavior, however, is believed to be the same.

I) 1. Backscattered electrons – Si substrate

The CASINO software provides information about surface backscattered electrons (backscattered electrons emerging from the surface) through two relevant distributions:

- The total energy of surface backscattered electrons in a length division as a function of radial distance from the incident beam (see figure 95 on the left)
- The total number of surface backscattered electrons in a length division as function of radial distance from the incident beam (see figure 95 on the right)

The radial distance is divided into divisions. The number of divisions has to be fixed prior to the simulation. Therefore, the resolution depends on the maximal radial distance of an emerging surface backscattered electron encountered during the simulation divided by the number of divisions. The

backscattered electrons can travel further at high acceleration voltages. Consequently the resolution is decreased at high acceleration voltages.

The simulation results are shown in figure 95.

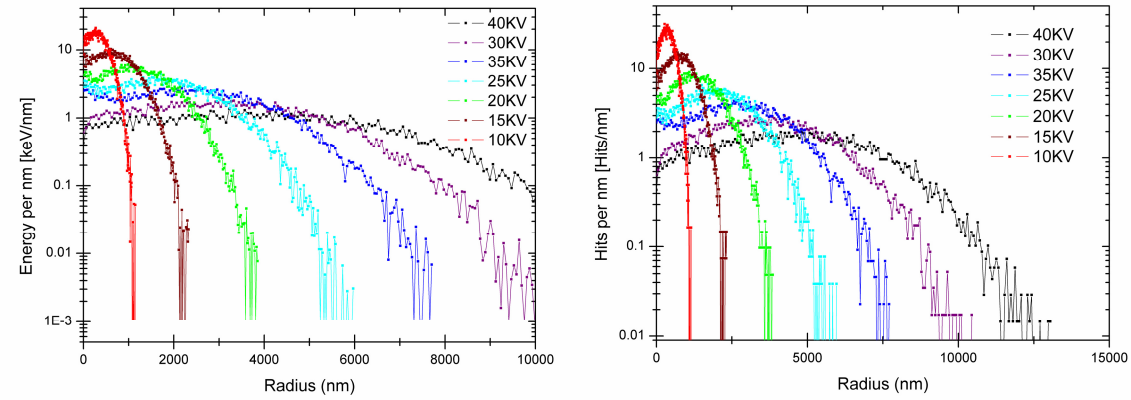

Figure 95: Left: Total energy of surface backscattered electrons as a function of radial distance from the incident beam. Right: Total number of surface backscattered electrons as a function of radial distance from the incident beam.

In figure 95 one can see that the total energy distribution of the surface BE's is narrower and higher for lower acceleration voltages than for high ones. The consequence is, that for low acceleration voltage the total energy of backscattered electrons is limited to short ranges around the incident beam where it has a high and well defined maximum. At high acceleration, the total energy of the backscattered electrons has a long range, but the maximum is not as well defined and always lower than at low acceleration voltages. As a consequence, high acceleration voltages should be preferred; the forwardscattering will be smaller and at the same time the total energy of the increasingly long range BE's could be chosen to be underneath the critical dose.

Please note: The high variance at large radial distance is due to a lack of statistic: Few BE electrons travel that far leading to „oscillations" at large radial distances.

I) 2. Energy deposition – PMMA on Si

The CASINO software provides an "energy by position tool". This feature records, in a three-dimensional matrix of cubic elements, the amount of energy lost in such a cubic element by all the simulated electron trajectories. The size of these cubic elements is again determined by the number of divisions and the maximum range of the electron trajectories. For that reason, all the following graphs are corrected by dividing the simulated data by the division size. A typical energy by position distribution is shown in figure 96.

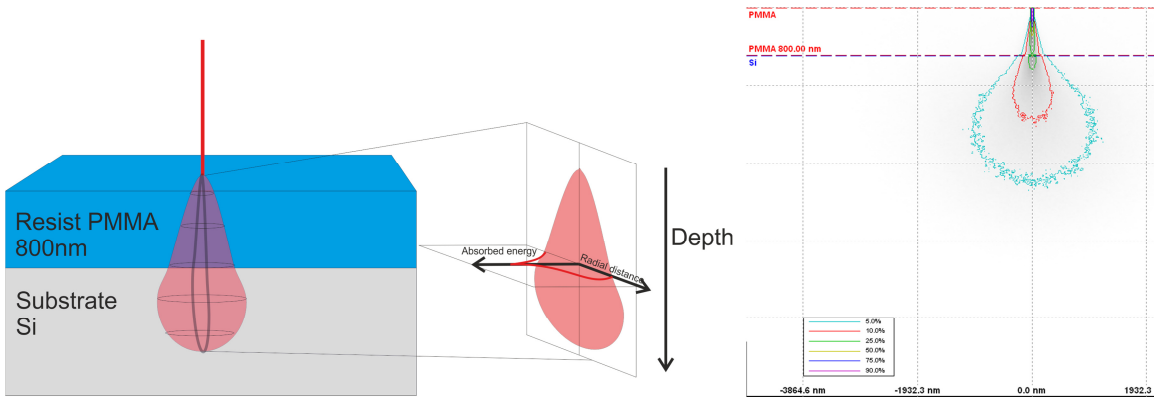

Figure 96: Left; energy deposition distribution; due to spherical symmetry it is possible to only look at the XZ plane. It is convenient to talk about the radial distance from the incident beam and the depth only. Right; energy by position of the XZ plane where y =0 (center of the incident beam). Area not enclosed by colored lines corresponds to the energy which is not adsorbed in the surrounded area. I.e. the area enclosed by the 10 % line adsorbs 90 % of the energy. Note that the energy was summed over the projected axis.

The interaction volume of the beam is spherically symmetric. It is therefore sufficient to look at the energy deposition in one plane XZ cutting the center of the incident beam (The plane XZ where Y=0). It is convenient to talk about the radial distance r from the incident beam and the depth z in the substrate. The following interesting topics can be extracted:

- Energy deposition as a function of r and z for a certain acceleration voltage.
- The energy deposition as a function of radial distance for different acceleration voltages and for different depths in the substrate.
- The energy deposition as a function of the depth z of different acceleration voltages, in the center of the beam (r = 0) as well as away from the beam r = 50 nm.

The overview of the energy deposition for different acceleration voltage is shown figure 97 and figure 98.

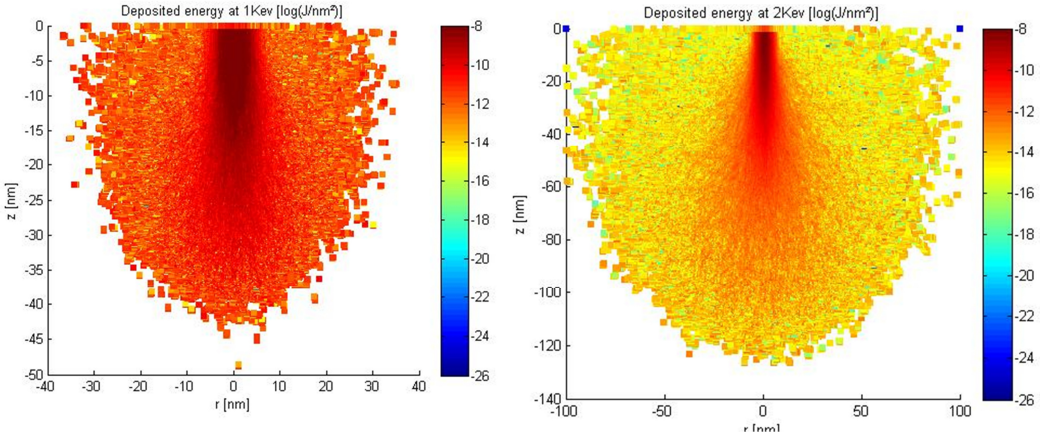

Figure 97: Left; deposited energy at 1 kV acceleration voltage. Right; deposited energy at 2 kV deposited energy.

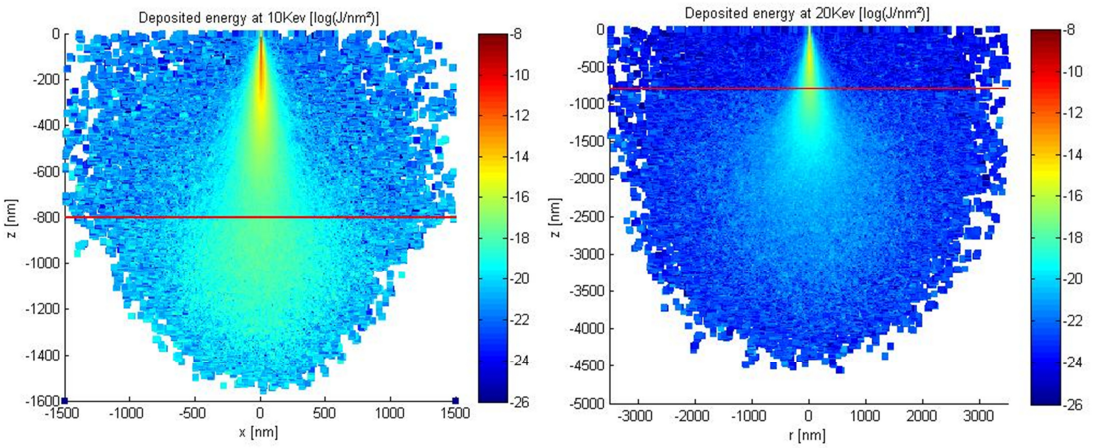

Figure 98: Left; deposited energy at 10 kV deposited energy. The red line indicates the resist– substrate interface. Right; deposited energy at 20 kV deposited energy red line indicates the resist– substrate interface.

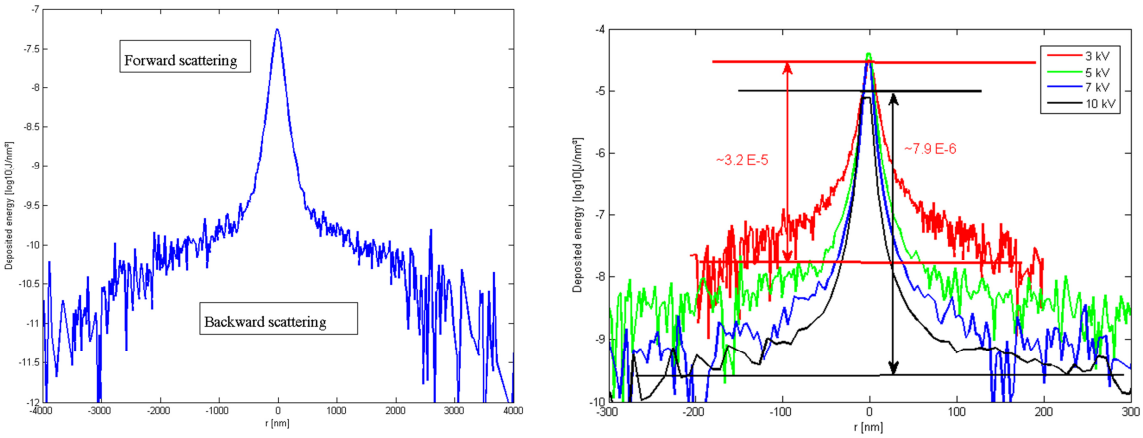

Figure 99: Left; deposited energy as a function of radial distance from the incident beam at a depth of 800 nm at an acceleration voltage of 20 kV. This function has the typical shape of two Gaussians, see chapter 3, on page 25 for details. Right; deposited energy as a function of radial distance from the incident beam at a depth of 50 nm at acceleration voltages: 3 kV, 5 kV, 7 kV and 10 kV.

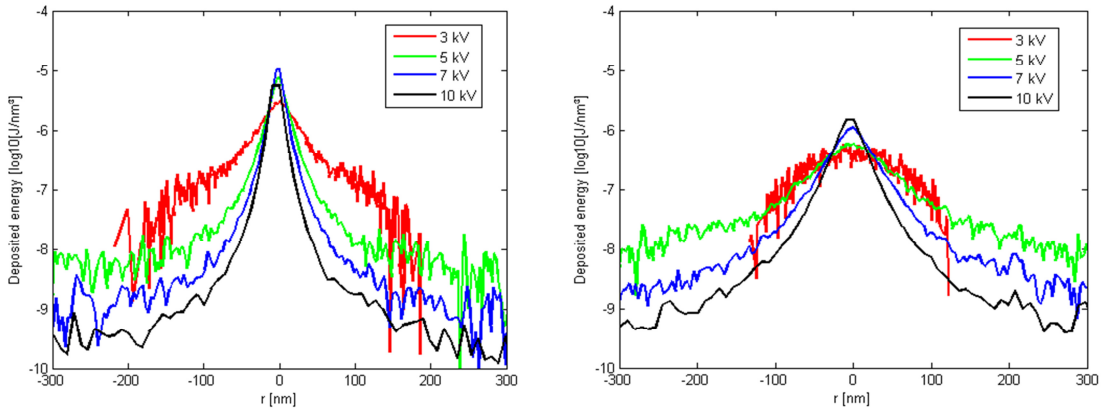

Figure 100: Left; deposited energy as a function of radial distance from the incident beam at a depth of 100 nm. Acceleration voltages: 3 kV, 5 kV, 7 kV and 10 kV. Right; deposited energy as a function of radial distance from the incident beam at a depth of 200 nm at acceleration voltages: 3 KV, 5 KV, 7 kV and 10 kV.

Figure 99 and figure 100 show the deposited energy as a function of radial distance at acceleration voltages of 3,5,7 and 10 kV at a depth z of 50 nm, 100 nm and 200 nm. The backscattered energy deposition for 10 kV has a longer range than at 3kV. But the deposited energy of these backscattered electrons is much lower at high acceleration voltages such as 10 kV than at 3 kV. The difference between the deposited energy of forwardscattered electrons to backward scattered electrons at 3 kV is 4 times lower than at 10 kV. I.e. the backward scattered electrons deposit 4 times more energy in the resist at 3 kV compared to 10 kV. Another interesting fact which can be seen is that the forwardscattered contribution to the deposited energy decreases as expected with increasing depth. The deposited energy at 3 kV at a depth of 200 nm can‘t be separated into backscattered and forwardscattered anymore.

Figure 101 shows the deposited energy as a function of depth for different acceleration voltages and radial distances r. Let’s consider the radial distance r = 0: The deposited energy is practically constant until a certain depth where it starts to decrease rapidly (note the logarithmic scale). As expected, high acceleration voltages penetrate deeper into the material than lower ones. An interesting detail of this simulation is that the deposited energy is slightly increased around the interface resist-substrate.

If the deposited energy as a function of depth is plotted at a radial distance of r ≠ 0 as in figure 101 one can see that the deposited energy of high acceleration voltages like 40 kV is a magnitude lower than at 10 kV, for example. An interesting detail is that the deposited energy has a maximum when crossing the main belly of the „interaction pulp“ as shown in figure 102 on the right.

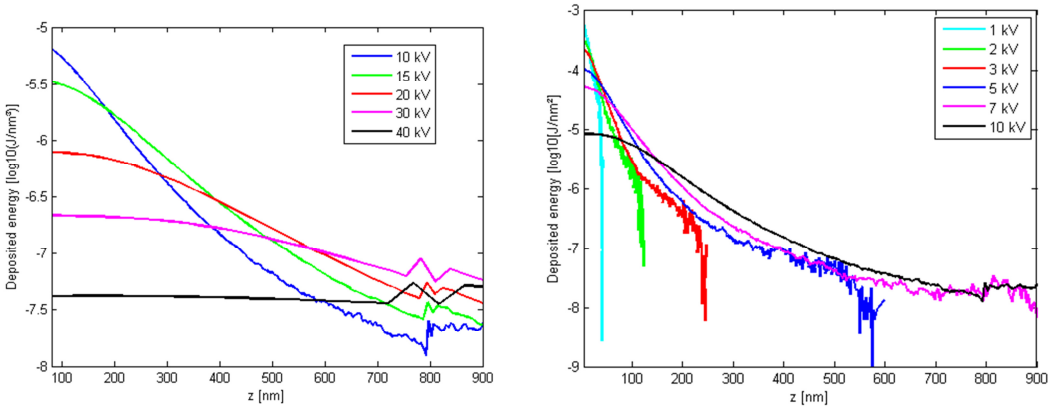

Figure 101: Left; deposited energy as a function of depth in the center of the incident beam at r = 0. Acceleration voltages: 10 kV, 20 kV, 25 kV, 30 kV, 40 kV. The interface resist-substrate is at z=800nm. Right; deposited energy as a function of depth in the center of the incident beam at r = 0. Acceleration voltages: 1 kV, 2 kV, 3 kV, 5 kV, 7 kV, 10 kV. The interface resist-substrate is at z=800 nm.

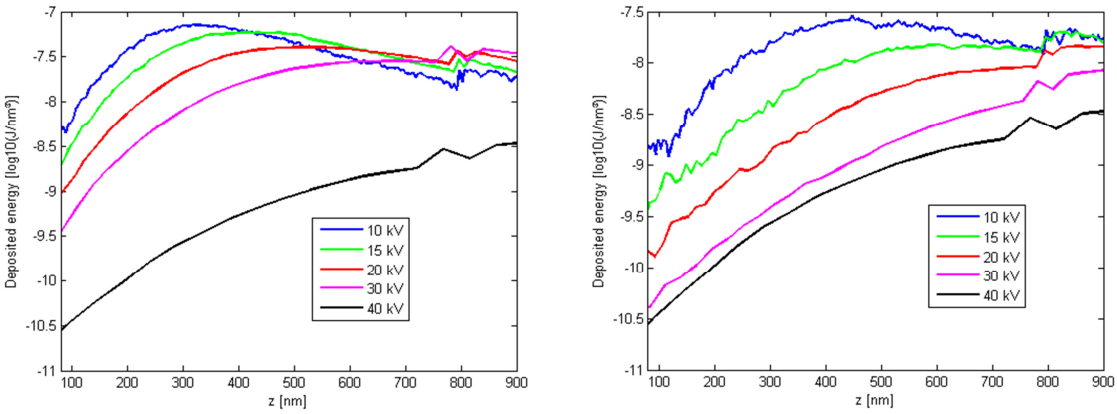

Figure 102: Left; deposited energy as a function of depth in the center of the incident beam at r = 50 nm. Acceleration voltages: 10 kV, 15 kV, 20 kV, 25 kV, 30 kV and 40 kV. The interface resist-substrate is at z=800 nm. Right; deposited energy as a function of depth in the center of the incident beam at r = 100 nm. Acceleration voltages: 10 kV, 15 kV, 20 kV, 25 kV, 30 kV and 40 kV. The interface resist-substrate is at z=800 nm.

I) 3. Conclusion - simulation

As a résumé one can say, that an increasing acceleration voltage also leads to an increasing interaction volume. The point is, that the actual deposited energy in this interaction volume is decreased with increasing acceleration voltage, i.e. the difference between the deposited energy around the incident beam and the deposited energy of the long ranging backscattered electrons, is higher at high acceleration voltages. The long ranging interaction of the backscattered electrons can usually be cut off with the contrast of the resist. Low acceleration voltages require a very high contrast in order to achieve a good resolution since the energy window between the desired deposited energy around the incident beam and the undesired energy deposited further away from it is small compared to high acceleration voltages. Another problem arising when using low acceleration voltages is that the beam gets stuck in the resist not developing it all the way through down to the substrate.

As far as the proximity function parameters are concerned one can draw the following conclusions (in agreement with reference [**22**] (simulations) and reference [**25**] (experimental results)):

Acceleration voltage is ...	then α ...	then β ...	then η
increasing	decreases	increases	decreases
decreasing	Increases	decreases	increases

II) PDMS

II) 1. PDMS datasheet / PDMS mechanical properties

Property	Value
Viscosity Base	5500 mPas
liquid PDMS after mixing (1:10 weight ratio curing agent:base)	4000 mPas [**35**], 4150 mPas [**44**]
Time after which viscosity of the liquid PDMS doubled at 25°C ambient temperature. Corresponds to the processing time.	2 h
Time after which viscosity of the liquid PDMS doubled at -7°C ambient temperature.	20 h
Specific weight at 25°C	1.05
Tensile strength	6.3 MPa
Elongation	100% [**35**],
Thermal expansion.	$9.6\ 10^{-4}$ /K
Heat conductivity	0.15 W/(m K)
Curing processes	15 min 150 °C; 1 h 100 °C; 4 h 65 °C; 24 h 25 °C;
The mechanical and electrical properties change for	7 days
Breake through voltage	22 KV/mm
Refraction index	1.430 [**35**], [**44**]
Specific resistance	$1\ 10^{15}$ Ohm/cm
Young modulus	1.75 MPa up to 45% strain [**44**]

II) 2. PDMS pre-polymer fabrication

An overview of the PDMS fabrication process is given in figure 103. In order to prepare the liquid PDMS, the equipment should be arranged first: One needs two spoons, one Pasteur pipette, a baker and aluminum foil. The baker and the spoon should be cleaned thoroughly. The base has a viscosity similar to honey, that's why the spoon used to transfer the PDMS-Base to the baker has to be twisted all the time in order to avoid spilling. After the base is transferred it is weighted, the weight is noted and then set to 0. After that the curing agent (ratio 1 : 10 curing agent : base) is added to the baker simply by using a Pasteur pipette. After each drop one has to wait a few seconds for the wage to be ready.

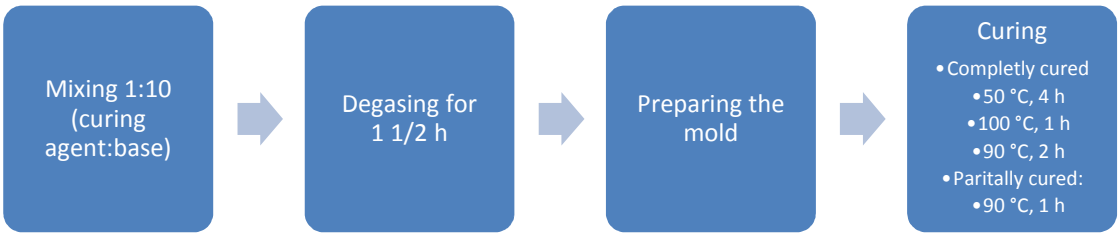

Figure 103: PDMS pre-polymer fabrication

Please note that putting the curing agent into another baker and mixing the base and the curing agent later is not as exact since there is always some residual curing agent staying inside. It is therefore better to add the curing agent directly to the base in the baker.

After the weighting the mixture is stirred for 2 minutes. Then the PDMS is put into a vacuum chamber for 1 ½ h at about 100 mbar in order to extract all air bubbles. The vacuum chamber is vented from time to time in order to pop air bubbles.

III) Surface OH groups

The OH groups always present on metal oxide films and SiO_2 are believed to play an important role in the surface properties of the films. The materials investigated in were SiO_2, SnO_2, TiO_2, CrO_x, ZrO_2. [**67**]

The surface OH group density depends on the electro negativity difference between the oxygen and the metal element. The higher the electro negativity of the metal compared to the oxygen, the higher the OH density on the surface. [**64**]

The OH groups on the surface adsorb organic substances. The more OH groups the more organic substances get adsorbed. The contact angle of DI water of these materials is 0° right after deposition but it increases as the organic substance get adsorbed. The contact angle saturates after a certain time. Materials with a high surface OH group density like CrO_2 end up having a contact angle of 90° whereas SiO_2 with a low OH group density ends up having a contact angle around 40°. [**67**]

It is believed that plasma activation cleans the surface liberating the OH groups which are important for bonding. [**1**] Please note that cleaning the samples by rinsing them with acetone, isopropanol and ultra-sonic bath does not liberate the surface OH groups because the contact angle isn't changed.

IV) Peel Test

The peel test is performed in order to quantify the bonding quality. The peel test is basically done by peeling off the PDMS stamp bonded to the substrate. The bonding quality is then defined as the ratio between the reversible bonded areas to the irreversible bonded areas as shown in figure 104. This method is purely empirical but it is fast, uncomplicated and meets the requirements.

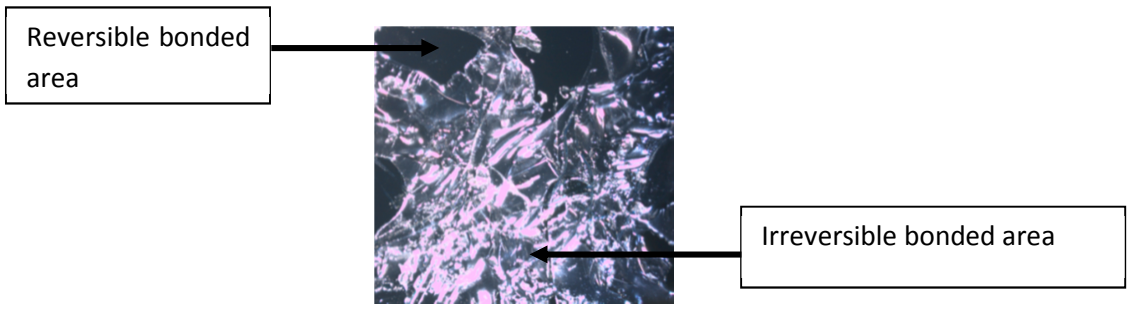

Figure 104: Peel test example: PDMS bonded to a SiO2 substrate both plasma activated. Reversible bonded and irreversible bonded areas are marked by arrows.

It's important to know that the bonding quality is somehow stochastic and also depends on other parameters like the substrate treatment prior to plasma activation and how the PDMS sample has been placed on to the substrate. These random effects are believed to be included by determining

the variance of the bonding quality, i.e. by doing statistics. In order to bond microfluidic chips reliably, the mean bonding quality has to be good and the variance of this bonding quality has to be small.

The quality and the variance of the bonding were determined by the following equations:

$$q_i = \frac{A_i^{reversible}}{A_i}$$

$$Q = \frac{\sum_i q_i k_i}{\sum_i k_i}$$

$$\sigma = \sqrt{\frac{\sum_i (q_i - Q)^2 k_i}{\sum_i k_i}}$$

q_i... quality factor sample i; $A_{R,i}$ ... reversible bonded area of sample A_i... total area of sample i; Q... mean quality of all activated with the same plasma parameter (pressure, power, time); k_i corresponds to the statistical weight of sample i, which was chosen to be the total area of the sample ($A_i = k_i$)). σ... Variance of the mean Q.

V) Pressure test

The pressure test is used to quantify the bonding strength. This is done by applying a pressure onto a reservoir until this reservoir bursts. This reservoir has to have the same size and geometry for all samples in order to compare the results. Varying geometries lead to different results. [**64**] A typical setup is shown in figure 105.

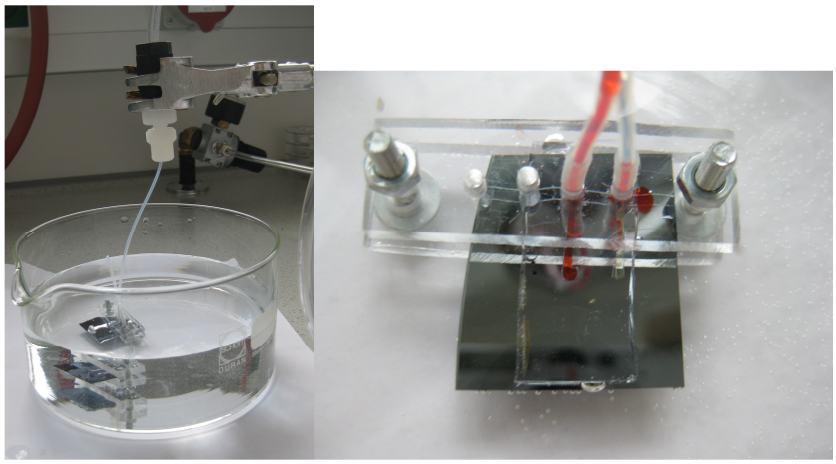

Figure 105: Pressure test setup. The channel is filled with red water and subsequently connected to the pressure supply. The pressure is increased until the chip starts to burst / leak.

The master used to fabricate these microfluidic chips is shown in figure 106. The master was made out of scotch. Consequently, the reservoirs were not very well defined. This will lead to an error which is believed to be important, but no other test structure was available at the time.

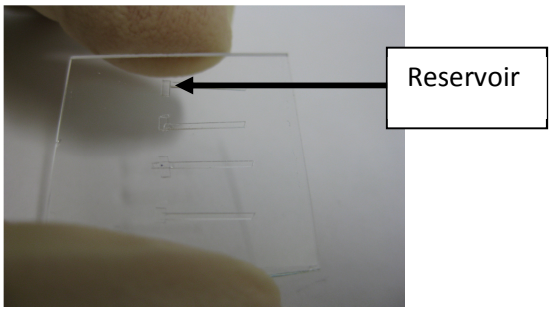

Figure 106: Master made out of scotch used to make the pressure tests. The reservoirs are not very well defined and their sizes vary.

The pressure test is conducted as follows. First, the channels are filled with water to be sure that the pressure is actually applied to the reservoir and that there are no leaks. The air in the channel in front of the water can simply be squeezed out because the PDMS is air permeable. Once the water has filled the reservoir, the pressure is increased until the chip starts to leak / bursts. The burst / the leaking should be happening around the reservoir first. Leaking at another place leads to useless results.

VI) Contact angle measurements

The goal of the contact angle measurements was to determine the density of OH groups as a function of time after plasma activation of SiO_2, glass and PDMS.

The contact angles were measured with DI (deionized) Water in sessile droplet mode. The droplet volumes were 1 µL and the droplets were measured within 1 min after deposition. Only advancing contact angles were measured. In order to determine the contact angle "automatic fitting" was used. For further details please refer to the user manual.

The PDMS stamps were produced with the standard procedure „simple PDMS molds" and they were cured at 100 °C for 1 h and put on a glass sheet. The samples were subsequently activated by the standard procedure (evacuate to 0,3 mbar, flush for 15 minutes at 0,6 mbar with oxygen).

VII) Doughnut test

First of all, the fabrication of the doughnut test will be explained. The evaluation and parameter determination (fitting) will be discussed subsequently.

11.1.1. Fabrication

A doughnut test was designed with a tool called Raith Doughnut test. The parameter space was divided into 2 regimes. The upper regime consisted of doughnuts with large inner radius and high doses, whereas the lower regime consisted of doughnuts with small inner radius and lower doses. The step size of the inner radius R1 of the upper regime was higher than of the lower regime. This is because the doughnut test is more sensible in the lower regime around the forwardscattering parameter.

The exposure parameters are listed in the following:

Upper regime:

- Normalized dose: from: 0.5 to 2 step 0.05
- Inner radius R1: from 1 µm to 3.5 µm; step 0.03 mu
- Outer radius R2: 11.6 µm
- In order to save time the parameter space was further constraint by deleting doughnuts at edges.

Lower regime:

- Dose: from: 0.5 to: 0.09 step: 0.01
- Inner radius R1: from: 2 µm to: 0.01 µm step: 0.01 µm
- Outer radius R2: 11.6 µm
- In order to save time the parameter space was further constraint by deleting doughnuts at edges.

This doughnut test was exposed with the following parameters:

- Base dose = 100 µC/cm²
- Area step size 0.0096 µm
- Acceleration voltage 20 KV
- Aperture = 10 µm
- Developer 2 min, developer:water ratio 4:1

The writing time lasts more than one day. Carefully constraining the parameter space by deleting doughnuts at the edges is therefore necessary. The resulting structure is shown in figure 107.

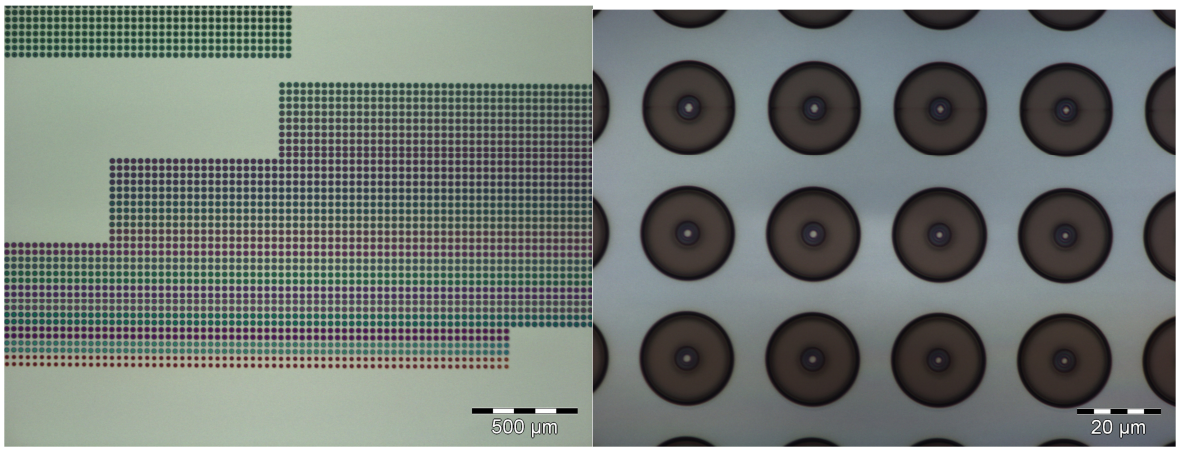

Figure 107: Images are made with the optical microscope of the doughnut test. Left; cut-out of the Doughnut test (lower regime). The parameter space was constraint by deleting away the edges in order to save writing time. Right; close up of the doughnuts

First the contrast curve which has been exposed at the same time as the doughnut test is presented. The evaluation of the doughnut test can be rather time consuming and will be explained first. The extraction of the proximity parameters is then done via a non-linear least square fit in the end.

11.1.2. Evaluation

The evaluation of the doughnut test is best done with the SEM using the SE-Inlens detector and low acceleration voltages (10 kV for example). The SE-Inlens detector has a slight material contrast (e.g. one can distinguish between organic substances and SiO_2) and the SEM has a high resolution. The secondary electrons emission depth is around 10 nm to 20 nm. [**29**] Another advantage of this method is that if the contrast curve was exposed on the same substrate the critical deposited dose D_c can be determined by looking at the contrast curve. The dose where the last contrast pattern is still visible with the SEM corresponds to D_c. D_c can then be used to identify the open / closed doughnuts and can further be used to fit the proximity parameters later on.

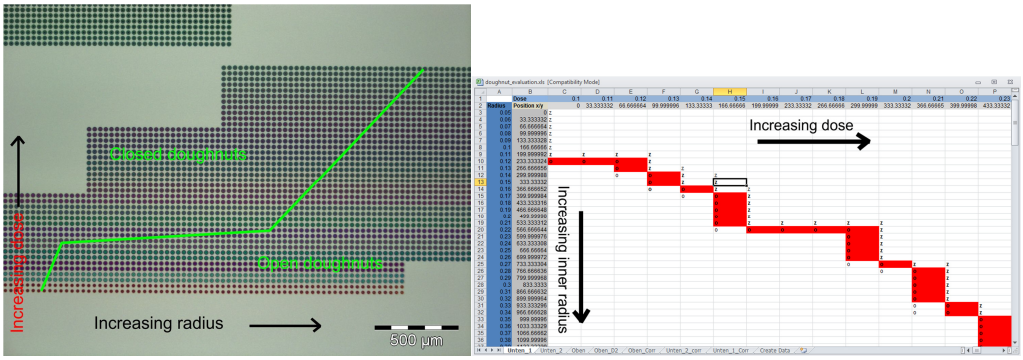

Figure 108: Left; evaluation of the doughnut test; the imaginary line between the closed and open doughnuts is followed. Right; doughnut-test evaluation in an Excel sheet. The data points are marked red. The absolute position of the data points was then automatically calculated by a macro.

The evaluation is done by setting the origin of the local coordinate system into the center of the first doughnut (lowest dose, smallest inner radius). After that, the doughnuts exposed at the lowest dose are scanned along an increasing radius (along the first lower line) up to the point where the first doughnut is opened, i.e. the center of the doughnut is free of resist. The coordinates of this doughnut are marked. The line between the just opened doughnuts and just closed doughnuts is followed. It's faster to mark the path of this line. The coordinates of the just opened doughnuts should nevertheless be marked down every once in a while.

These coordinates and the path are then written into an excel sheet which automatically transforms the path into the absolute values of the inner radius and the dose. Once the absolute inner radius and the dose is known, it is time to determine the proximity parameters by fitting.

11.1.3. Fitting of the proximity parameters

The extracted data points ($D_{applied}$, R) are shown in figure 109. The graph in figure 109 can be fitted by the following function:

Equation 11-1) $$D_{app} = D_c \left[\frac{1}{(1+\eta+\nu_1+\nu_2)} \left(e^{-\left(\frac{R}{\alpha}\right)^2} + \eta\, e^{-\left(\frac{R}{\beta}\right)^2} + \nu_1\, e^{-\left(\frac{R}{\gamma_1}\right)^2} + \nu_2\, e^{-\left(\frac{R}{\gamma_2}\right)} \right) \right]^{-1}$$

$\eta, \nu_{1,}\nu_2, \alpha, \beta, D_c$... fitting parameters, R … inner radius of the doughnut; D_{app}…applied dose to the outer circle.

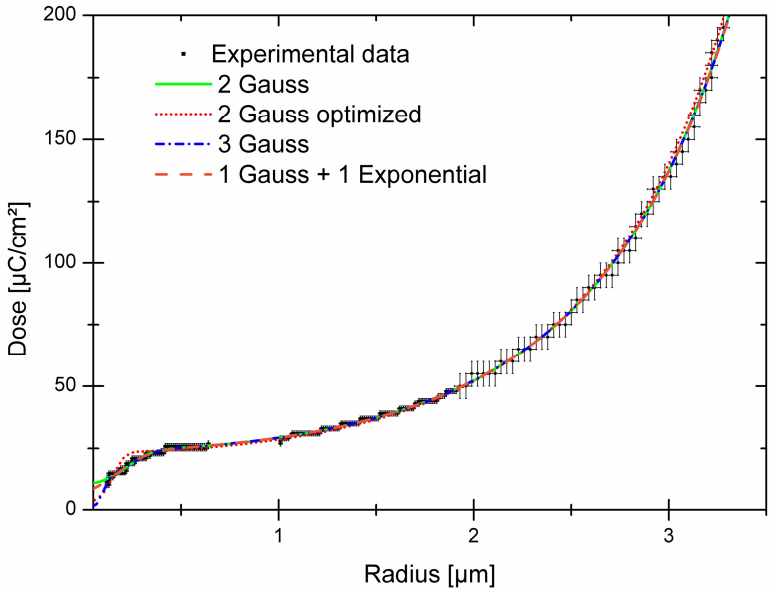

Figure 109: Result of the doughnut test; inner radius R1 as a function of the applied dose. The function was fitted by non linear least squares with equation 11-1.

The first try to fit the proximity parameters was to use the same approach as in reference [**29**] where the critical exposure D_c was also used as a fitting parameter. In order to know which model is the best, the graph in figure 109 was fitted with different proximity terms by setting the corresponding pre-factors η, ν_1, ν_2 to 0. Three proximity functions were investigated: 1 Gauss term + 1 Exponential term, 2 Gauss terms and 3 Gauss terms. Additionally, another modified 2 Gauss proximity function was fitted. This function was fitted with α fixed to 0.1. The results of the fits are shown in table 7.

Table 7: Results of doughnut test. Bold values are fixed and were not varied during the fit. All values are in µm.

Parameters	2 Gauss terms [µm]	Modified 2 Gauss terms [µm]	3 Gauss terms [µm]	1 Gauss term + 1 exponential term [µm]
α	0.197±0.004	**0.1**	0.004±0.002	2.28±0.004
β	2.27±0.004	0.24±0.007	2.28±0.004	-
η	0.73±0.03	0.14±0.01	0.052±0.1	-
γ_1	-	-	0.21±0.005	-
γ_2	-	-	-	0.067±0.002
υ_1	-	-	0.058±0.002	-
υ_2	-	-	-	2.27±0.1
D_C	19.2±0.2	2.88±0.2	1.12±2	7.4±0.3

All the proximity functions fit the experimental data very well. Anyhow the α parameters and η have a high variance depending on the starting value of the fits, i.e. the fits are not very robust. The models are almost identical, i.e. the curves lay on each other, at a large inner radius (>1 µm). They differ in a range below 1 µm. The most common 2 Gauss proximity function is not suited to fit this regime. The modified 2 Gauss function leads almost to the same adjusted R square, but fits the data better around 150 nm, whereas the fit in the regime between 150 nm and 400 nm gets worse (see

figure 110). This is maybe due to scattering in the resist, high energy secondary electrons and tails in the beam distribution. [**20**]

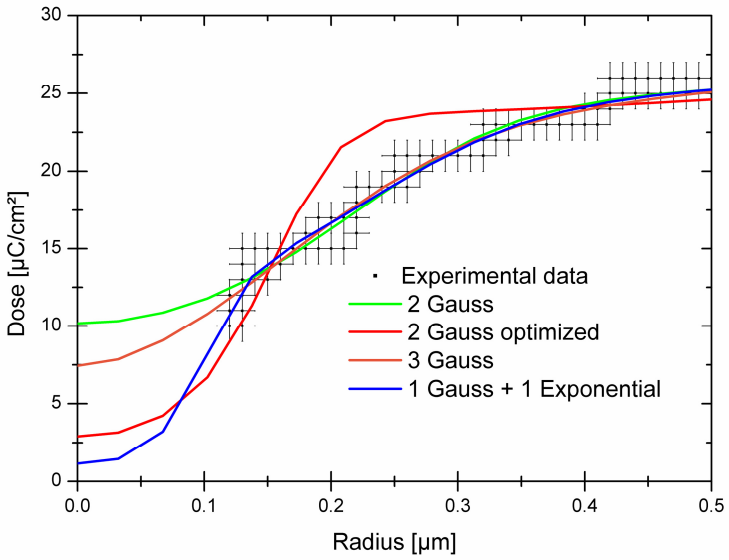

Figure 110: Results of doughnut test. Fitted with the critical deposited dose as a fitting parameter. The fits are not very robust and are not suited to describe the proximity function in a range below 500 nm.

In fact, it is not important to obtain physical meaningful proximity parameters, but it is important to replicate the profile of the experimentally determined proximity function. It does not matter if the fits are not robust as long as the fitted proximity functions have the same profile as the experimentally one. This is not the case for the fits made in figure 110. The problem posed by the somewhat unrealistic values of the critical deposited dose D_c. The parameter D_c itself actually has no relevance, but it influences the relevant normalization factors of the proximity functions and their profiles in the sub 500 nm range (see figure 110).

Therefore, in a second approach the critical deposited dose D_c was fixed to 9 µC/cm² (incipient dose extracted from the contrast curve). The results of the fits are listed in table 8 and shown in figure 111 (sub 500nm regime). Due to one parameter less, all fits turned out to be robust and the results are presented in table 8. It is believed that the different values of the proximity parameters in literature are mainly due to a combination of a lack of data below 100 nm the use of a non-normalized curve fitting technique. [**21**], [**77**]

Table 8: Results of the fits of the doughnut test. The critical deposited dose fixed at 9 µC/cm².

Parameters	2 Gauss terms [µm]	3 Gauss terms [µm]	1 Gauss term + 1 exponential term [µm]
α	0.18±0.002	0.15±0.01	2.28±0.004
β	2.278±0.005	2.278±0.005	-
η	0.6±0.003	0.93±0.3	-
γ_1	-	0.24±0.03	-
γ_2	-	-	0.067±0.002
υ_1	-	0.57±0.46	-
υ_2	-	-	2.27±0.1
D_C	9	9	9
Adj. R Square	0.97769	0.99565	0.99558

As one can see in figure 111, all models fit the data very well. The shape of the proximity function is almost the same for all three models. It's therefore not important which model is used knowing that the results of the simulations will be the same. The exponential term, however, is numerically difficult to treat. The simulation time doesn't differ between the 2 Gauss model and the 3 Gauss model. This is why the 3 Gauss model was chosen to describe the proximity function used for all future energy density simulations and proximity corrections.

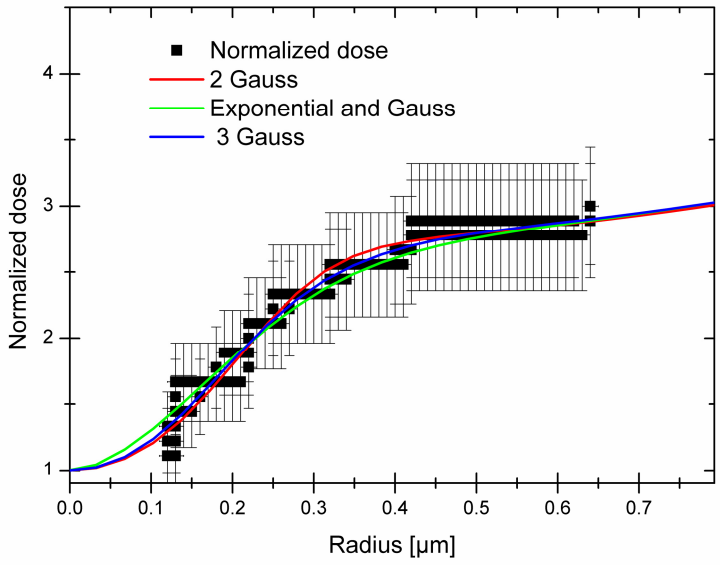

Figure 111: Normalized dose $D_{normalized} = \frac{D_{applied}}{D_c}$ as a function of the inner radius. The clearing deposited dose was not used as a fitting parameter. All models lead to the same result and the fits turned out to be robust.

VIII) Sample cleaning procedure

The cleaning procedure of the samples has to be done very carefully. Failures during cleaning are fatal. Reproducibility is very important!

The samples are cleaned like this:

- Rinse with acetone
- Blow dry with N_2
- Rinse with isopropanol
- Blow dry with N_2
- Clean the sample in a ultrasonic bath for 1 min at a power of 2
- Blow dry with N_2
- Rinse with H_2O
- Blow dry with N_2
- The sample is then further dried by spin coating at 6000 RPM for 60 s
- The sample is placed on a hot plate at 200 °C for 5 min. The sample is flushed with N_2 and then a vacuum is applied.

This process step does, however, not influence the contact angle. OH groups are therefore not believed to liberate from their contaminants.

IX) Stamp and stick bonding

The samples are fabricated with the standard procedure and a curing time of 1 ½ h at 100 °C for completely cured molds and at 50 °C for 1 h for partially cured molds. The adhesive was spin coated onto a SiO_2 substrate. The spin parameters were extracted from literature:

- PDMS : toluene 1 : 6 (0.8 µm after coating, 0.4 µm transferred), 1 : 1 (~10 µm after coating, transferred ~5 µm), 1:2 (~2.5 µm after coating, ~1.5 µm transferred). Spin parameters: 500 RPM 3 s followed by 1500 RPM 60 s. Ramp = 0. [**63**]
- PDMS pre-polymer: after coating: 1 - 1.5 µm and after transfer: 0.74 µm. Spin parameters: 8 min-9 min, 8000 RPM. This spin parameters are not possible with our spin coater. The following parameters were taken: 500 RPM 100 s, 6000 RPM 500 s, and ramp 9. [**64**]
- No literature was found for the curing agent. The following spin parameters were chosen: 4000 RPM 30 s. The thickness is not known and hard to determine because the curing agent is liquid and won't get solid until cross-linking with the PDMS.

Very important: Spin coating PDMS pre-polymer creates a mess. Protecting the whole spin coater including the cap with silver foil is obligatory. Once the film is spin coated, it has to be transferred to the PDMS stamp and subsequently to the substrate. One problem is that air bubbles easily get enclosed underneath the chip, impeding a proper transfer. The chip shouldn't be moved either because this could fill the channels with adhesive. For toluene and the curing agent no problems have been encountered / thought of so far. Undiluted PDMS pre-polymer on the other hand turned out to be time critical since it cures at RT and therefore changes viscosity. If PDMS pre-polymer is used as an adhesive, fast processing (<< 4h) is necessary.